1985

Charge Simulation Technique As Applied To Electrostatic Precipitators

Alaa Abdel-azim Elmoursi

CANADIAN THESES ON MICROFICHE

I.S.B.N.

THESES CANADIENNES SUR MICROFICHE

National Library of Canada
Collections Development Branch

Canadian Theses on
Microfiche Service

Ottawa, Canada
K1A 0N4

Bibliothèque nationale du Canada
Direction du développement des collections

Service des thèses canadiennes
sur microfiche

NOTICE

The quality of this microfiche is heavily dependent upon the quality of the original thesis submitted for microfilming. Every effort has been made to ensure the highest quality of reproduction possible.

If pages are missing, contact the university which granted the degree.

Some pages may have indistinct print especially if the original pages were typed with a poor typewriter ribbon or if the university sent us a poor photocopy.

Previously copyrighted materials (journal articles, published tests, etc.) are not filmed.

Reproduction in full or in part of this film is governed by the Canadian Copyright Act, R.S.C. 1970, c. C-30. Please read the authorization forms which accompany this thesis.

THIS DISSERTATION
HAS BEEN MICROFILMED
EXACTLY AS RECEIVED

AVIS

La qualité de cette microfiche dépend grandement de la qualité de la thèse soumise au microfilmage. Nous avons tout fait pour assurer une qualité supérieure de reproduction.

S'il manque des pages, veuillez communiquer avec l'université qui a conféré le grade.

La qualité d'impression de certaines pages peut laisser à désirer, surtout si les pages originales ont été dactylographiées à l'aide d'un ruban usé ou si l'université nous a fait parvenir une photocopie de mauvaise qualité.

Les documents qui font déjà l'objet d'un droit d'auteur (articles de revue, examens publiés, etc.) ne sont pas microfilmés.

La reproduction, même partielle, de ce microfilm est soumise à la Loi canadienne sur le droit d'auteur, SRC 1970, c. C 30. Veuillez prendre connaissance des formules d'autorisation qui accompagnent cette thèse.

LA THÈSE A ÉTÉ
MICROFILMÉE TELLE QUE
NOUS L'AVONS REÇUE

CHARGE SIMULATION TECHNIQUE AS APPLIED TO ELECTROSTATIC PRECIPITATORS

by

Alaa Abdel-Azim Elmoursi

Faculty of Engineering Science

Submitted in partial fulfillment

of the requirments for the degree of

Doctor of Philosophy

Faculty of Graduate Studies

The University of Western Ontario

London, Ontario

March, 1985

ABSTRACT

To be able to properly predict the performance of electrostatic precipitators, a complete knowledge of the electrical conditions existing is necessary. The equations governing such conditions are analytically solvable for the cylindrical geometry, but no similar exact solutions are available for the more common duct-type geometry.

In this work, one of the objectives was to present a method based, on the charge simulation technique, that accurately evaluates the electrical parameters in duct-type precipitators. The method is intended to be applicable to variable physical dimensions of the precipitator as well as to account for a wide range of operating conditions, particularly dust loading conditions.

The charge simulation technique was choosen following a literature survey and analysis, conducted by the author, for the different methods available for evaluating the electrical parameters of duct-type precipitators. The survey involved the approximate analytical methods of P. Cooperman, G. Cooperman and conformal transformations as presented by Sekar. Also the numerical methods of finite difference and finite element as presented by McDonald and Hoburg respectively.

In choosing the charge simulation method, the author developed a procedure for adapting this technique to solve problems that in general involve space charge of unknown distributions.

Computer models based on the charge simulation technique are developed to model the electrostatic, the corona in clean air and the corona quenching cases in cylindrical precipitators. These models were developed with the intent of checking the validity and the accuracy of applying the charge simulation technique to such conditions. Later these models were extended to the more complex duct-type geometry.

For the duct geometry, the electrostatic model based on the charge simulation method, gave good agreement to the infinite series developed by Cooperman and Böhm for this case.

Also the corona in clean air model, as developed by the author, shows good agreement to the published experimental work of Penney, Felici and Tassicker.

Another objective of this work was to investigate the enhanced performance of wide-duct spacing precipitators (0.4 to 0.6 m) compared to standard duct spacing (0.15 to 0.25 m).

Since no experimental data was found in the literature concerning the electrical parameters of wide duct spacing precipitators, it was decieded to design and construct a laboratory scale electrostatic precipitator of variable duct spacing. Experiments were carried out to measure the current density and electric field distributions at the collecting plates for three duct spacings: 0.2, 0.4 and 0.6 m. The experimental results further confirmed the validity of the corona model.

Finally, a corona quenching model was developed for the duct geometry. This model was also used in the study of wide duct spacing precipitators.

The results of this study show that the technique is suitable for the purpose of accurately predicting the electrical characteristics of electrostatic precipitators under variable operating conditions. These models eliminate the cost and time needed in constructing and experimenting with prototype models.

ACKNOWLEDGEMENTS

The author wishes to express his deep gratitude to Professor G.S. Peter Castle for his supervision and valuable guidance which he generously offered throughout the course of this work.

Thanks are also extended to Professor I.I. Inculet and Assistant Professor W.D. Greason for their encouragement and helpful suggestions.

Gratitude is also expressed to Mr. Dave Woytowich of the Engineering Mechanical Shop for his good fabrication of the experimenatl apparatus.

The financial support from the National Research Council of Canada is also gratefully acknowledged.

Last, but not least, the author wishes to convey his sincere gratitude to his wife Maysa for her patience, understanding and self-sacrifice.

TABLE OF CONTENTS

LIST OF TABLES

LIST OF FIGURES

NOMENCLATURE

a	mean particle radius (m)
A	total collecting surface area (m^2)
A^n_{li}	area of the ith element at the first contour after n interations (m^2)
A^n_{ki}	area of the ith element at the kth contour after n iterations (m^2)
b	mobility ($m^2/V.s$)
b_i	ion mobility ($m^2/V.s$)
b_p	particle mobility ($m^2/V.s$)
C	constant (V^2)
e	ion charge (C)
E	electric field (V/m)
E^n_{li}	electric field at the ith element of the first contour after n iterations (V/m)
E_{av}	average electric field in gap = V_c/h (V/m)
E^*_{av}	assumed average charging field (V/m)
E_c	charging electric field (V/m)
E_{ki}	electric field at the ith element of the kth contour (V/m)
E_m	electric field at the mth element (V/m)
E_o	corona onset field (V/m)
E_p	plate (precipitating) electric field (V/m)
E_u	electric field component in the u-direction (V/m)
E_v	electric field component in the v-direction (V/m)
E_x	electric field component in the x-direction (V/m)
E_y	electric field component in the y-direction (V/m)

h	wire to plate spacing (m)
I_c	total corona current (A)
I_i	the current flowing between two successive trajectories (A/m)
I_{tot}	experimental current from all corona wires (A)
J	current density (A/m^2)
J_i	average current density at the ith element (A/m^2)
J_ℓ	linear corona current density (A/m)
K	Boltzmann's constant (J/°K)
K_p	relative dielectric constant of particles (dimensionless)
L	length of corona wire (m)
N_o	undisturbed ion concentration (m^{-3})
P	dimensionless parameter
P_c	corona power (watts)
q	line charge per unit length (C/m)
q_{li}^n	ith line charge per unit length at the first contour after n iterations (C/m)
q_i	ionic line charge per unit length (C/m)
q_{im}	mth ionic line charge per unit length (C/m)
q_{ki}^n	ith ionic line charge per unit length at the kth contour after n iterations (C/m)
q_{max}	limiting particle charge (C)
q_p	particle line charge per unit length (C/m)
r	radial distance using cylindrical co-ordinates (m)
r_c	corona wire radius (m)
r_o	radius of the outer cylinder (m)

Δr_m	radial distance between two successive equipotential contours (m)
s	half wire to wire spacing (m)
S	specific surface area of particles (m^2/m^3)
ΔS^n_{li}	curved arc length of the ith element at the first contour after n iterations (m)
ΔS_{lm}	outer arc length of elemental area (m)
ΔS_{ki}	curved arc length of the ith element at the kth contour (m)
ΔS_m	average arc length of elemental area (m)
ΔS_{ni}	base length of the ith element at the last contour (n)
t	time (sec)
T	absolute temperature (°K)
u,v	two dimensional co-ordinate system (m)
v'	rms ion velocity (m/s)
v_g	gas flow rate (m^3/s)
V	potential (V)
V_c	corona wire potential (V)
V_o	corona onset potential (V)
ΔV_c	potential due to the ionic space charge for the corona in clean air model (V)
ΔV_i	potential due to the ionic space charge for the corona quenching model (V)
ΔV_p	potential due to the particle space charge for the corona quenching model (V)
x	distance in the x-direction (m)
y	distance in the y-direction (m)
δ	gas density relative to 25 °C and 1 atm (dimensionless)
ε_o	permittivity of free space, 8.86×10^{-12} (F/m)

η	precipitator fractional efficiency
λ	mean free path of air ions at STP (m)
μ	viscosity of air (dp)
ξ	scaling factor (dimensionless)
ρ	charge density (C/m^3)
ρ_l	charge density at wire surface (C/m^3)
ρ_l^n	charge density at wire surface after n iterations (C/m^3)
ρ_i	ionic charge density (C/m^3)
ρ_{im}	ionic charge density of the mth element (C/m^3)
ρ_{ki}^n	charge density of the ith element at the kth contour after n iterations (C/m^3)
ρ_p	particle space charge density (C/m^3)
ρ_i'	modified ionic space charge density (C/m^3)
ρ_p'	modified uniform particle space charge density (C/m^3)
τ	charging time constant (sec)
ϕ	angle measured from the x-axis (rad)
ω	particle migration velocity (m/s)

CHAPTER ONE

INTRODUCTION

1.1 Air Pollution and Industrial Gas Cleaning

Advances in science and technology in the past twenty years have lead to a rapid growth and expansion of large industries most of which, if not all, contribute to air pollution. One form of air pollution is particulate emissions. Although many devices are suitable for collecting or separating particulate emissions from exhaust gases, electrostatic precipitators are most favoured for this task particularly when small sized particles in the micron and submicron range are involved.

Electrostatic precipitators differ from other types of particulate control equipment in that they use electrical forces to separate particulates from the exhaust gases rather than mechanical forces such as those encountered in settling chambers, baffle chambers, scrubbers and cyclones.

Electrostatic precipitators are mainly used in the fly-ash collection in electric-power generating stations, steel and cement production, the processing of paper and non ferrous metals as well as some other chemical industries.

The major advantages of electrostatic precipitators are high collection efficiencies (95% to 99.9%), small pressure drops and they handle very large flow rates and require little maintenance.

Some of the disadvantages of electrostatic precipitators are:

i) High initial cost.

ii) Some materials are extremely difficult to be collected because of their higher resistivity, usually higher than 10^9 Ω m. This is the result of what is known as the back corona phenomena [1,2]. In normal electrostatic precipitator operation, ions of only one polarity (usually negative) are the current carriers that charge the particles to be collected. In the presence of back corona, ions of the opposite polarity are generated. This reduces the total particle charge and thus the particle collection is seriously degraded.

iii) If the dust concentration in the gas is too high, the corona current may be severely reduced, this is referred to as corona quenching [3]. Under this condition the precipitator efficiency may be reduced.

1.2 Electrostatic Precipitators

The basic principle of electrostatic precipitation is the separation of suspended particles from gases using electrostatic forces.

The separation of the suspended particles from the gaseous media can be sub-divided into three fundamental processes: particle charging, migration and collection. Particle charging is accomplished by generating a corona [4] in the vicinity of a small-diameter wire or any other configuration with a sharp radius which serves as one of the electrodes. The glow region (corona sheath) surrounding the corona electrode is filled with ions of both polarity, but apart from this small region the entire space is filled with unipolar ions. The unipolar ions produced travel along the electric field lines, extending between the corona electrode and the collecting surface, and are intercepted by the dust particles, resulting in a net charge flow to the particle. Charging continues until the net charge on the particle reaches the saturation limit [5]. As the gas traverses the space between the two electrodes, the charged particles under the influence of electrical forces migrate towards the collecting surface. The particles adhere to the collecting walls mainly due to the Coloumbic forces, but other forces such as Van der

Waals and image forces may also exist. The collected particles are removed periodically by rapping or flushing of the collecting surfaces and allowing them to fall into a hopper or sump for subsequent removal.

1.2.1 Basic Types of Electrostatic Precipitators

There are two basic precipitator geometries, both are shown in figure 1.1.

Figure 1.1.a shows the cylindrical geometry or tube-type precipitator, the central fine wire is energized by a D.C. high voltage power source, while the outer cylinder is grounded. Cylindrical tubes may be packed together to form a multi-unit precipitator. Those are commonly used for precipitating sulphuric acid mists and blast furnace fumes [6].

The second basic geometry is the duct geometry, in which a set of corona wires are positioned half way between a set of parallel earthed plates as shown by figure 1.1.b.

Both geometries of figure 1.1 are referred to as single stage precipitators because the charging and the collection processes occur simultaneously in the same stage.

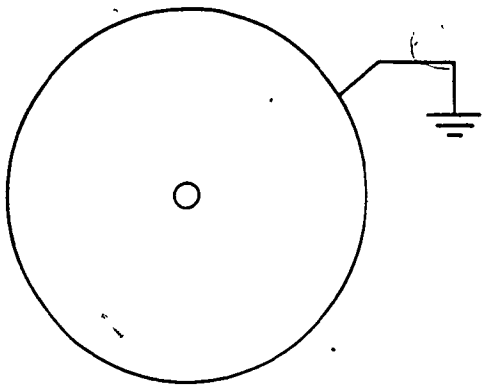

(a) Cylindrical type precipitators

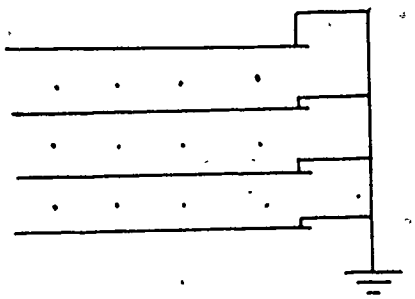

(b) Duct type precipitators

Figure 1.1. Basic electrostatic precipitator geometries

Two stage electrostatic precipitators, whether of the cylindrical or duct-type, are constructed such that the charging process takes place at the first stage in the presence of corona, while the collection process takes place at the second stage under the effect of an electrostatic field.

1.3 Theory of Electrostatic Precipitators

The three processes involved in electrostatic precipitation are presented here in more detail.

1.3.1 Corona Generation

Corona represents a stable condition of conduction in gases. It can only be achieved between asymmetrical electrodes when a relatively large potential difference exists between them. Extensive studies on the corona phenomena have been performed by Cobine [7] and Loeb [8]. The phenomena are also well documented by Nasser [9].

To demonstrate the corona mechanism in electrostatic precipitators consider the cylindrical geometries shown in figure 1.2.

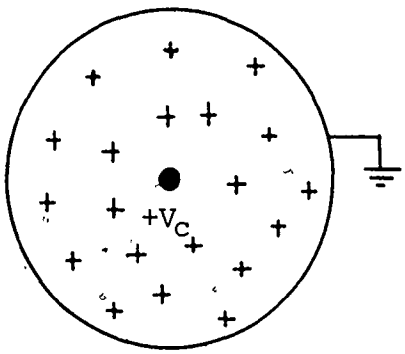

(a) Positive corona

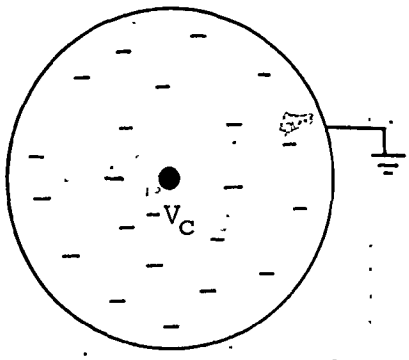

(b) Negative corona

Figure 1.2. Positive and negative corona in a cylindrical geometry

For positive corona, a positive high voltage is applied to the inner corona wire. As a result of the high electric field adjacent to the wire, a Townsend avalanche is initiated and free electrons are produced. The free electrons are pulled quickly towards the inner wire where they are neutralized whereas the positive ions are repelled towards the outer grounded cylinder. Virtually all the current in the space external to the corona envelope is carried by positive ions [10]. Visually the corona appears as a bluish uniform glow surrounding the corona wire.

For negative corona, the wire is energized with negative high voltage. Again a Townsend avalanche is initiated, this time the free electrons are repelled away from the wire. As the electrons travel toward the outer grounded cylinder some of them attach to neutral electronegative gas molecules forming negative ions [11]. These negative ions, due to their relative slowness compared to the free electrons, constitute the unipolar space charge in the inter-electrode gap. In negative corona, the corona electrodes play an active role in producing free electrons and the discharge process is dependent on the electronegativity of the surrounding gas. Visually, the negative corona appears as a series of localized tufts of discharge on the wire surface.

Most industrial applications use single stage precipitators operated under negative corona since higher operating voltages can be achieved prior to breakdown as compared to positive corona. Two stage electrostatic precipitators operated under positive corona are preferred for air cleaning purposes since less ozone is generated [12].

The critical onset field for corona was determined semi-empirically by Peek [13] and is presented by equation (1.1).

$$E_o = \delta\left(A + \frac{B}{\sqrt{\delta r_c}}\right) \qquad (1.1)$$

where A and B are constants depending on the type of gas. For air, the values $A=32.2\times10^5$ V/m and $B=8.46\times10^4$ $V/m^{\frac{1}{2}}$ are recommended [6].

1.3.2 Charging of Particles

In an electric discharge, two distinct particle charging mechanisms are present. The first is field charging, in which the ions under the influence of electric field bombard the particles and impart their charges to them. This process continues until the particles have acquired their saturation charges. The second mechanism is charging by ion diffusion. This charging process is

dependent on the random thermal motion of ions and particles, and is independent of the applied electric field.

It has been shown by Pauthenier [5], that the maximum charge acquired by a spherical particle due to ion-bombardment is given as

$$q_{max} = 4\pi\varepsilon_o P a^2 E_c \tag{1.2}$$

where $$P = 2\left(\frac{K_p - 1}{K_p + 1}\right) + 1 \tag{1.3}$$

The charge at any time, relative to the saturation charge, is given as

$$q(t) = q_{max}\frac{t}{t+\tau} \tag{1.4}$$

where $$\tau = \frac{4\varepsilon_o}{\rho_i b} \tag{1.5}$$

As for diffusion charging, the charge acquired by a particle is given as [14].

$$q(t) = \frac{4\pi\varepsilon_o aKT}{e}\left(1 + \frac{aN_o e^2 v' t}{4\varepsilon_o KT}\right) \tag{1.6}$$

The ion-bombardment process is predominant for particles of size 1 μm or larger, while diffusion charging predominates for particles of size 0.1 μm and less [15]. Thus both charging mechanisms are equally important for particle sizes in between these two ranges. In this case, the saturation charge acquired by the particle may still be calculated using equation (1.2) on condition that equation

(1.3) be replaced by equation (1.7). This last equation modifies the parameter P, as given by equation (1.3), to account for ion diffusion charging [3].

$$P = (1 + \frac{\lambda}{a})^2 + \frac{2}{1 + \lambda/a} \times \frac{K_p - 1}{K_p + 1} \qquad (1.7)$$

1.3.3 Collection of Particles

After the particles have been charged, they may migrate along the lines of electric field and be eventually collected at the grounded surfaces. This simplistic picture of particle collection is only true for laminar flow. For the more realistic form of operation where turbulence is encountered, there are at least three forms of particulate mass transfer from the main body of gas to the collecting electrode:

i) Electrostatic convection under the action of Coulomb forces.

ii) Turbulent diffusion of aerodynamic and electrodynamic origin, such as electric wind [16].

iii) Inertial drift.

The migration velocity of the particles adjacent to the collecting walls is given by equation (1.8). This equation is derived by equating the electrical and the aerodynamic drag forces acting on the particle.

$$\omega = \frac{2P\varepsilon_o E_c E_p a}{3\mu} \qquad (1.8)$$

The migration velocity represents a measure of the rate at which particles are collected, this is shown by Deutsch's efficiency equation [17] given below.

$$\eta = 1 - e^{-(A\omega/v_g)} \qquad (1.9)$$

It is well recognized that the above equation does not completely model the collection process. Thus it has often been criticized and many modifications and alterations have been introduced [17, 18 and 19].

The electric field in electrostatic precipitators, as seen from the previous discussions, serves a three fold purpose: initiating the corona, charging the particles and finally precipitating them. Thus it is clear that the electric field is a parameter of fundamental importance in electrostatic precipitators.

To be able to predict the performance of electrostatic precipitators, a complete knowledge of the electric field distribution becomes a necessity.

1.4 General Objectives

The electric field in electrostatic precipitators, whether under clean air conditions or in the presence of dust particles, is governed by Poisson's equation (1.10).

$$\nabla^2 V = - \frac{\rho}{\varepsilon_o} \qquad (1.10)$$

The above equation can be solved analytically for the cylindrical geometry. On the other hand it is formidable to solve for the duct geometry. Thus the main objective of this study was to predict the electrical conditions that exist in electrostatic precipitators under clean air conditions as well as in the presence of dust loadings.

Following a review of the major approximate analytical solutions and numerical methods suggested by other researchers for evaluating the electrical variables in duct-type precipitators, it was decided to establish a set of computer models, based on the charge simulation technique [20,21]. The purpose of these models is to simulate the electrical variables of cylindrical and duct-type precipitators. The charge simulation technique was attractive because it is not an iterative procedure and thus it is expected to reduce computational time. In addition, it has only been used recently (1980) to model space charge of unknown distribution.

All programs developed, based on the charge simulation technique, are available on file at the Seam Laboratory, Faculty of Engineering Science, The University of Western Ontario (refer to Appendix 1).

The study involved the evaluation of the electric field, the electric potential, the current density and the ionic (and particle) space charge density distributions in the inter-electrode gap of the two geometries.

The charge simulation models were used to investigate the importance of the value of mobility of negative and positive ions.

Another prime objective of this study was to investigate the electrical variations that occur in wide-duct spacing precipitators (400 to 600 mm) as compared to conventional duct spacings (150 to 250 mm). This study was motivated by the recent increasing interest in wide-duct precipitators and the lack of sufficient theory to explain why such precipitators perform well.

This part of the study was supplemented by conducting experiments on a variable duct spacing electrostatic precipitator laboratory model. Both the electric field and the current density distributions were measured along the collecting plate under clean air conditions. The

experimental results were used to compare the effect of variable duct spacing and also to verify the computer model developed for duct-type precipitators.

Particular consideration was given to the effect of the particle space charge on the electric field enhancement at the precipitator walls in wide-duct precipitators and standard precipitators exposed to corona quenching of different degrees.

CHAPTER TWO

CRITICAL REVIEW OF LITERATURE

2.1 Introduction

The electrical conditions in electrostatic precipitators are primarily governed by two equations. Those are, Poisson's equation (2.1) and the current continuity equation (2.2).

$$\nabla^2 V = - \frac{\rho}{\varepsilon_0} \qquad (2.1)$$

$$\text{div.}J = \text{div.}(\rho b E) = 0 \qquad (2.2)$$

The above set of equations are solvable analytically for the cylindrical geometry, both in clean air and in the presence of dust loading. These are presented in chapters three and four respectively. Unfortunately, no similar exact solutions are available for the more common duct-type geometry.

This chapter is dedicated to presenting the different approximate analytical solutions as well as the numerical procedures proposed by several investigators for solving equations (2.1) and (2.2) for the duct-plate geometry.

All the approximate analytical solutions and numerical procedures presented in this chapter, with the exception of the finite element procedure, were formulated into computer programs by the author. The results of the preceeding methods, as evaluated by the formulated computer programs, are compared to experimental data to check their validity and accuracy.

2.2 Analytical and Numerical Methods as Applied to Duct-Type Precipitators

2.2.1 Analytical V-I Characteristics

In an attempt to approximately solve both Poisson's and the current continuity equations, P. Cooperman [22] proposed equation (2.3) for the V-I characteristics of a duct-type precipitator under dust-free conditions.

$$\bar{J}_\ell \cong \frac{4\pi\epsilon_o b}{h^2 \ln(d/r_c)} V_c(V_c - V_o) \qquad (2.3)$$

where $$V_o = r_c E_o \ln(d/r_c) \qquad (2.4)$$

and $$d = \frac{4h}{\pi} \sum_{m=1}^{\infty} \frac{\cosh(m\pi s/h) + 1}{\cosh(m\pi s/h) - 1} \qquad (2.5)$$

This approximate equation, according to P. Cooperman, is only accurate for low current densities.

Later, P. Cooperman [23] utilized equation (2.3), for evaluating the V-I characteristics in the presence of dust particles, after replacing the term V_o by another term V_o' which is given by equation (2.6).

$$V_o' = V_o + \frac{\rho_p h^2}{2\varepsilon_o} \tag{2.6}$$

The second term in equation (2.6) represents the apparent increase in the corona onset potential due to the presence of a uniform particle space charge density ρ_p.

Fifteen years later, G. Cooperman [24] proposed another approximate solution for the V-I characteristics under clean air conditions, this is given below as.

$$J = \frac{\varepsilon_o b}{16h^3} \left[\alpha + \sqrt{\alpha^2 + 192(V_c - V_o)(hE_1)^3} \right] \tag{2.7}$$

where $$\alpha = 9(V_c - V_o + hE_1)^2 - 12(hE_1)^2 \tag{2.8}$$

and $$E_1 = \frac{\pi V_o}{2s \ln(d/r_c)} \tag{2.9}$$

Equation (2.7) was derived on the basis of imagining an arbitrary plane placed between the array of corona wires and the collecting plate. The purpose of this plane is to visualize the electric field as being uniform on the plate side of the plane, thus reducing the problem to one dimension in a direction (x) extending from the plane to the collecting plate.

G. Cooperman extended his method, to account for a uniform particle space charge density ρ_p, while still considering the problem to be one dimensional. In this case Poisson's equation was reduced to the following form [24].

$$\frac{dE}{dx} = \frac{\rho_i}{\varepsilon_o} + \frac{\rho_p}{\varepsilon_o} \tag{2.10}$$

where $$\rho_i = J/bE \tag{2.11}$$

When solving the above set of equations, the electric field E_x is given implicitly as a function of the current density J and the distance x.

Equations (2.3) and (2.7) which give the V-I characteristics under clean air conditions were investigated. They were both applied to two of Sekar's geometries [25] and compared to his experimental data. The results are shown in figures 2.1 and 2.2.

The first geometry, which is given in figure 2.1, represents a precipitator of conventional duct spacing. It is clear that equation (2.7) gives a closer fit to the experimental data as compared to equation (2.3). For the second geometry, the duct spacing is increased and both equations (2.3) and (2.7) give a reasonably good fit to the experimental data.

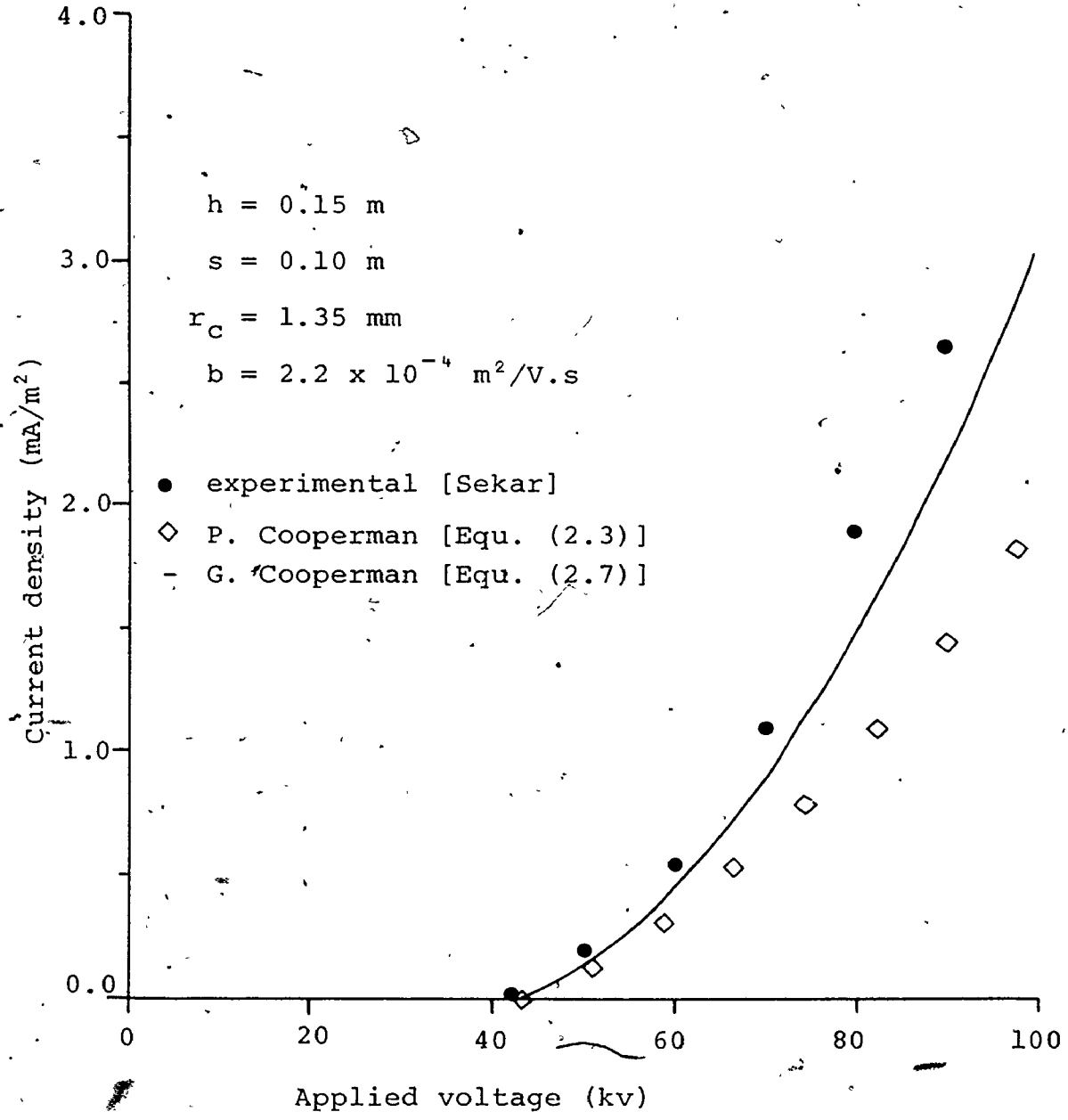

Figure 2.1. V-I characteristics in clean air for conventional spacing of a duct-type precipitator

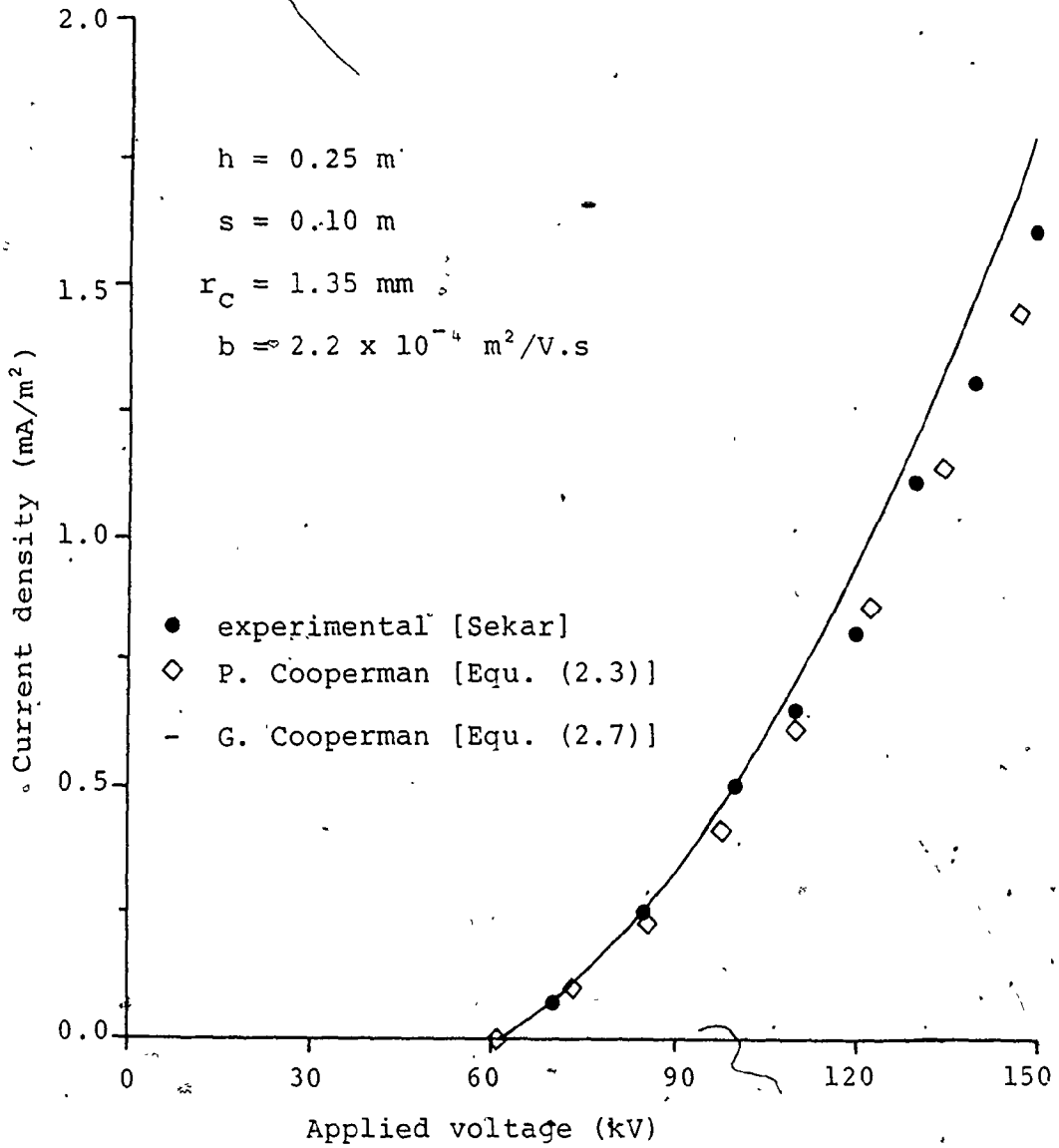

Figure 2.2. V-I characteristics in clean air for a wide-spacing duct-type precipitator

The value of the negative ionic air mobility used for the two cases was 2.2×10^{-4} $m^2/V.s.$ This value was choosen since the experimental data was for negative corona. It was found that by reducing the mobility to 1.7×10^{-4} (the value suggested by Sekar), the difference between the results of equations (2.3) and (2.7) is increased. This difference was observed for the two duct spacings investigated and is clearly illustrated by comparing figures 2.3 and 2.1.

In the previous cases presented, the experimental value of V_o was used rather than using equation (2.4). This equation always overestimated the corona onset voltage and resulted in the shift of the V-I characteristics away from the experimental data.

Equation (2.3) in conjuction with equation (2.6) was also used to evaluate the V-I characteristics under dust loading for Awad's [3] precipitator geometry. Equation (2.12) was used to evaluate the particle space charge density ρ_p [26].

$$\rho_p = \varepsilon_o P E_c S \qquad (2.12)$$

According to equation (2.12), the particle charge density ρ_p is a function of the charging field E_c which is variable with position. Thus to satisfy P. Cooperman's assumption of uniform particle space charge, an assumed value of average charging field E^*_{av} was used. In this case

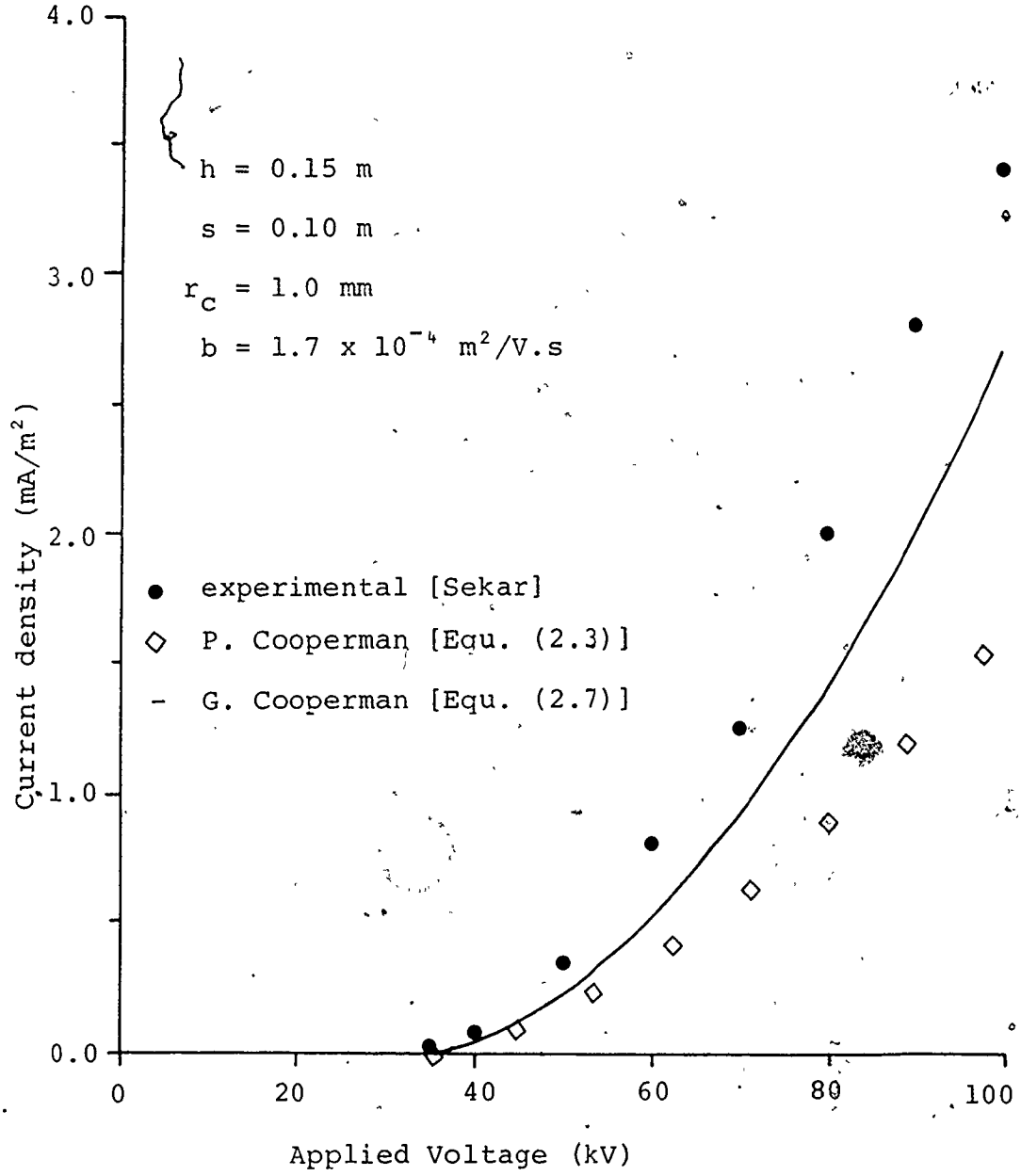

Figure 2.3. Effect of reducing ionic mobility value on the V-I characteristics when using Equations (2.3)and (2.7)

E^*_{av} was assumed equal to 5 kV/cm.

The value of the specific surface area of the D.O.P particles used was 14.7 m^2/m^3 . The value of P was evaluated using equation (1.7) which is suitable for the D.O.P particle sizes that were used. The results of using equation (2.3) as well as the experimental data are included in figure 2.4. It is clear from this figure that equation (2.3) is rather inadequate for evaluating the V-I characteristics under conditions of dust loading.

Equation (2.10) was solved numerically to evaluate the V-I characteristics under dust loading for Awad's [3] precipitator geometry. The value of the uniform particle charge density ρ_p was similar to that used for equation (2.3). It is clear from figure 2.4 that equation (2.10) gives good agreement to the experimental data for low values of linear current density, but deviates away for higher values. Nevertheless, this equation appears to be more accurate than equation (2.3), in terms of predicting the V-I characteristics of duct-type precipitators in the presence of a uniform particle space charge density ρ_p.

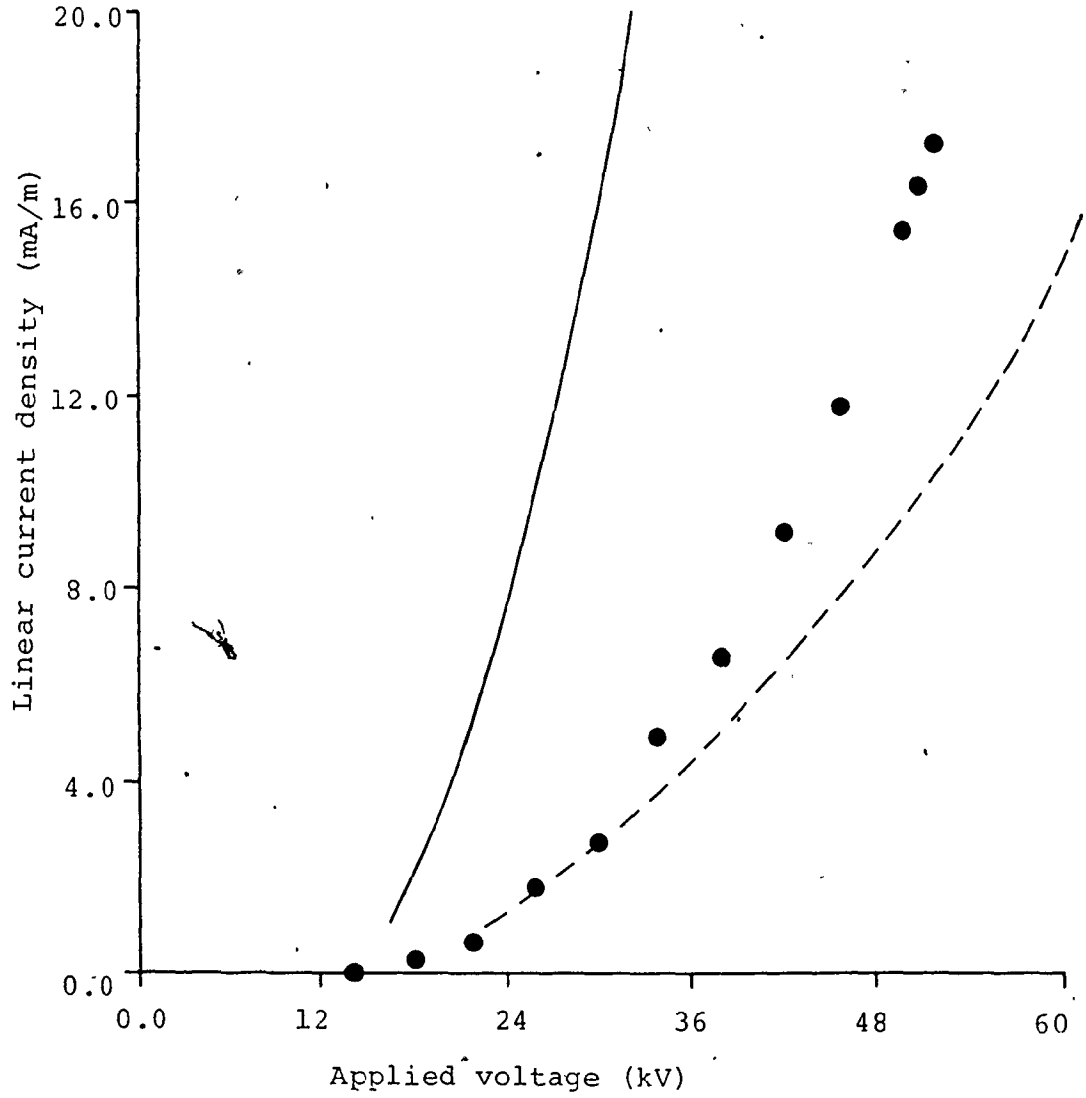

h = 0.038 m

S = 14.7 m^2/m^3

r_c = 0.125 mm

b = 2.2 x 10^{-4} $m^2/V.s$

● experimental Awad

— P. Cooperman [Equ. (2.3) and (2.6)]

-- G. Cooperman [Equ. (2.10)].

Figure 2.4. V-I characteristics under dust loading for a duct-type precipitator

2.2.2 Conformal Transformations

Vershchagin [27] and later Sekar [25] proposed a method for solving Poisson's and the current continuity equations for the wire plate geometry in clean air. Their method is based on the conformal transformation of the wire plate geometry to the cylindrical geometry as shown by figure 2.5.

The equations used for evaluating the electric field components (E_u and E_v) and the charge density $\rho(u,v)$ are given respectively below.

$$E_u = V_c \frac{\sigma \sinh 2\sigma u}{2r^2} \frac{}{\sqrt{C_2 + C_1 \ln(r^2 + \sqrt{1 + r^4})}} \qquad (2.13)$$

$$E_v = V_c \frac{\sigma \sin 2\sigma v}{2r^2} \frac{}{\sqrt{C_2 + C_1 \ln(r^2 + \sqrt{1 + r^4})}} \qquad (2.14)$$

$$\rho(u,v) = \frac{C_1 \varepsilon_o V_c \sigma^2}{\sqrt{1 + r^4}} \frac{\sqrt{1 + 2r^2 \cos 2\theta + r^4}}{\sqrt{C_2 + C_1 \ln (r^2 + \sqrt{1 + r^4})}} \qquad (2.15)$$

where $C_1 = \dfrac{J_\ell}{2\pi\sigma^2 \varepsilon_o b V_c^2}$

$$C_2 = \left(\frac{E_o r_c}{V_c}\right)^2$$

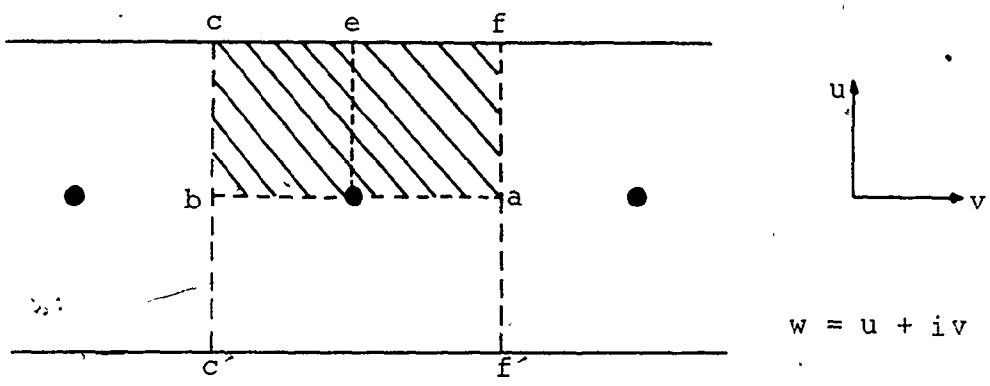

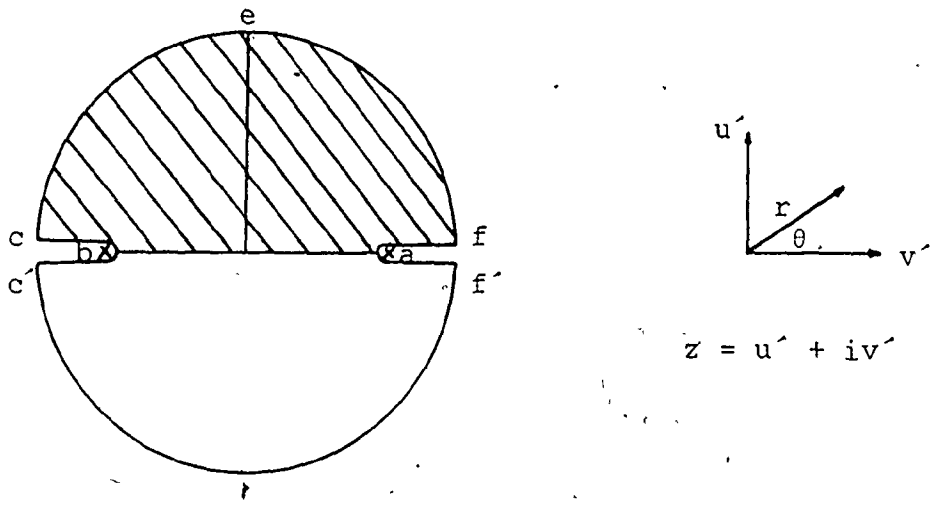

The transformation used is: $z = \sinh \sigma w$

Figure 2.5: Conformal transformation from wire-plate geometry to cylindrical geometry

$$r^2 = \sinh^2\sigma u \cos^2\sigma v + \cosh^2\sigma u \sin^2\sigma v$$

$$\tan\theta = \coth\sigma u \tan\sigma v$$

$$\sigma = \pi/2s$$

A close look at equations (2.13) to (2.15) reveals that they are independent of the applied potential V_c. Thus for a given precipitator geometry and operating linear corona current J_ℓ, the applied potential V_c may be evaluated by integrating equation (2.14) from the wire surface to the plate.

The above method was used for evaluating the V-I characteristics for the geometries as documented by G. Cooperman (the actual experimental work was performed by Robinson [28]). The results as well as the experimental data are given in figure 2.6 and 2.7. These results indicate that the above method tends to overestimate the wire potential V_c, for a given linear corona current J_ℓ. The main reason for this error is due to the difference between the experimental and analytical onset potentials. This is expected, since the analytical equations do not account for any reduction in the onset potential (or onset field).

The conformal transformation method was also applied to Tassicker's geometry [29] and compared to his experimental data for the current density distribution at the collecting plates. The results are shown in

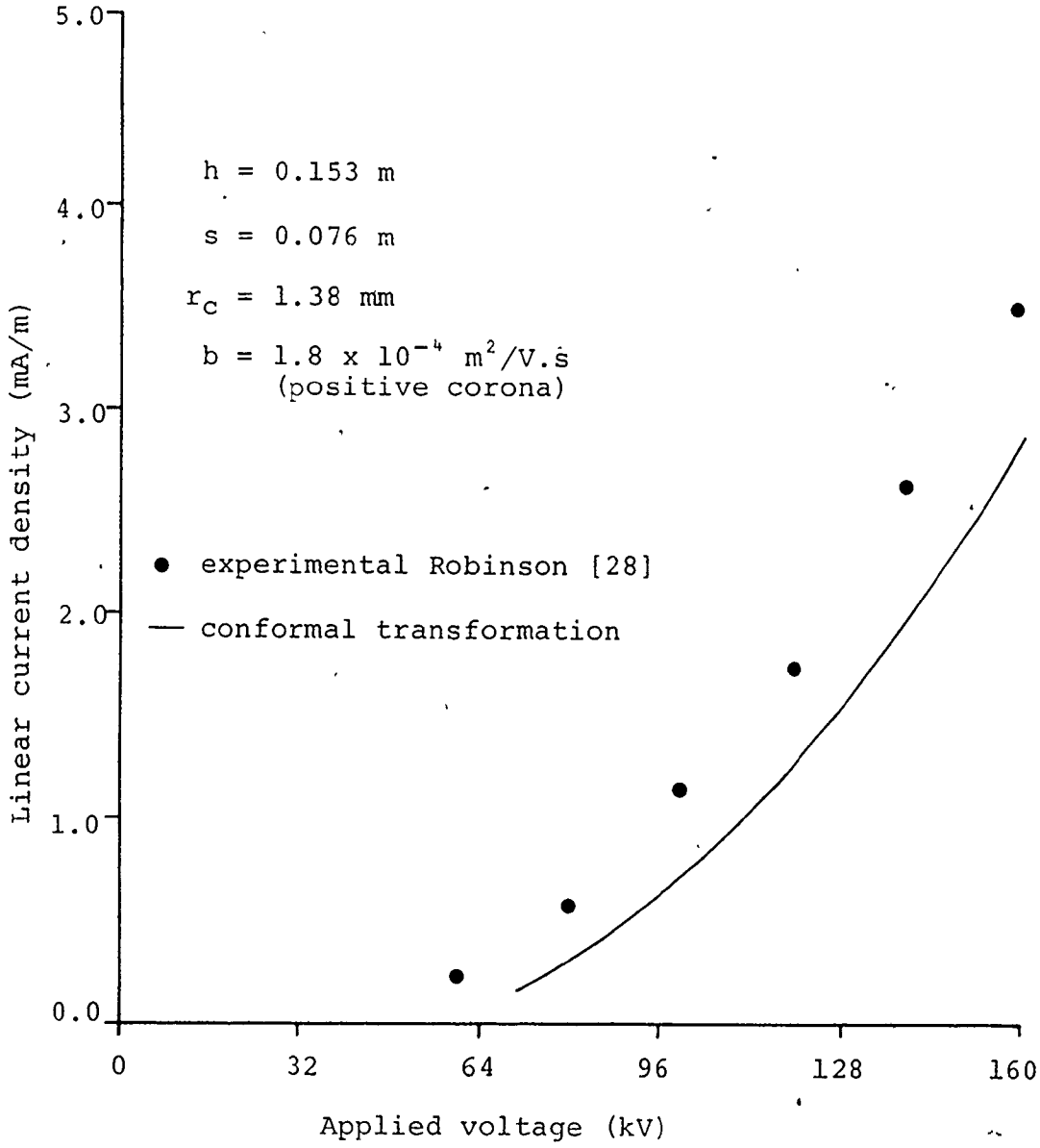

Figure 2.6. V-I characteristics in clean air for standard duct spacing using conformal transformation

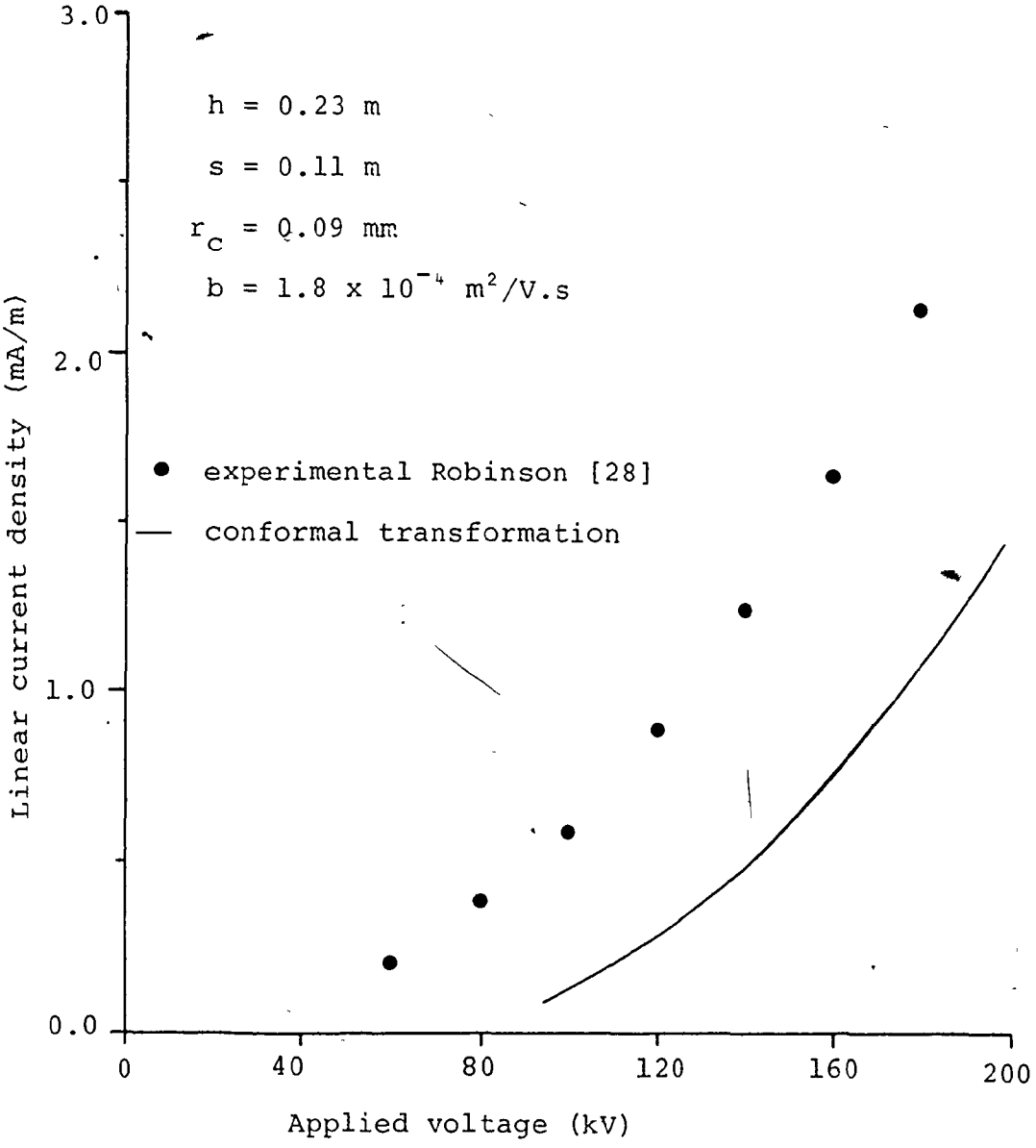

Figure 2.7. V-I characteristics in clean air for wide-duct spacing using conformal transformation

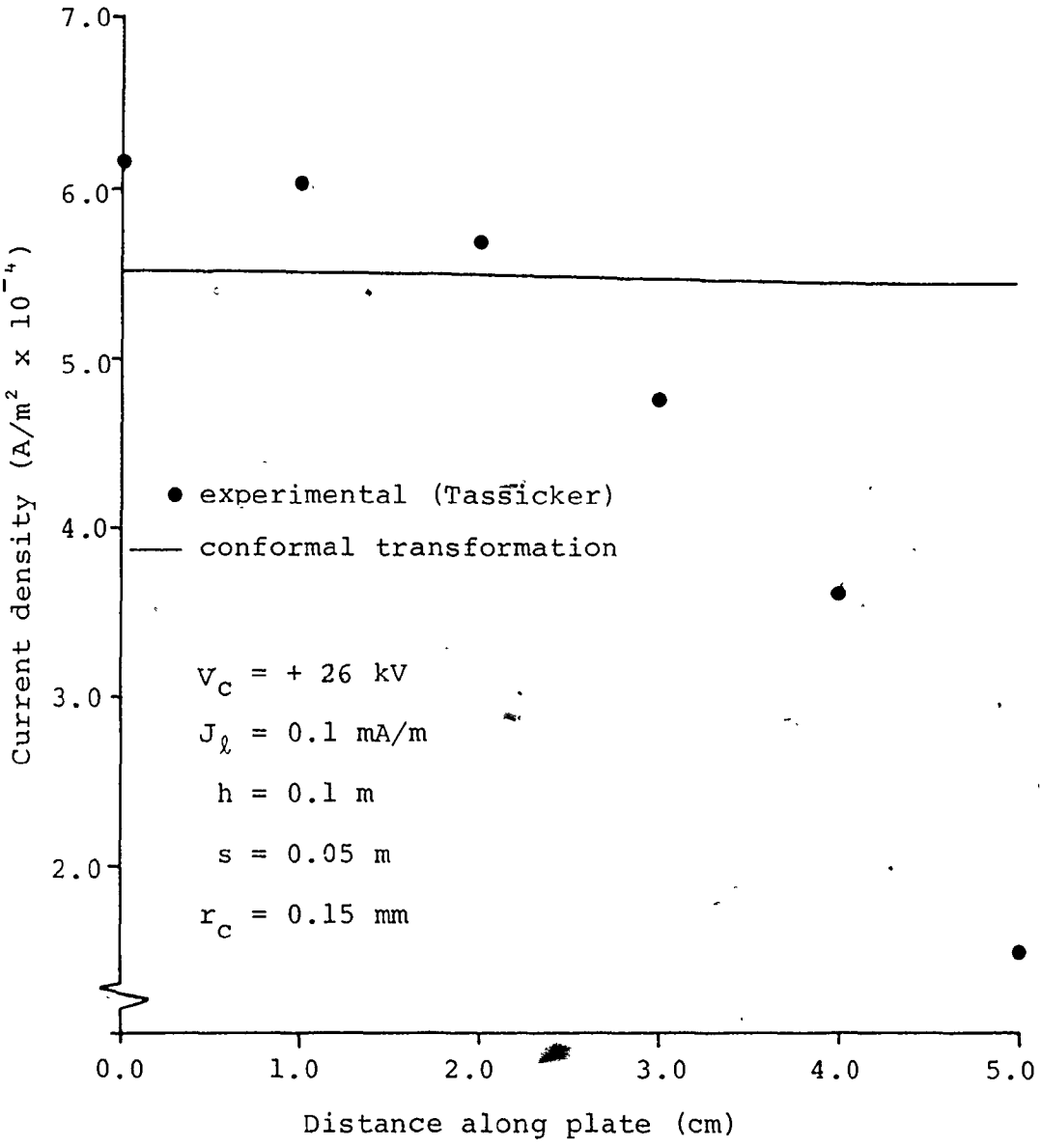

Figure 2.8. Current density distribution at the collecting plate using conformal transformation

figure 2.8. Similar disagreement was observed when comparing the conformal transformation method to the experimental data of Felici [30] and Penney and Matick [31].

2.2.3 Finite Difference

Solving Poisson's equation and the current continuity equation for duct-type geometries using the finite difference method was first introduced by Leutart and Bohlen [32] and later modified by McDonald [33] and Sparks [34].

The method involves dividing the area of interest into a fine grid as shown by figure 2.9.a. Point "O", in figure 2.9.b, is the point of interest for the following discussion. However, once the electric field, potential and charge density are evaluated, the label "O" is moved to a neighbouring point and calculations are repeated. This process is continued until all nodal points are covered.

Both Poisson's equation and the current continuity equation can be written in a difference form and later reduced to give the potential and the charge density at point "O" as shown below.

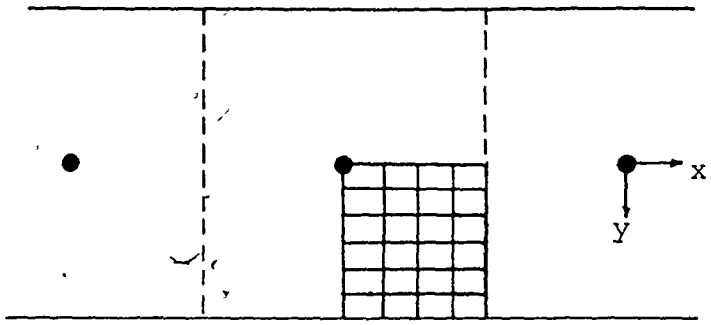

(a) Region of interest to which the numerical technique is applied

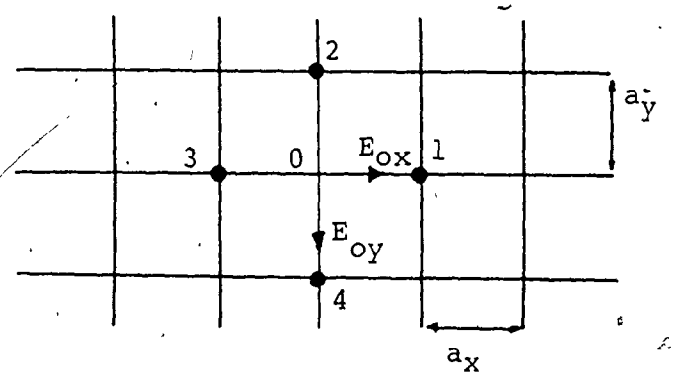

(b) Partial grid

Figure 2.9. Elemental grid structure as applied to finite difference

$$V_o = \frac{1}{2(a_y^2 + a_x^2)} [a_y^2 (V_4 + V_2) + a_x^2 (V_1 + V_3) + a_x^2 a_y^2 \frac{\rho_o}{\varepsilon_o}] \quad (2.16)$$

$$\rho_o = -\frac{\varepsilon_o}{2}[\frac{E_{ox}}{a_x} + \frac{E_{oy}}{a_y}] + 0.5[\varepsilon_o^2 (\frac{E_{ox}}{a_x} + \frac{E_{oy}}{a_y})^2 + 4\varepsilon_o (\frac{E_{ox}\rho_2}{a_x} + \frac{E_{oy}\rho_3}{a_y})]^{\frac{1}{2}} \quad (2.17)$$

The steps of the numerical procedure may be outlined as follows:

1- Assign initial values to V at every point, as well as ρ at the corona wire.

2- Compute ρ at every point using equation (2.17).

3- Re-compute V at every point using equation (2.16).

4- Repeat steps 2 and 3 alternately until the desired convergence is achieved on V at every point.

5- Check to see if the computed current density (J=ρbE) equals the measured current density. If they do not agree, readjust ρ at the corona wire and repeat all the above.

The finite difference method was applied to Matick's geometry [31] and compared to his experimental data. Figure 2.10 gives the voltage distribution along a line extending from wire to plate using different grid sizes. It is interesting to observe that as the number of elements are increased, the results tend to deviate away from the

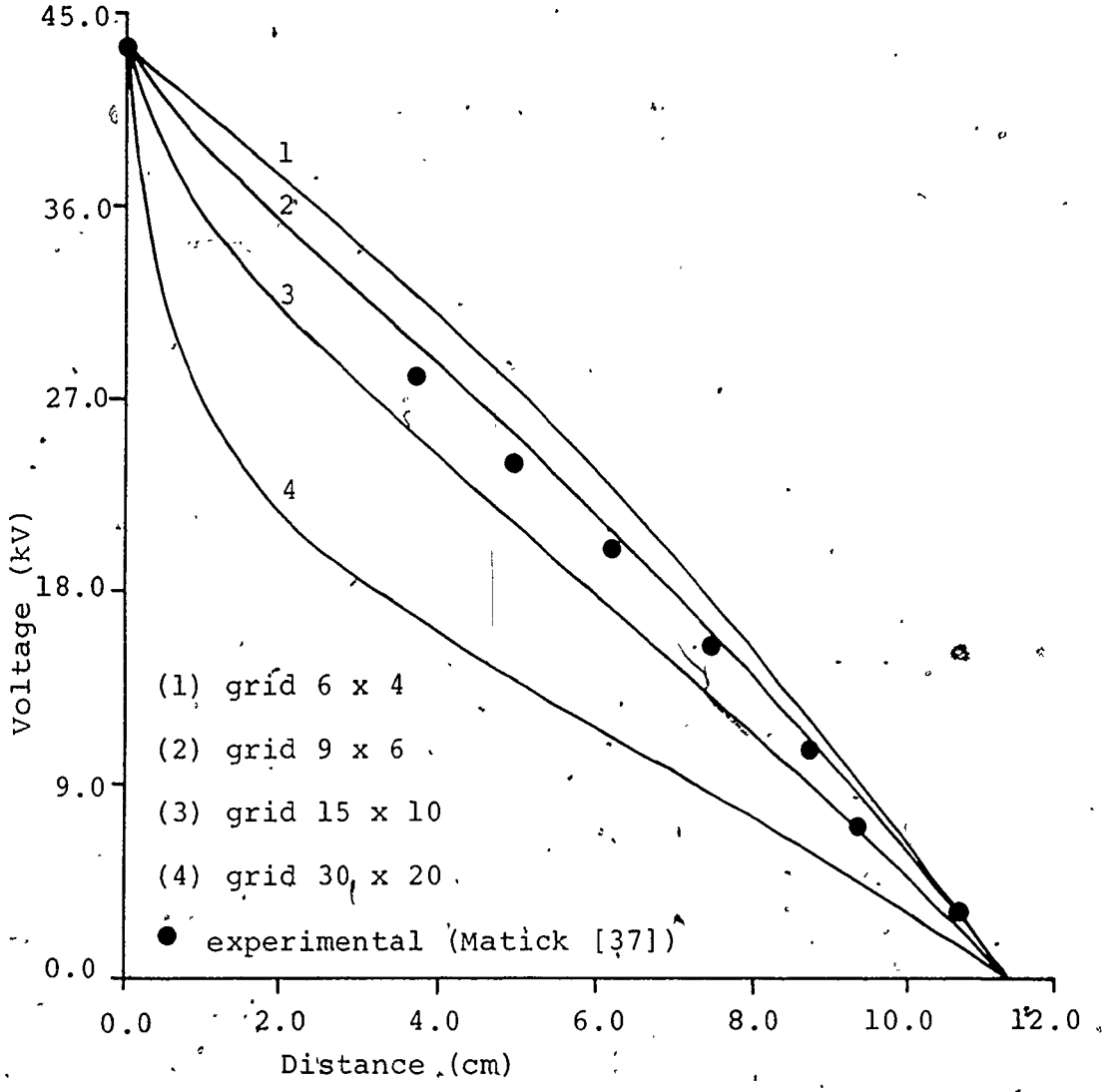

$h = 0.11$ m $\quad V_c = 43.5$ kV

$s = 0.076$ m $\quad J_\ell = 0.48$ mA/m

$r_c = 0.15$ mm $\quad b = 2.2 \times 10^{-4}$ m^2/V.s

Figure 2.10. Voltage distribution along a line extending from wire to plate using finite difference

experimental data. This contradicts the well known fact in finite difference theories [35], that the accuracy of the technique increases as the number of elements are increased, as long as round-off errors are not encountered.

This deviation is believed to be the result of the insufficient accuracy in modeling the region next to the corona wire, where rapid changes in electric field and charge density occur. This is more clearly realized when considering the relatively large element sizes used (3.7x3.7 mm for the 30x20 grid and 18.3x18.3 mm for the 6x4 grid), as compared to the wire radius (in this case 0.15 mm).

This view is also shared by other investigators [24, 36]. Using a successive graded mesh, with the smaller elements adjacent to the corona wire and the successive larger elements next to the collecting plate [37], would probably eliminate this deviation.

The SRI computer model for electrostatic precipitators [38] uses the finite difference method. In their model they used a grid of 15x10, which coincidently gives results in good agreement to the experimental data (refer to figure 2.10). Although the developers of this package agree that the finite difference method in its present form is not suitable for modeling the region close to the corona wires,

they claim that it is sufficiently accurate for evaluating the electric field at the collecting walls provided that a mesh of about 15x10 elements is used [39]. This appears to be the case, since when observing figure 2.11 which gives the electric field distribution at the collecting plate using different grid sizes, the average electric field along the plate for a grid of 15x10 is equal to 3.6 kV/cm. This value corresponds reasonably well to the value of 3.9 kV/cm evaluated by the common approximation [40] (E at the plate= V_c/h).

2.2.4 Finite Element

The finite element method was recently applied to the duct precipitator geometry in 1983 by Davis and Hoburg [41] and later in 1984 by Kallio and Stock [36].

In this technique, the region of interest is divided into a grid structure (usually of triangular elements), in such a manner that the elements adjacent to the corona wire are small and they gradually increase in size as they approach the collecting plate. The area ratio of the largest element to the smallest element is in the order of 10^3.

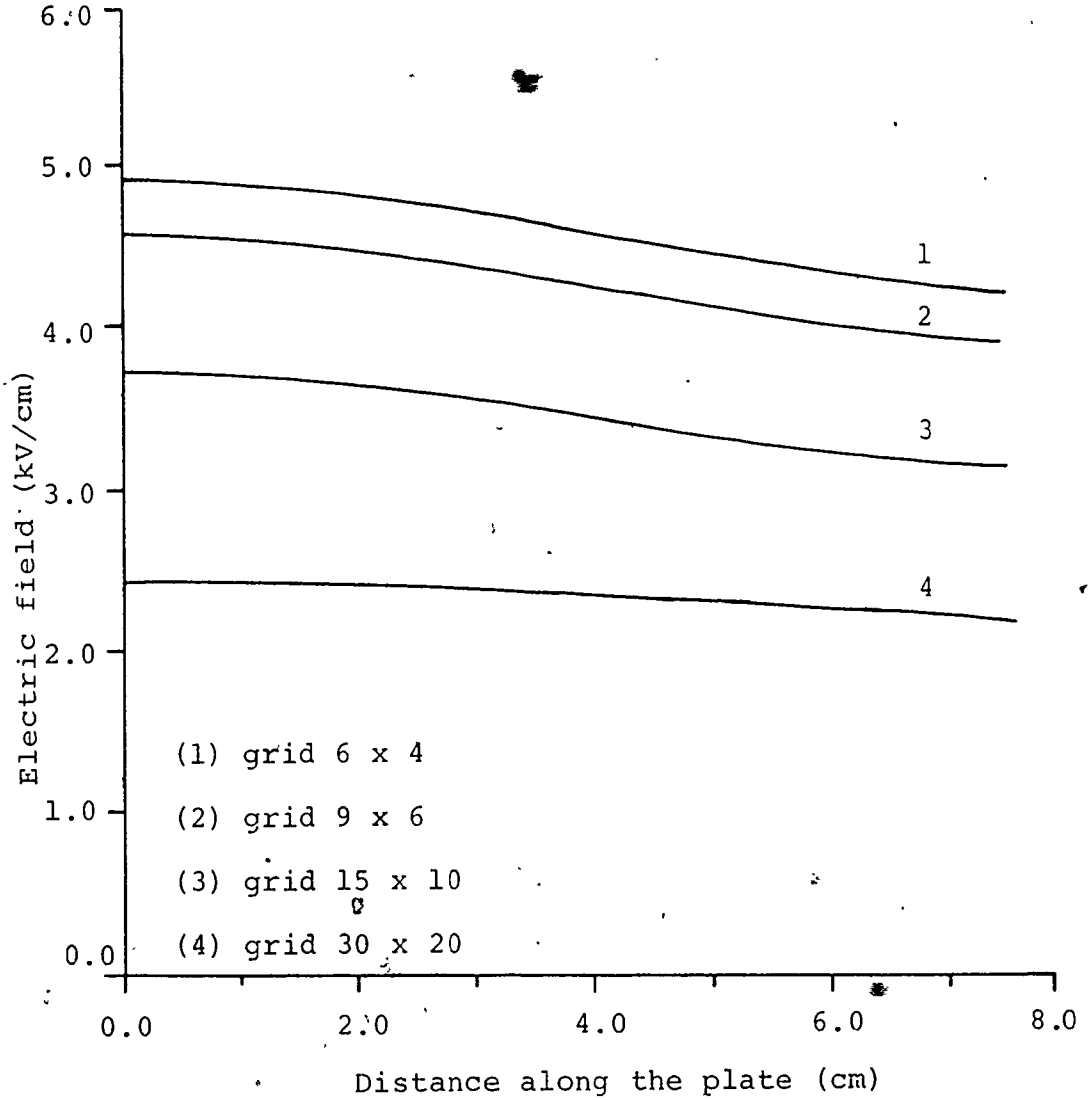

h = 0.11 m V_c = 43.5 kV

s = 0.076 m J_ℓ = 0.48 mA/m

r_c = 0.15 mm b = 2.2 x 10^{-4} $m^2/V.s$

Figure 2.11. Electric field distribution along the collecting plate using finite difference

The finite element procedure involves assigning potential values to each node, as well as assigning conditions of potential and electric field at the boundaries. Later the charge density at each node is evaluated, either using the characteristic method [41] or the finite difference method [36], then the potential is evaluated at the same points using the finite element method. Alternate calculations of potential and charge density are performed until convergence is achieved. Further details of the finite element and the characteristic methods are given in Appendix 2.

As mentioned earlier, the finite element method was the only numerical procedure not formulated (programmed) by the author. Thus the results and the conclusions cited here are those of Davis et al. [41] and Kallio et al. [36].

All the results presented by Davis and Hoburg were limited to comparing their finite element - characteristic method model to the experimental measurements of potential distribution conducted by Penney and Matick.[31]. Their model showed good agreement with the experimental data for the different precipitator geometries and the different operating voltages investigated. Unfortunately, in their work they did not present any other electrical distributions, such as electric field, current density or charge density. This makes it difficult to fairly evaluate

the technique in terms of validity and accuracy.

The work presented by Kallio and Stock was based on comparing their finite element - finite difference model to the absolute finite difference model developed by McDonald et al. [38], for approximately the same number of nodal points.

In this work, they showed that their model was more accurate than McDonald's, by comparing both of them to the experimental results of Penney and Matick. This better accuracy was attributed to the use of higher nodal density next to the corona wire.

They also showed that the computational time required was approximately three times larger for the finite element model as compared to the finite difference model.

Since they were using finite difference for solving the continuity equation, ie. for evaluating the charge density distribution, they obtained charge density profiles similar to those obtained by McDonald's model. They considered this a weak point, and suggested for future work that another method be implemented for solving the continuity equation rather than the finite difference method. This supports the use of the characteristic method as used by Davis.

2.2.5 Comments

From the previous analysis presented in sub-sections 2.2.1 to 2.2.4, regarding the electrical conditions in duct-type precipitators, the following conclusions can be made.

1- The general shape of the V-I characteristics may be estimated using equations (2.3) and (2.7), bearing in mind that these equations are only approximate solutions of Poisson's equation and the current continuity equation.

2- The conformal transformation technique is another method for obtaining the general shape of the V-I characteristics, but it is not recommended for predicting the electrical conditions in the inter-electrode gap.

3- The finite difference method in its current form as presented in sub-section 2.2.3, is not sufficiently accurate. The accuracy of the technique may be enhanced by using a successive graded mesh.

4- The finite element method appears to be the most accurate and reliable technique, although further improvement is necessary in the method of evaluation of the charge density. A drawback of this method is that it requires relatively long computational time compared to the other methods.

It is apparent from the previous discussions, that numerical methods seem to be the most appropriate approach in terms of reliability and accuracy for solving Poisson's equation and the current continuity equation for the duct precipitator geometry.

However, comparing the finite difference and the finite element techniques indicates that there are certain limitations:

i) Both techniques are iterative and alternate between Poisson's equation and the current continuity equation as opposed to solving them simultaneously.

ii) Both techniques require the pre-construction of a fixed grid.

iii) Both techniques require proper initial guesses for quick successful convergence.

iv) Both techniques, because of their iterative nature, require considerable computational time, particularly if high accuracy is sought.

To overcome the above difficulties, it was decided to use a different numerical approach which is based on the charge simulation technique. Although the charge simulation technique is basically a numerical method, it results in an analytical expression for the potential and field quantities of interest, expressed in terms of a number of fictitious charge distributions. This is further

explained in the following section.

2.3 Charge Simulation Technique

The technique was orginally developed [43,20] to solve Laplacian field problems. It is based on the replacement of the conductor surface charges by discrete fictitious charges. These charges in Laplacian field problems are placed outside the region where the solution is sought, and their magnitudes are evaluated such that their integrated effect satisfies the boundary conditions at a selected number of points on the conductor surfaces.

The choice of the type of charges depends on the geometry. Three major forms of charges have been found to cover almost all possible needs of simulation [20], these are: point charges, infinite and finite line charges and finally uniform and non-uniform ring charges. Specific attention will be given to infinite line charges, since these best satisfy the boundary conditions for the duct geometry.

2.3.1 Electric Potential and Field due to an Infinite Line Charge

Consider an infinite line charge of uniform charge density per unit length (q) positioned at a point (x_i, y_i) as shown in figure 2.12.a. The potential V at any point (x,y) due to this charge is given as [20].

$$V(x,y) = \frac{q}{4\pi\varepsilon_o} \ln \frac{1}{\sqrt{(x - x_i)^2 + (y - y_i)^2}} \qquad (2.18)$$

Similarly the electric field components E_x and E_y at the same point may be evaluated using equations (2.19) and (2.20) respectively.

$$E_x = \frac{q}{2\pi\varepsilon_o} \frac{x - x_i}{(y - y_i)^2 + (x - x_i)^2} \qquad (2.19)$$

$$E_y = \frac{q}{2\pi\varepsilon_o} \frac{y - y_i}{(y - y_i)^2 + (x - x_i)^2} \qquad (2.20)$$

2.3.2 Illustrative Example of the Charge Simulation Technique

Consider two parallel infinite plates such as those shown in figure 2.12.b. The upper being at potential V, while the lower is grounded. To apply the charge simulation technique to solve for the Laplacian field between the two plates, replace the upper surface charges by a set of discrete line charges of unknown values (q_1 ..... q_{m-1}), similarly replace the lower surface charges by another set (q_m ..... q_n). Select a set of (n) boundary

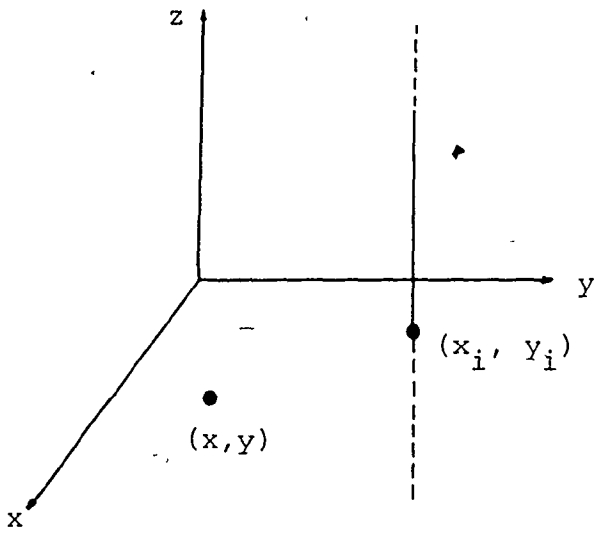

(a) Schematic of infinite line charge perpendicular to the x-y plane

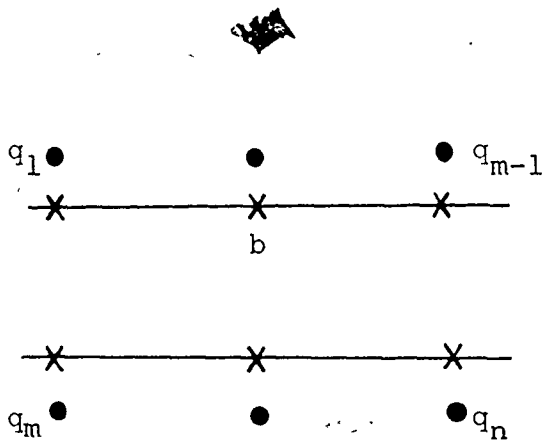

(b) Location of charges and boundary points for modeling two infinite parallel plates

Figure 2.12. Infinite line charges as used in the charge simulation technique

points on the two surfaces (a, b ..... n). Those points selected on the upper surface are assigned a potential V and the lower points are assigned a zero potential.

The potential at point (a) due to the set of (n) charges is given as.

$$V(a) = V = \frac{1}{4\pi\varepsilon_o} \sum_{i=1}^{n} q_i \ln \frac{1}{d_{a-i}} \qquad (2.21)$$

where d_{a-i}, is the distance between point (a) and the ith charge.

The potential at the remaining boundary points can be written in a manner similar to that of equation (2.20). Thus a set of (n) linear equations with (n) unknowns are developed. Those can be written in a matrix form as shown by equation (2.22), and solved by Gauss elimination [44] for the unknown vector of charges q_i.

$$\begin{bmatrix} \text{Potential} \\ \text{Cofficient} \\ \text{Matrix} \\ \\ \\ \end{bmatrix} \begin{bmatrix} q_1 \\ q_2 \\ \\ \\ q_n \end{bmatrix} = \begin{bmatrix} V_a \\ V_b \\ \\ \\ V_n \end{bmatrix} \qquad (2.22)$$

When applying the charge simulation technique to a particular problem, the choice of the number of charges and their locations relative to the simulated electrode has no specific rules.

Concerning the number of charges, one would initially select a small number of charges and progressively increase the number until a predetermined accuracy level is achieved. One method of determining the accuracy of a developed model is to evaluate, at several points on the boudary, the percentage error of the calculated potential with respect to the actual electrode potential. These points should be different than the preselected boundary points. Another method of determining the accuracy is to evaluate the ratio of tangential to perpendicular field components at selected points along the electrode boundary. This ratio is physically equal to zero. In the literature, if the percentage error of the calculated potential and/or the ratio of the previously mentioned electric field components is less than 1%, the model is regarded as being successful.

As for the location of the charges, it has been found from general experience [51], including the author, that if the ratio of the distance between adjacent charges and the distance between any charge and its corresponding boundary point is in the range of 0.75 to 1.25 then satisfactory accuracy is achieved.

2.3.3 Modeling of Space Charge Using Charge Simulation

The idea of using the charge simulation technique to model space charge was first introduced in 1974 [20]. Initially the technique was used for modeling a known or an assumed space charge distribution [45,46]. Later in 1980 Horenstein [47] used the charge simulation technique to model an unknown space charge distribution. This was performed to study the electrical conditions persisting around a single D.C. transmission line.

Further details of implementing the charge simulation technique to model space charge are given in the following chapters.

CHAPTER THREE

CHARGE SIMULATION TECHNIQUE AS APPLIED TO CYLINDRICAL TYPE ELECTROSTATIC PRECIPITATORS

3.1 Introduction

The charge simulation technique is used here as a method to model the electrical characteristics of a coaxial type electrostatic precipitator. Analytical solutions for both Laplace's and Poisson's equation are available in the literature for the coaxial geometry. However, modeling this geometry by the charge simulation technique is desirable to check the validity of the technique with the intent of extending it to the parallel plate geometry which does not have an analytical solution.

Two models will be presented in this chapter. The first represents the electrostatic case where no space charge exists, while the second represents the corona case in clean air.

3.2 The Electrostatic Model

For a coaxial wire-cylinder geometry, if the voltage applied to the wire is less than the corona onset voltage, then the problem becomes an electrostatic one with zero space charge in the inter-electrode gap. This reduces Poisson's equation to Laplace's equation which is given below.

$$\nabla^2 V = 0 \tag{3.1}$$

Using cylindrical co-ordinates, and assuming an infinitely long coaxial system, then the problem becomes only one dimensional in the radial direction (r), and the solution of equation (3.1) yields [49].

$$E(r) = \frac{V_c}{r \ln(r_o/r_c)} , \tag{3.2}$$

The voltage at any radial distance (r), is given as shown below.

$$V(r) = V_c - \int_{r_c}^{r} E(r)dr \tag{3.3.a}$$

$$= V_c \left[1 - \frac{\ln(r/r_c)}{\ln(r_o/r_c)}\right] \tag{3.3.b}$$

When using the charge simulation technique to model cylindrical type precipitators, the problem was solved using a two co-ordinate system V(x,y) rather than a one co-ordinate system V(r). The reason for this was to be able to use the same modeling technique for the parallel plate geometry which is physically two dimensional (in the

x-y plane).

The problem was greatly simplified due to the double symmetry and thus a solution was only required in one quadrant as seen in figure 3.1. This figure is only a schematic diagram and does not include the actual number of line charges used in the simulation routine. Although the solution was only sought in the first quadrant, the mirror charges in the remaining three quadrants were taken into consideration when evaluating the potential or the electric field at any point within the shaded area.

In the electrostatic model developed, the wire surface charges were replaced by 8 infinite line charges (in the first quadrant), those were placed inside the wire on a circular circumference of radius equal to one half the wire radius r_c. The image charges of the outer grounded cylinder, were replaced by 31 infinite line charges (in the first quadrant) placed outside the outer cylinder. The 39 boundary points, necessary for evaluating the unknown charges, were located such that the ratio S_1 to S_2 was approximately unity as suggested by Malik [51]. This particular ratio was tested by comparing it to other ratios of higher and lower values, it proved to give reasonable accuracy for a fixed number of charges. To obtain the best accuracy optimization techniques would have to be used [52,53]. The 8 boundary points located at the wire were

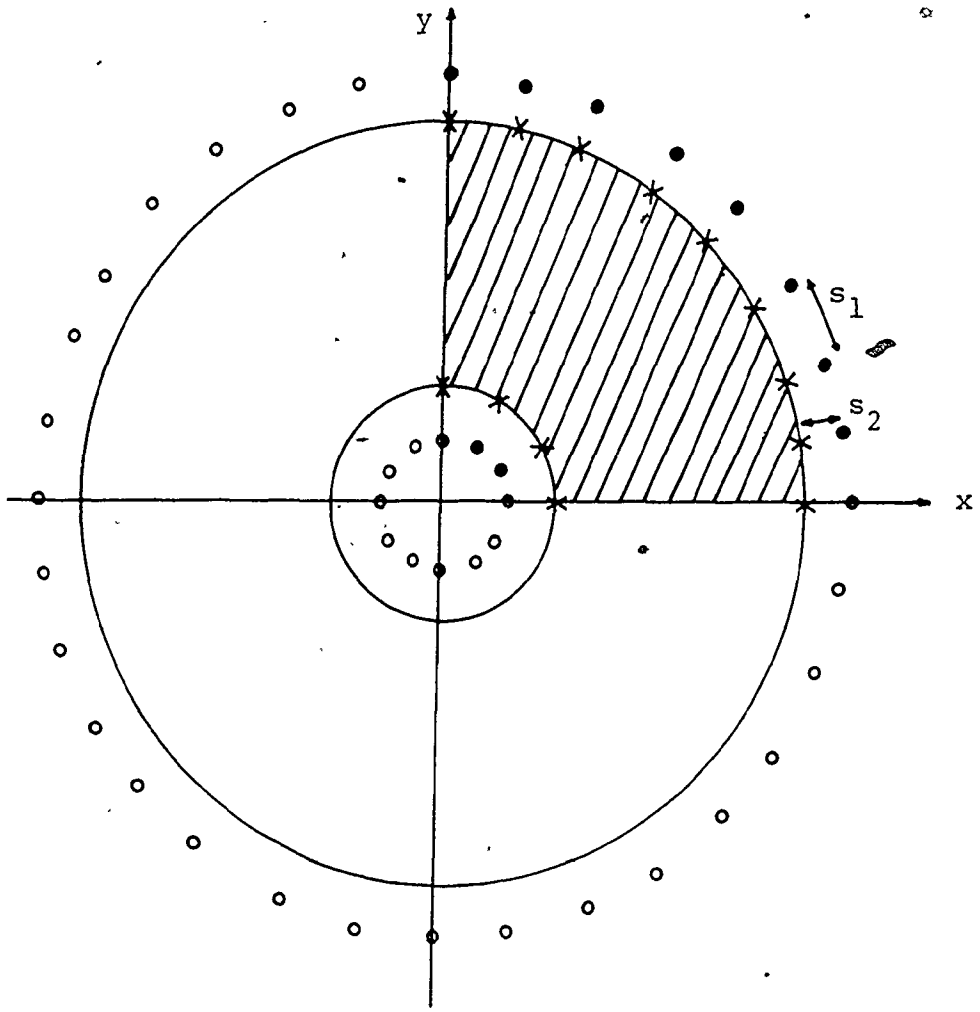

• infinite line charges and their images in the first quadrant

o infinite line charges and their images in the remaining quadrants

x boundary points

Figure 3.1. Location of line charges and boundary points for the electrostatic model of the cylindrical geometry

assigned a potential V_c (a value lower than the corona onset voltage V_o), while the remaining 31 boundary points at the grounded cylinder were assigned zero potential. The potential coefficient matrix was constructed using equation (2.18), and the Gaussian elimination method was used for solving the matrix equation (3.4), for the unknown charges.

$$[PC]_{39x39}\ [Q]_{39} = [V]_{39} \qquad (3.4)$$

where [PC]= potential coefficient matrix, [Q]= magnitudes of unknown charges, and [V]= potential at boundary points.

The electrostatic model was applied to an arbitrary coaxial geometry and the results were compared to the analytical voltage and field distributions evaluated using equations (3.3) and (3.2) respectively. The good agreement of the simulation results to the analytical results is illustrated by figures 3.2 and 3.3.

3.3 The Corona Model in Clean Air

In a coaxial cylindrical geometry, if the voltage applied to the wire is higher than the corona onset voltage, the gas surrounding the wire becomes ionized and a space charge is created in the inter-electrode gap as explained in chapter one. The analytical equations governing the unipolar region for this case are Poisson's equation (3.5) and the current continuity equation (3.6), the latter is given in it's integral form.

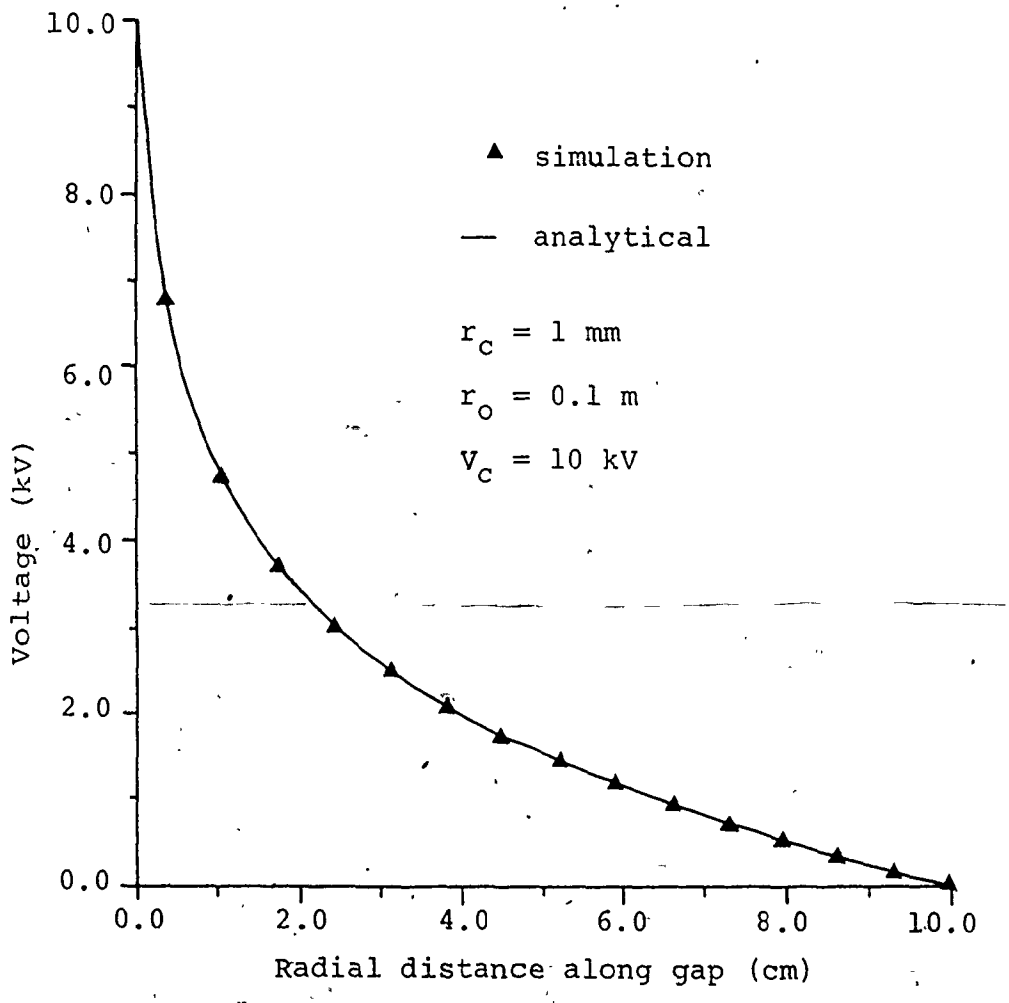

Figure 3.2. Electrostatic voltage distribution in a cylindrical geometry using charge simulation

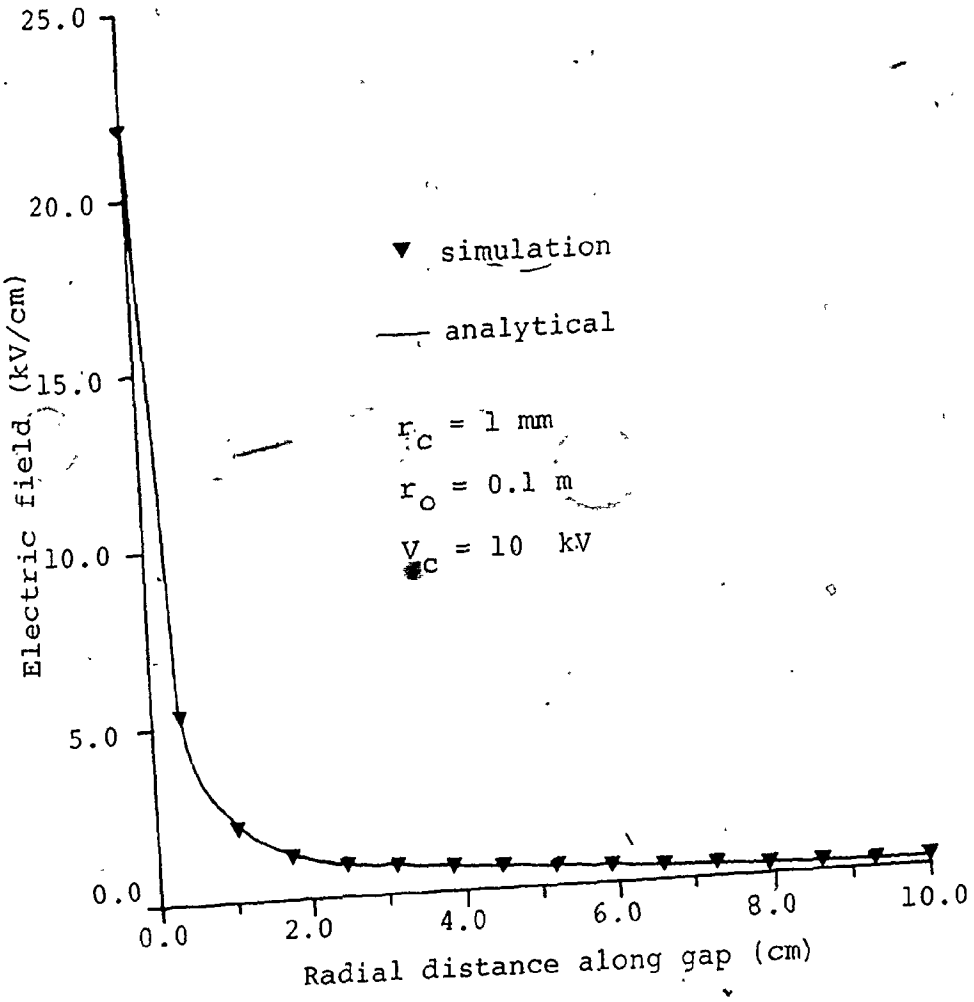

Figure 3.3. Electrostatic field distribution in a cylindrical geometry using charge simulation

$$\nabla^2 V = - \frac{\rho_i}{\varepsilon_o} \qquad (3.5)$$

$$\oint J.dA = I_c \qquad (3.6)$$

The complete solutions of equations (3.5) and (3.6), using cylindrical co-ordinates are given in Appendix 3 [52], from which the following two equations were extracted.

$$E(r) = \left[\left(\frac{r_o}{r}\right)^2 E_o^2 + \frac{J_\ell}{2\pi\varepsilon_o b} \left\{1 - \left(\frac{r_o}{r}\right)^2\right\} \right]^{\frac{1}{2}} \qquad (3.7)$$

$$\rho_i(r) = \frac{\sqrt{r_c E_o \varepsilon_o \rho_e}}{\sqrt{r^2 + K_2^2 - r_c^2}} \qquad (3.8)$$

where $$\rho_e = \frac{J_\ell}{2\pi r_c b E_o} \qquad (3.9)$$

and $$K_2 = \sqrt{\frac{E_o \varepsilon_o r_c}{\rho_e}} \qquad (3.10)$$

Equation (3.7) gives the radial electric field distribution and equation (3.8) gives the radial ionic charge density (ρ_i) distribution. To evaluate the voltage distribution, equation (3.3.a) may be used.

The above analytical equations provide the means for checking the validity and the accuracy of the corona in clean air model developed using the charge simulation technique.

Two commonly used assumptions were applied to the corona model, these are:

i- The corona ionization sheath is neglected and the wire is considered a uniform ion emitting source. This assumption is based on the fact that the thickness of the ionization zone is usually only one to two times the wire radius [4,55].

ii- The electric field at the surface of the conductor in corona remains constant at the onset value E_o [56,57].

The general shape of the V-I characteristics for a coaxial geometry is given by figure 3.4. The voltage V_c required to sustain a corona current level I_c, can be considered to be composed of two components V_o and ΔV_c. Thus the discrete infinite line charges used in the simulation were divided into two sets.

The first set, which will be referred to as the onset charges (including the onset image charges), was placed outside the region where the solution was sought (refer to figure 3.5) and in a similar arrangement to that of the electrostatic model. The onset charges were evaluated such that their magnitudes satisfied the following boundary conditions.

$$V(r=r_c) = V_o = E_o r_c \ln(r_o/r_c) \qquad (3.11)$$

$$V(r=r_o) = 0 \qquad (3.12)$$

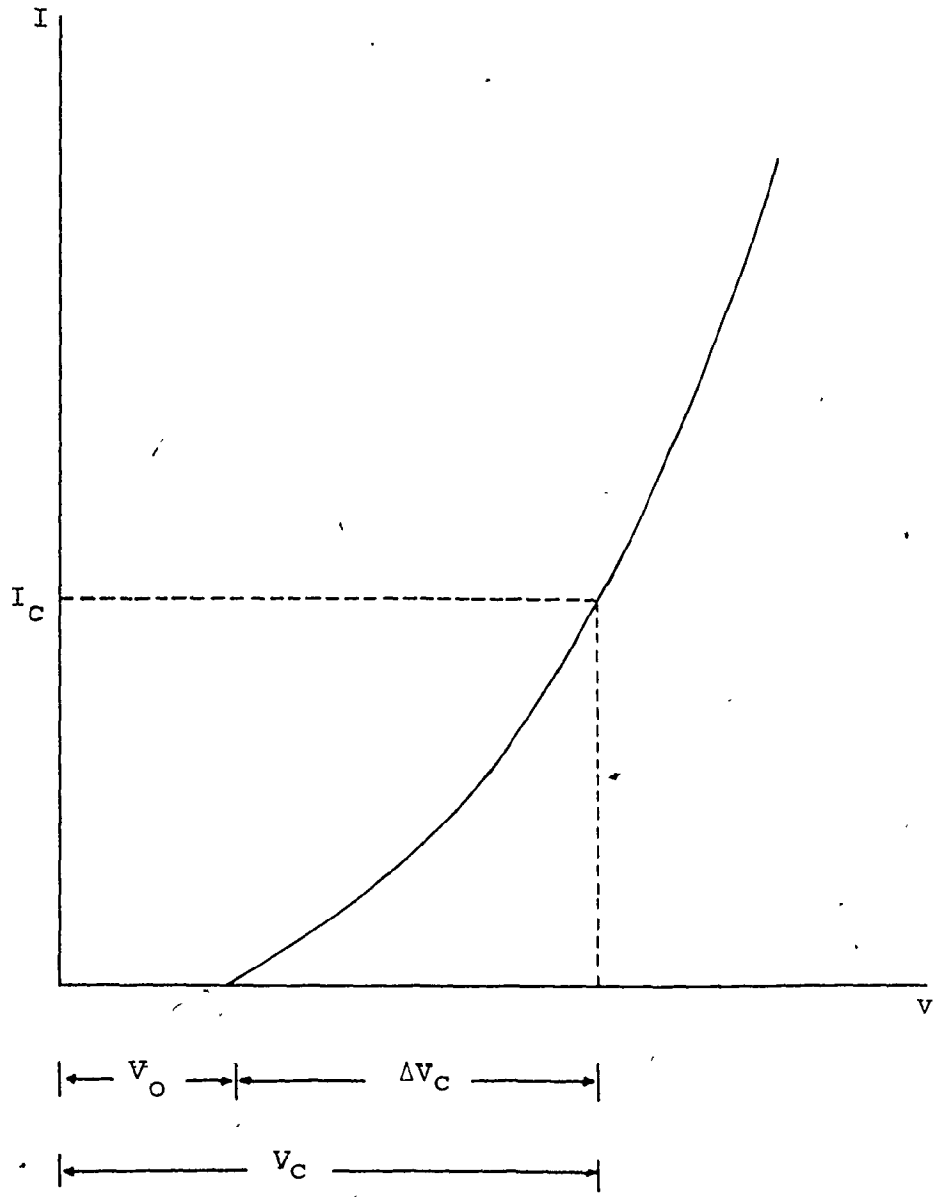

Figure 3.4. Typical V-I characteristics for coaxial geometry

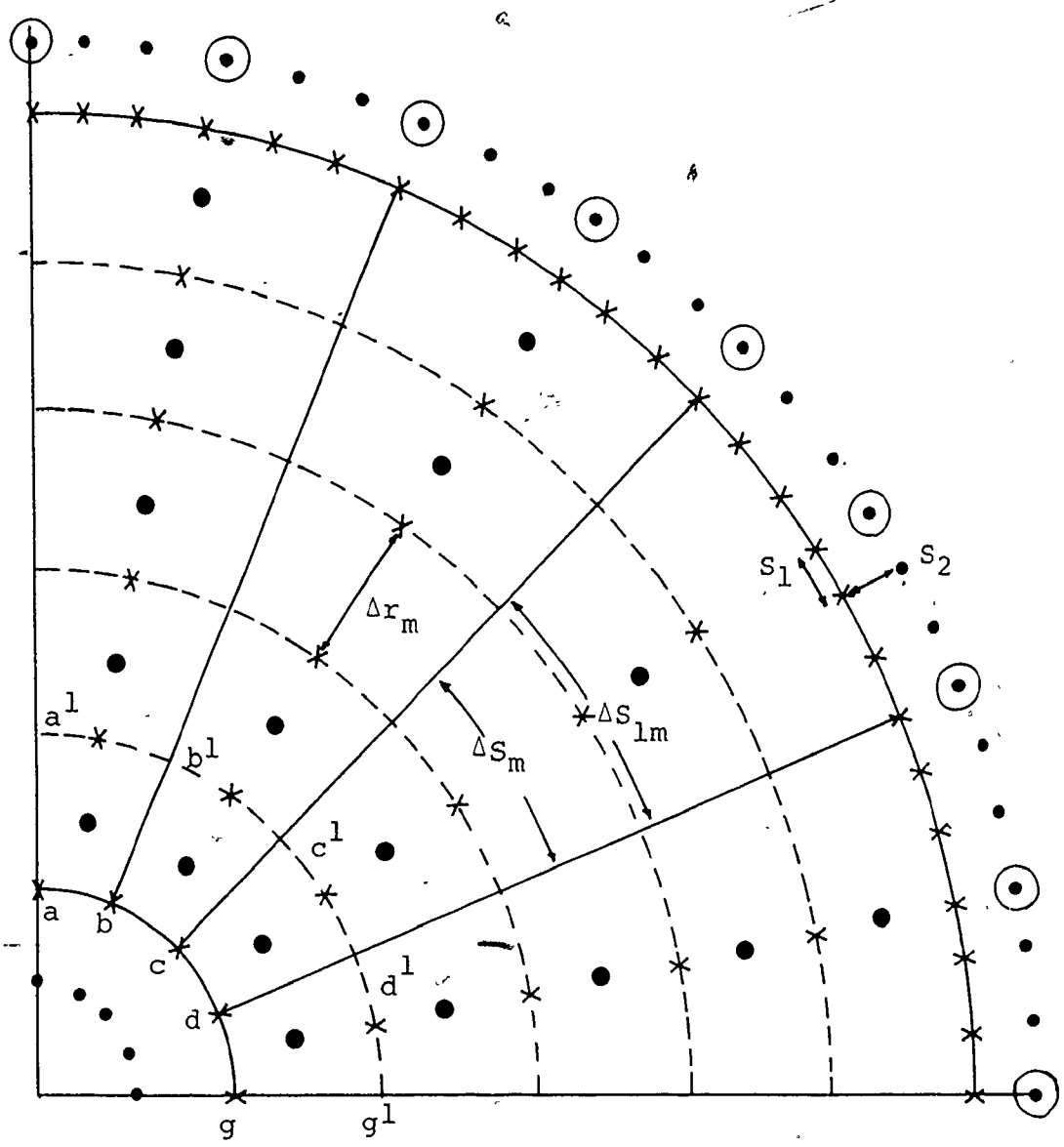

Figure 3.5. Location of simulation charges and boundary points in the corona model for clean air

The second set of charges was placed inside the region where the solution was sought as shown by figure 3.5. These charges represented the ionic space charge and their magnitudes were evaluated such that they contributed a potential ΔV_c to the corona wire and zero potential to the grounded cylinder.

The integrated effect of both set of charges had to satisfy the boundary conditions given by equations (3.13), (3.14) and (3.15) as well as the current continuity equation (3.6).

$$V(r=r_c) = V_c \tag{3.13}$$

$$V(r=r_o) = 0 \tag{3.14}$$

$$E(r=r_c) = E_o \tag{3.15}$$

To evaluate and locate the ionic space charge a method similar to the one presented by Horenstein [47] was used. The method was based on finding a set of 20 equipotential charge shells (contours) by extending 7 trajectories or lines of field (refer to figure 3.5) from the conductor surface to the outer cylinder.

Since the electric field, potential and charge density tend to change more rapidly in the vicinity of the corona wire, thus the elements adjacent to the corona wire were choosen to be smaller in size with respect to those adjacent to the outer collecting wall. This was achieved by varying the spacing between equipotential contours. The first ten equi-potential contours were equispaced by a distance equivalent to 3.3% of the inter-electrode gap, while the remaining ten contours were equispaced by a distance equivalent to 6.7% of the inter-electrode gap.

Note that because of the continous space charge in the inter-electrode gap, the electric field is governed by Poisson's equation. But since in this technique the continous space charge is simulated by discrete infinite line charges. Then the effect of the resulting space charge field may be arrived at by summing the potential and electric field contributions caused by each discrete infinite line charge.

The first equipotential shell was located by using only the onset charges and calculating the voltage drop along the trajectories starting from the initial points (a, b, ... g) to the points (a^1, b^1, ... g^1) which are equipotential with respect to the wire surface.

Then, 6 discrete charges q_{im}, representing the ionic charges in the first shell and located at the geometric centers of the elements, were calculated such that they satisfied an arbitrary voltage V_a at the 6 boundary points located mid-way between the points (a^1, b^1, ... g^1). The potential V_a at any boundary point due to the six discrete charges was evaluated using equation (3.16).

$$V_a = \sum_{m=1}^{6} \frac{q_{im}}{2\pi\varepsilon_o} \ln \frac{1}{d_{im}} \qquad (3.16)$$

where d_{im} is the distance between the boundary point and the mth ionic charge.

At the same time, these q_{im} charges had to satisfy the continuity equation in discrete form which is presented by equation (3.17).

$$J_\ell = I_c/L = \sum_{m=1}^{6} \frac{q_{im}}{\Delta r_m \Delta S_m} b_i E_m \Delta S_{lm} \qquad (3.17)$$

Next, a set of 11 ground image charges were evaluated so as to continuously satisfy the boundary condition given by equation (3.14).

After the ionic line charges of the first shell and their associated ground images were found, their voltage and field contributions were included with the onset charges in integrating out towards the next shell and so on for each shell until the entire gap is filled with the 20 shells. A summarized flow chart of the simulation program developed is given in Appendix 4.

The results of using the corona in clean air model, for a coaxial geometry having an inner and outer radii of 1 mm and 0.4 m respectively and operated at an arbitrary linear corona current of 1 mA/m, are given in figures 3.6 to 3.9. The onset potential V_o for this geometry was 27 kV.

The analytical and simulation voltage distributions are given in figure 3.6. This figure indicates that the maximum percentage difference between the two methods of calculations is 1.1%, this was observed at the conductor surface. It was observed in similar runs for the same geometry that this percentage difference decreased as the corona current was reduced.

Similarly, analytical and simulation field distributions are given in figure 3.7. For this figure the percentage difference between the two methods of calculations was found to be less than 1%.

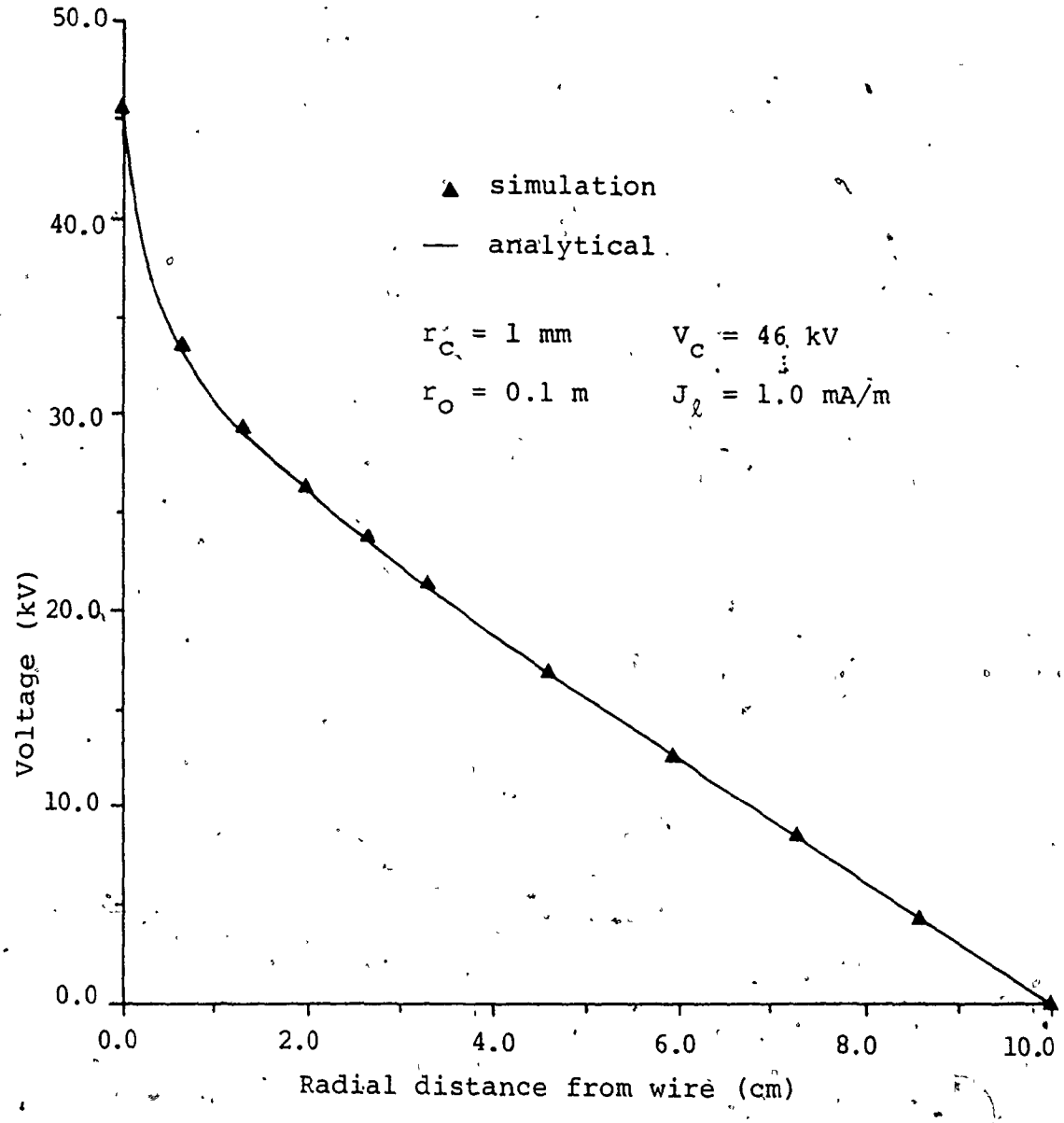

Figure 3.6. Voltage distribution for a cylindrical geometry in the presence of ionic space charge using charge simulation

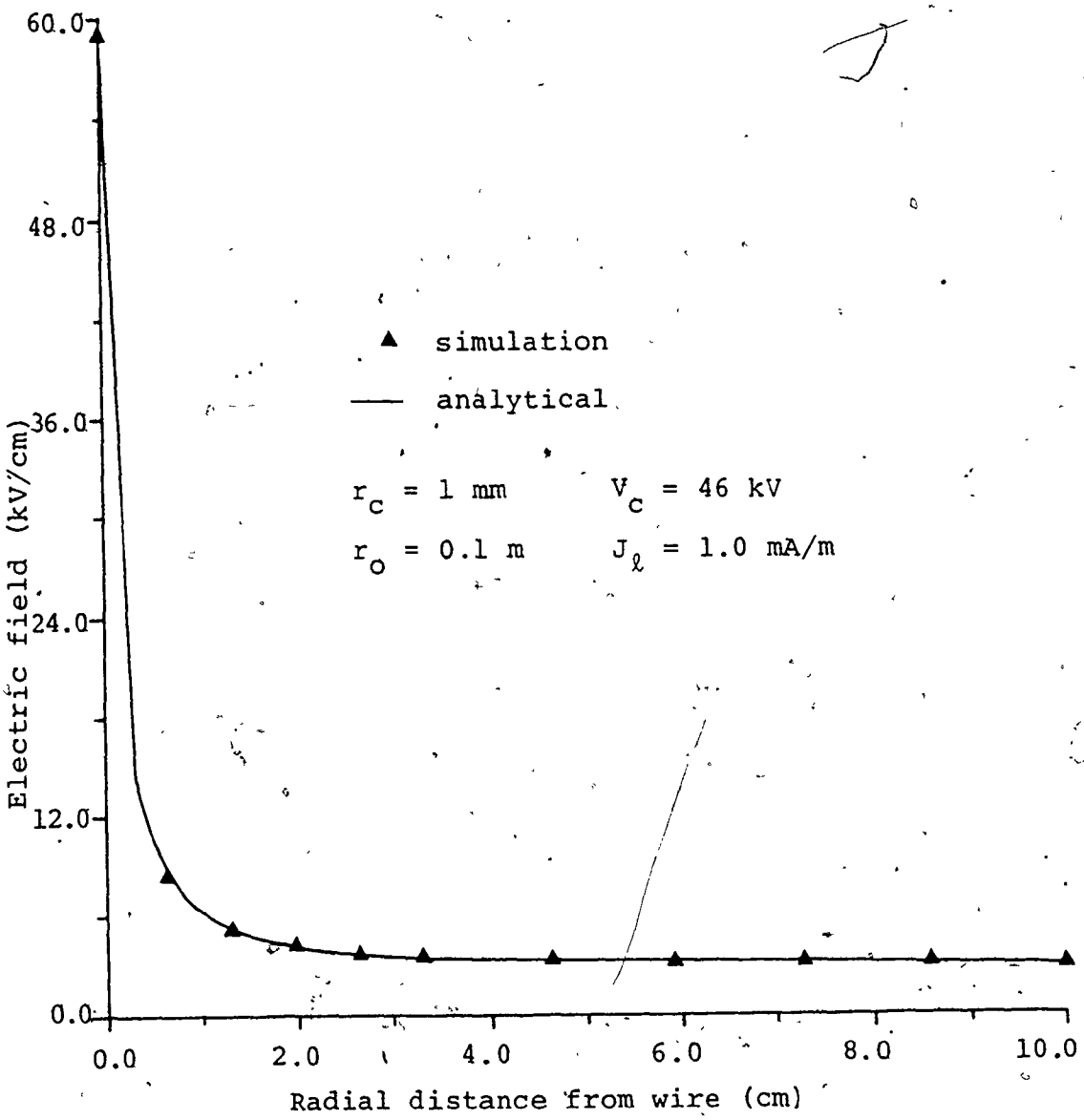

Figure 3.7. Electric field distribution for a cylindrical geometry in the presence of ionic space charge using charge simulation

Figure 3.8 shows the electric field distribution using the simulation routine for two different voltages. The lower curve represents the field when $V_c = V_o = 27$ kV (with zero space charge), while the upper curve represents the field when $V_c = 46$ kV. This figure confirms the validity of the model as it demonstrates the well known phenomenon in electrostatic precipitators, which is the enhancement of the electric field at the outer wall due to the presence of space charge.

Finally, figure 3.9 gives the analytical and simulation charge density distributions. It is observed from this figure that the percentage difference between the two methods of calculations may reach 7%. This may be expected since the charge density in the simulation routine was calculated using equation (3.18).

$$\rho_{im} = \frac{q_{im}}{\Delta r_m \Delta S_m} \qquad (3.18)$$

Equation (3.18) shows that the charge density is a function of the elemental area. Thus for smaller elements higher accuracy can be attained. The size of the elements may be reduced by either increasing the number of equipotential shells, the number of trajectories or both. This would of course involve more computational time.

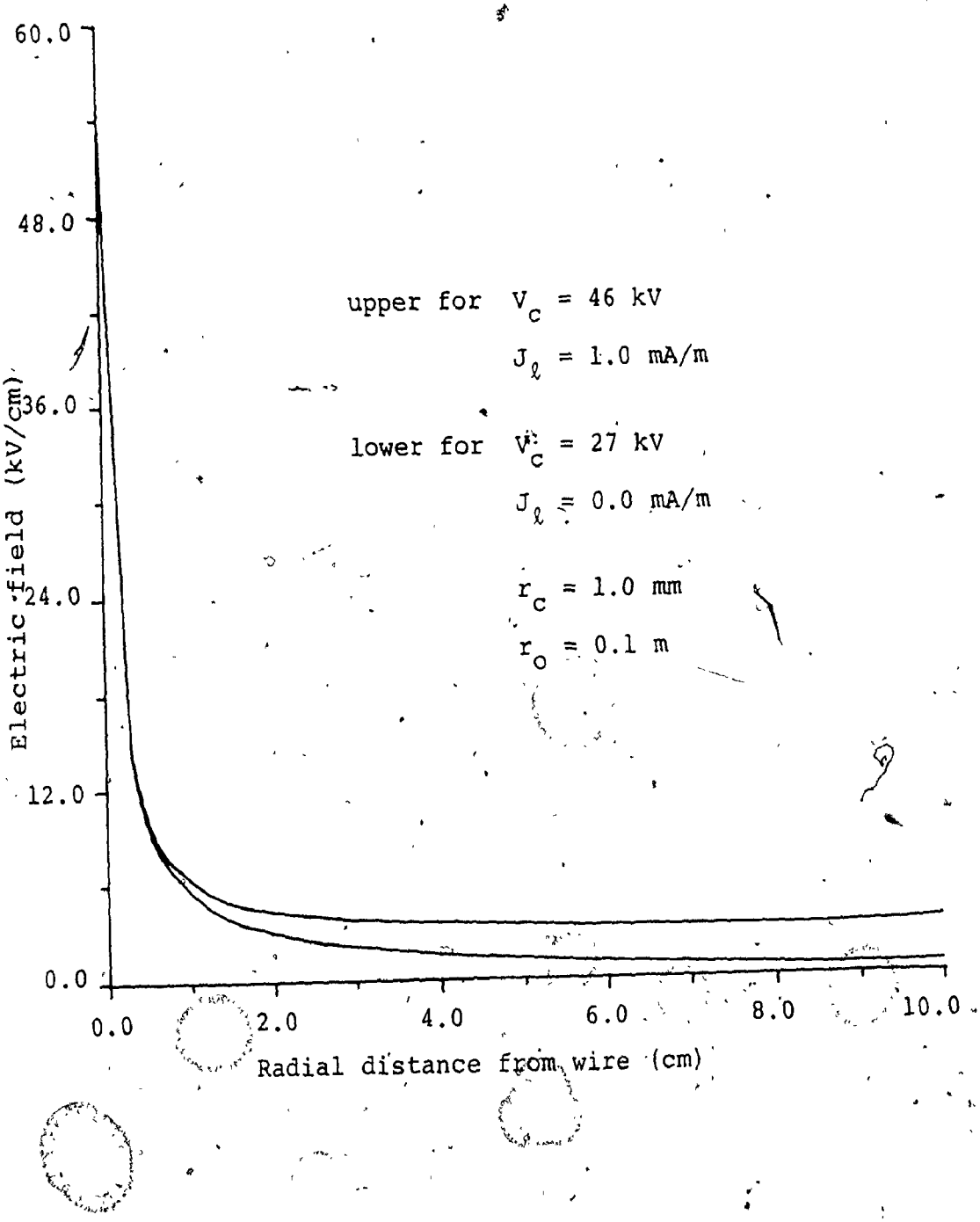

Figure 3.8. Laplacian and Poissonian field distribution in a cylindrical geometry using charge simulation

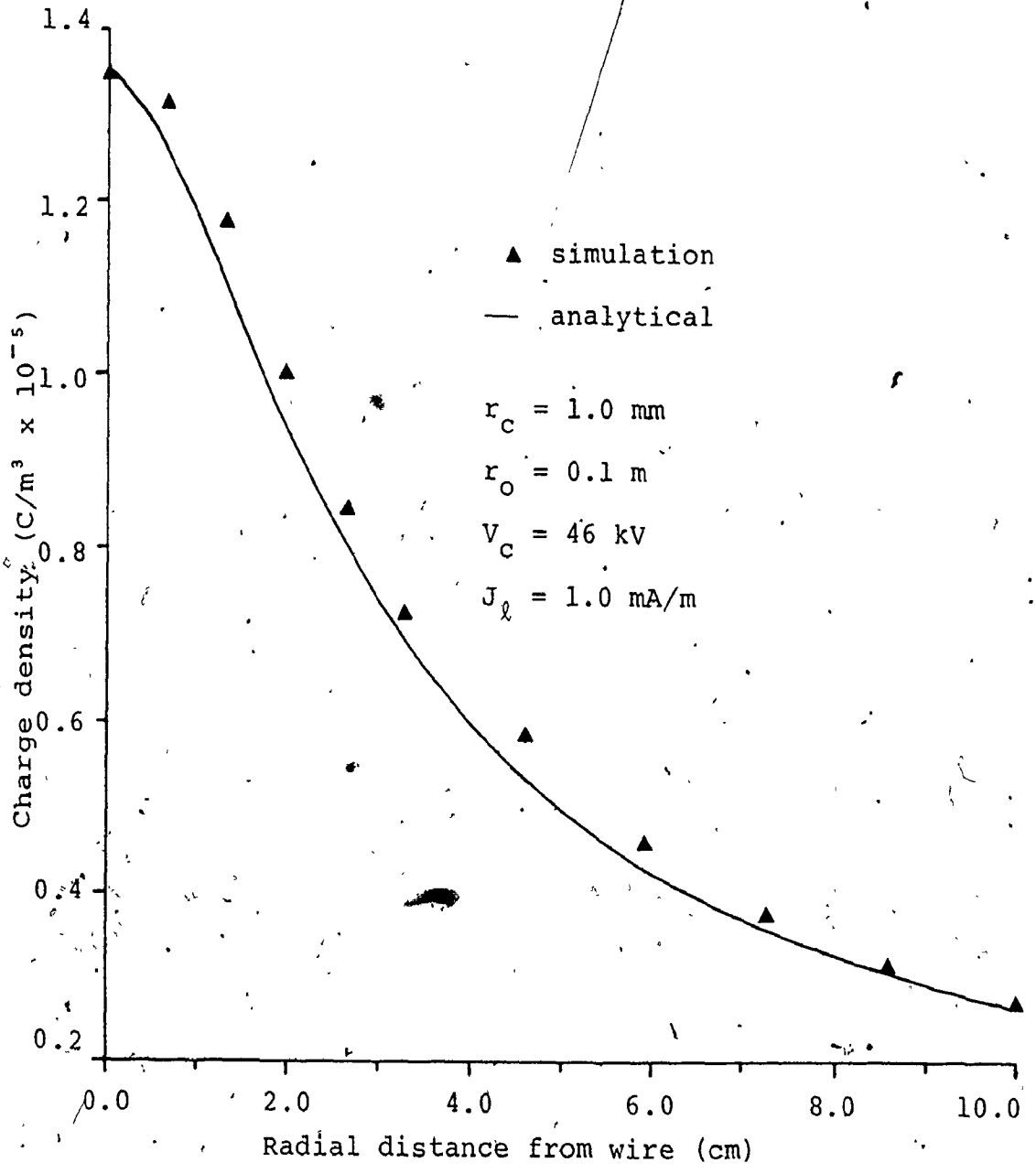

Figure 3.9. Ionic space charge density distribution in a cylindrical geometry using charge simulation

To investigate the effect of neglecting the ionization zone in the corona model, the initial trajectory points a, b, ... g (refer to figure 3.5) were moved further out to a circular circumference of radius equal to $3r_c$. This is equivalent to an ionization zone of thickness $2r_c$. The electric field at this new boundary was equated to the onset field evaluated using Peek's formula for a wire radius of r_c. The final wire potential V_c was evaluated at $r = r_c$ (not $r = 3r_c$).

The above process gave a value of 45.47 kV for the wire potential V_c as opposed to the value of 45.64 kV obtained by the original model which neglects the presence of an ionization zone. No variations were observed, when applying the above process, in the charge density and electric field distributions. This indicates that neglecting the ionization zone and assuming that the corona wire is an ion emitting source is a reasonable assumption.

It is clear from the previous analysis that the charge simulation model predicts well the electrical conditions in clean air for a cylindrical electrostatic precipitator.

The details of the modifications to extend this model to account for particle space charge are given in the next chapter.

CHAPTER FOUR

THE ANALYSIS OF CORONA QUENCHING IN CYLINDRICAL PRECIPITATORS USING CHARGE SIMULATION

4.1 Introduction

An analytical solution of Poisson's equation (4.1) for a coaxial geometry in the presence of corona and particle space charge was originally introduced by Pauthenier [50] in 1932 in the form given by equation (4.2).

$$\nabla . E = \frac{1}{\varepsilon_o} (\rho_i + \rho_p) \tag{4.1}$$

$$E^2(r) = \frac{C}{r^2} \exp(2PSr) - \frac{J_\ell}{4\pi\varepsilon_o b_i} \left[\frac{2}{PSr} + \frac{1}{(PSr)^2} \right] \tag{4.2}$$

Some modifications to the assumptions made by Pauthenier in solving equation (4.1) will be presented in this chapter. Later, the corona quenching model for cylindrical precipitators using the charge simulation technique will be illustrated.

4.2 Modified Solution of Poisson's Equation

Mild corona quenching in electrostatic precipitators is due to the capture of some of the ionic charges and the resulting charging of the dust particles. Thus it is commonly assumed that the linear corona current

density is composed of two components as given by equation (4.3).

$$J_\ell = 2\pi r(\rho_i b_i + \rho_p b_p)E \qquad (4.3)$$

In the classical solution of equation (4.1) the following assumptions were made by Pauthenier:

i) As the wire potential exceeds the corona onset voltage, the field at the wire surface remains constant at its onset value E_o. This assumption is used for evaluating the constant C in equation (4.2).

ii) The particles are charged to their limiting value [5] and their charge density distribution is given as

$$\rho_p = \epsilon_o PE(r)S \qquad (4.4)$$

iii) Since the particle mobility is usually 2 to 3 orders of magnitude less than the ion mobility [59], the corona current was assumed to be essentially carried by the free gaseous ions only, thus eliminating the second term in equation (4.3). This yields the following equation for the ionic charge density distribution.

$$\rho_i = \frac{J_\ell}{2\pi r E b_i} \qquad (4.5)$$

The first assumption is widely accepted in the literature [56,57]. As for the second assumption, it can be seen from equation (4.4) that the particle charge density is a function of the charging electric field E(r). This contradicts the generally accepted assumption in electrostatic precipitators, which is the uniformity of the particle distribution and thus space charge density due to

the turbulent flow in the precipitator cross section. Thus in this model the term E(r) has been replaced by an average charging field E^*_{av} as shown in equation (4.6). This is believed to offer a better representation of the effect of the random distribution of the charged particles.

Equation (4.4) is also based upon the assumption that the particles are fully charged to their Pauthenier saturation limit. In fact, in cases where corona quenching occurs, the charging time constant will be significantly larger than in clean gas conditions. Therefore, one would expect the particles to be charged to only a fraction of the Pauthenier limit. This is represented by assuming a scaling factor ξ, where $0<\xi<1$.

With these modifications equation (4.4) may be rewritten as

$$\rho'_p = \xi\varepsilon_o^{\xi} P E^*_{av} S \qquad (4.6)$$

As for the third assumption, this requires a closer look at equation (4.3). This electrodynamic equation implies that the charged particles behave in a similar way to ions in contributing to the current in the space charge region of the precipitator. However, this contradicts the commonly held assumption that is aerodynamic not electrical forces which govern the particle motion in the duct cross section, such as mentioned earlier about the uniformity of particle space charge due to turbulent remixing. Under

these circumstances the particles will contribute zero net current in the field direction in this turbulent zone and equation (4.3) will only have an ionic component. Thus the second term in equation (4.3) is approximately equal to zero.

On the other hand, equation (4.3) is valid in the region immediately adjacent to the grounded cylinder where the collection of the charged particles contributes a finite current component in the field direction. It is in fact this component which constitutes the collecting action of the precipitator.

Thus the inter-electrode gap may be divided into two zones, the turbulent zone where the charged particles contribute a net zero current in the field direction and a collecting zone adjacent to the collecting walls where the charged particles contribute a finite current component in the field direction.

In the collecting zone, the ionic charge density will be given by equation (4.7) rather than equation (4.5) to account for the current contributed by the charged particles,

$$\rho_i' = \frac{J_\ell - 2\pi r E b_p \rho_p'}{2\pi r b_i E} \qquad (4.7)$$

Sustituting equations (4.5) and (4.6) in Poisson's equation while using cylindrical co-ordinates we get the following differential equation for the field distribution in the turbulent zone.

$$\frac{dE}{dr} = \frac{J_\ell}{2\pi r E b_i \varepsilon_o} + \xi E^*_{av} PS - \frac{E}{r} \qquad (4.8)$$

Similarly, substituting equations (4.6) and (4.7) in Poisson's equation yields the following differential equation for the electric field distribution in the collecting zone.

$$\frac{dE}{dr} = \frac{J_\ell}{2\pi r E b_i \varepsilon_o} + \xi E^*_{av} PS\left(1 - \frac{b_p}{b_p}\right) - \frac{E}{r} \qquad (4.9)$$

It can be seen that the above two equations differ from Pauthenier's classical differential equation which is given below as equation (4.10).

$$\frac{dE}{dr} = \frac{J_\ell}{2\pi r E b_i \varepsilon_o} + EPS - \frac{E}{r} \qquad (4.10)$$

Now the electric field in the inter-electrode gap, according to the suggested modifications, is described by equations (4.8) and (4.9) in the turbulent and collection zones respectively. These two equations cannot be solved analytically, but a numerical solution is possible using Adam's-Moulton method for numerical integration [60]. The cylindrical plane that divides the two zones was assumed to be away from the outer cylinder by a distance equivalent to 6.7% of the inter-electrode gap length. This matches the distance between the last two equipotential

contours in the charge simulation model.

For a given linear corona current J_ℓ, equations (4.8), (4.9) and (4.10) may be solved numerically for the electric field distribution. By integrating this distribution radially from the wire surface to the outer cylinder, the corresponding wire potential V_c may be evaluated.

Using the above method a computer program was constructed to give the V-I characteristics and the corresponding electrical field distributions using Pauthenier's classical equation (4.10) and the modified equations (4.8) and (4.9). The program was applied to a geometry having an inner and outer radii of 1 mm and 0.1 m respectively. The particle charge densities ρ_p investigated were: 0.44×10^{-4} and 0.44×10^{-5} C/m^3. These charge densities were evaluated using equation (4.6), according to the specified values of the following parameters: particle mean radius = 5 μm, E^*_{av} = 5 kV/cm, S = 5 m^2/m^3, P = 2, ξ = 1 and 0.1 respectively.

Figure 4.1 gives the V-I characteristics for the above described precipitator using both the classical and modified equations. It is interesting to observe that increasing the particle charge density ten times (refer to curves 1 and 2) causes a major reduction in the corona current at a given voltage.

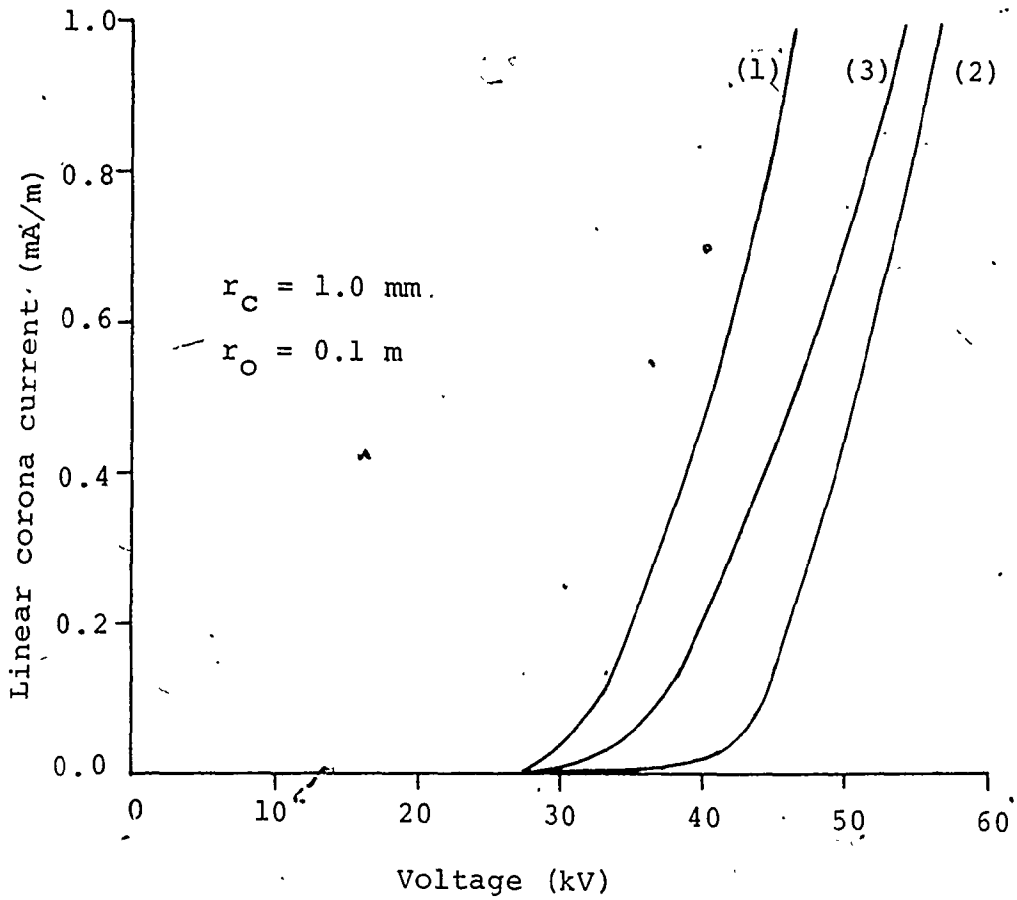

(1) $\rho_p' = 0.44 \times 10^{-5}$ C/m^3
(2) $\rho_p' = 0.44 \times 10^{-4}$ C/m^3
} results of modified solution, equations (4.8) and (4.9)

(3) Pauthenier's classical solution, equation (4.10)

Figure 4.1. V-I characteristics in a cylindrical precipitator in the presence of dust loading

Figures 4.2 and 4.3 give the electric field distributions using both the classical and the modified equations for two different operating modes: the first is constant linear corona current of 0.5 mA/m, while the second is constant voltage of 44.5 kV.

For constant linear corona current operation, it can be seen that when increasing the particle charge density ten times, the corresponding increase in potential necessary to maintain the same level of corona current is approximately 25%. Also an enhancement of 75% in the electric field at the outer cylinder was observed. The latter percentage indicates that the electric field enhancement is not only due to the increase in the applied potential but also due to the added particle space charge density.

In figure 4.2, although curves 2 and 3 are evaluated for approximately the same value of particle charge density, curve 2 which corresponds to the modified solution is significantly larger in magnitude than curve 3 which corresponds to the classical solution. This difference is more pronounced at the outer cylinder where it reaches 21%.

From figures 4.2 and 4.3, it is interesting to observe that the distribution evaluated by the classical equation (4.10) (curve 3) lies between the two curves 1 and 2 which

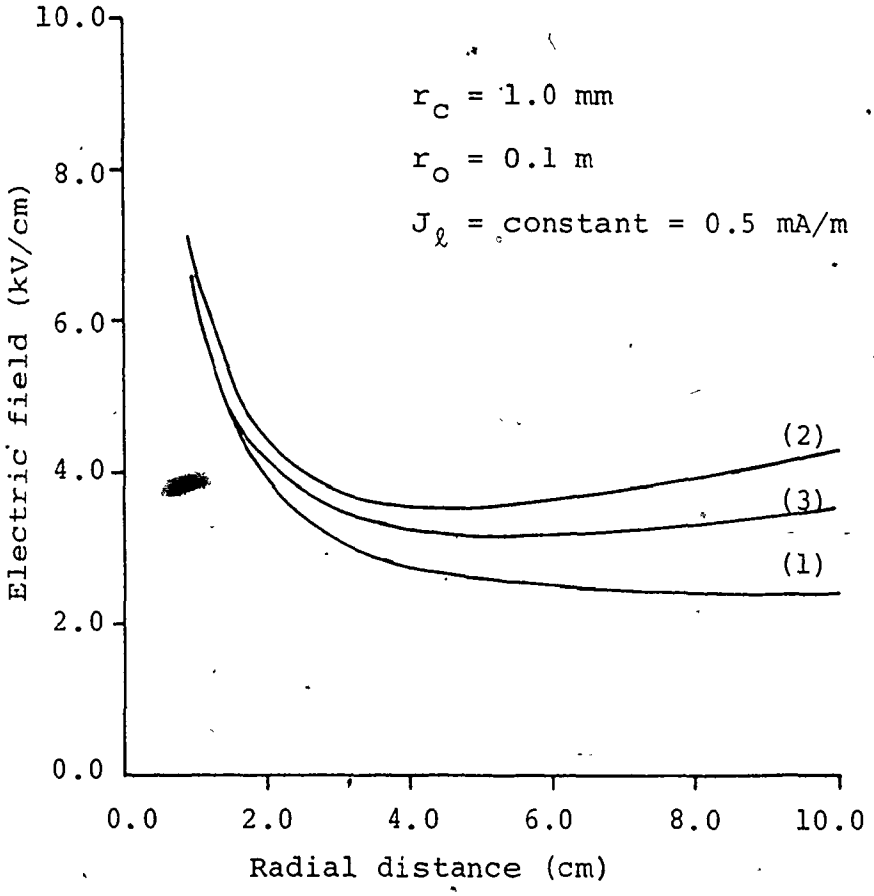

(1) $\rho_p' = 0.44 \times 10^{-5}$ C/m^3
V_c = 41.4 kV

(2) $\rho_p' = 0.44 \times 10^{-4}$ C/m^3
V_c = 50.8 kV

} results of modified solution, equations (4.8) and (4.9)

(3) Pauthenier's classical solution, equation (4.10)
V_c = 46.5 kV

Figure 4.2. Electric field distribution under conditions of dust loading and constant corona current

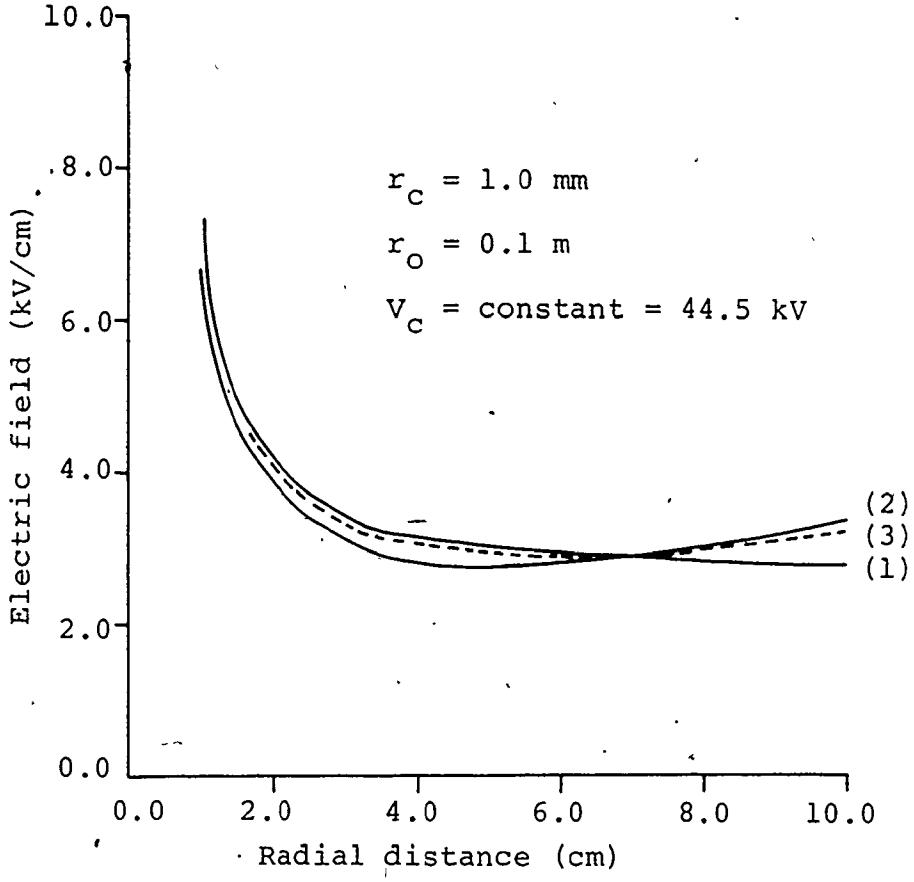

(1) $\rho_p' = 0.44 \times 10^{-5}$ C/m^3, $J_\ell = 0.8$ mA/m
(2) $\rho_p' = 0.44 \times 10^{-4}$ C/m^3, $J_\ell = 0.1$ mA/m
} results of modified solution, equations (4.8) and (4.9)

(3) Pauthenier's classical solution, equation (4.10)
$J_\ell = 0.4$ mA/m

Figure 4.3. Electric field distribution under conditions of dust loading and constant applied voltage

are evaluated by the modified solution for two different values of uniform particle charge density. This implies that although Pauthenier's assumptions are believed to be incomplete, they remain adequate for evaluating the electrical characteristics of cylindrical precipitators in the presence of dust loading.

For constant voltage operation, the increase of particle space charge density by ten times is accompanied by severe quenching of the current reaching about 90%. Also a smaller field enhancement at the outer cylinder of about 33% was observed, compared to that of the constant current case.

The previous figures indicate that the modified equations (4.8) and (4.9) as compared to the classical equation (4.10), are capable of accounting for different particle charge density levels, as a result of using the scaling factor ξ.

4.3 Corona Quenching Model

In the corona model (dust-free case) presented in chapter three, the calculation procedure involved evaluating the wire potential V_c required to maintain an assumed linear corona current density J_ℓ. The wire potential was considered to be made up of two components,

V_o and ΔV_c. The first component being the corona onset voltage V_o, and the second component ΔV_c being the voltage required to overcome the space charge due to the ion flow composing the corona current.

To include the effect of particle space charge in the clean air corona model, the potential ΔV_c was further split into two components, ΔV_i and ΔV_p. The first component ΔV_i, represents the potential required to establish the ionic space charge density ρ_i (i.e the only component present under clean gas conditions). The second component ΔV_p, represents the added potential drop due to the particle space charge ρ_p. Thus in figure (3.5), each line charge in an individual element is replaced by two line charges, one representing the ionic charge and the other representing the particle charge within the element.

The corona quenching model involves the following steps for the calculation procedure:

i) Evaluate the onset charges (including the image charges) to satisfy that the wire potential is equal to V_o and that the outer cylinder potential is equal to zero.

ii) Using the onset charges, extend 7 trajectories from the wire surface to construct the first equipotential contour as done previously in the clean air model.

iii) For each element bounded by the first contour, evaluate the magnitude of the discrete line charge q_p

representing the particle charge density using equation (4.11)

$$q_p = \rho_p' \times (\Delta r_m \Delta S_m) \qquad (4.11)$$

iv) Evaluate the ionic line charges q_i in each element of the first equipotential contour such that they satisfy equations (3.16) and (3.17).

v) To complete the calculations of the first equipotential contour, a set of image charges are evaluated such that the augmented effect of the ionic, particle and image charges is to satisfy that the potential at the outer cylinder is equal to zero (equation (3.14)).

vi) The onset charges as well as all the charges associated with the first equipotential contour are then used to extend towards the next contour. This procedure continues until the contour before last.

vii) For the elements bounded by the last two contours, the particle line charges q_p are evaluated as before using equation (4.11), while the ionic line charges q_i are evaluated such that they satisfy equations (3.16) and (4.12).

$$q_i = \rho_i' \times (\Delta r_m \Delta S_m) \qquad (4.12)$$

where ρ_i' is evaluated using equation (4.7).

The procedure was applied to a geometry having an inner and outer radii of 1 mm and 0.1 m respectively, with $\rho_p' = 0.22 \times 10^{-4}$ C/m^3. This charge density corresponds to: $S = 5$ m^2/m^3, $P = 2$, $\xi = 0.5$, $E_{av}^* = 5$ kV/cm and the mean

particle radius = 5 μm.

For a wire potential of 45 kV, equations (4.8) and (4.9) were used to evaluate the corresponding linear corona current J_ℓ. This was performed by using an iterative procedure, in which the value of J_ℓ was changed in small increments. For each value of J_ℓ the corresponding electric field distribution was evaluated and then integrated to give the wire potential V_c. If the calculated potential was different than 45 kV, J_ℓ was changed and the process was repeated again. Finally, after convergence was achieved at J_ℓ = 0.38 mA/m, the potential and ionic charge density distributions were evaluated.

The charge simulation routine developed for corona quenching, was evaluated using the above value of J_ℓ. The results of the simulation are compared to the results of equations (4.8) and (4.9). This comparison is made for the ionic charge density distribution, the potential and the electric field distributions as shown by figures 4.4, 4.5 and 4.6 respectively. It is clear from these figures that the simulation gives a reasonably good fit to the results of the modified equations (4.8) and (4.9).

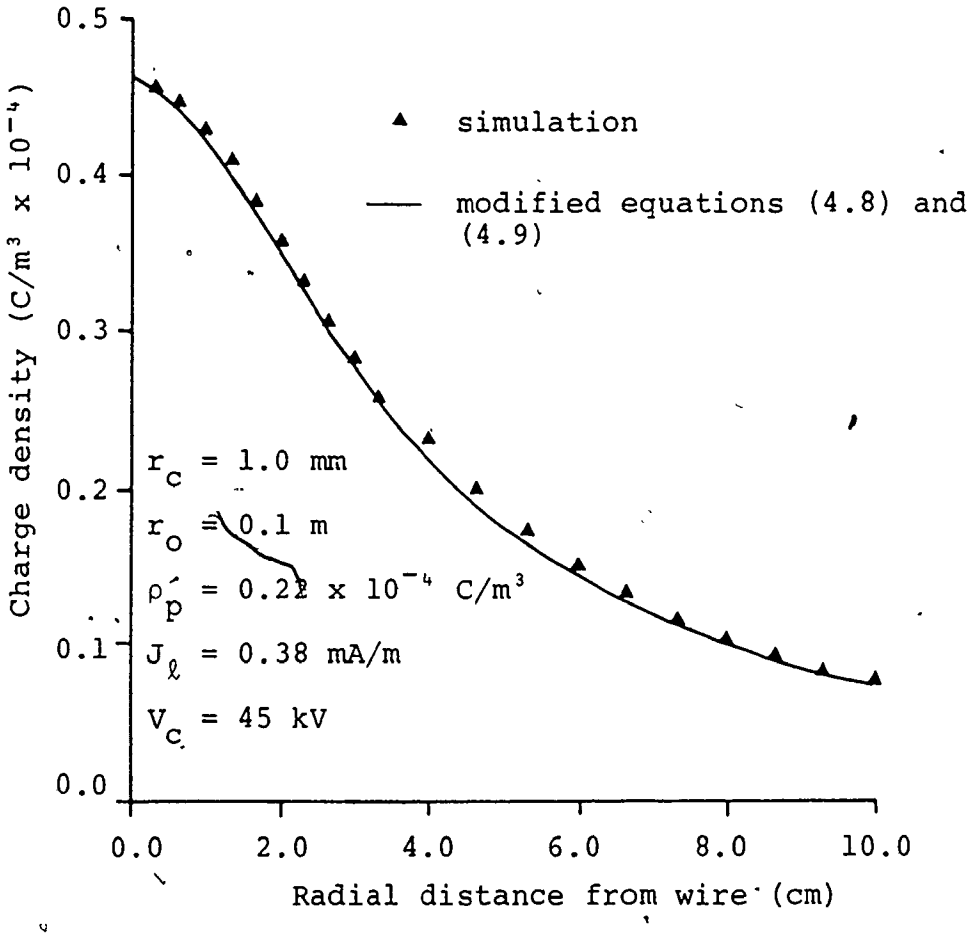

Figure 4.4. Ionic charge density distribution in a cylindrical precipitator under dust loading conditions.

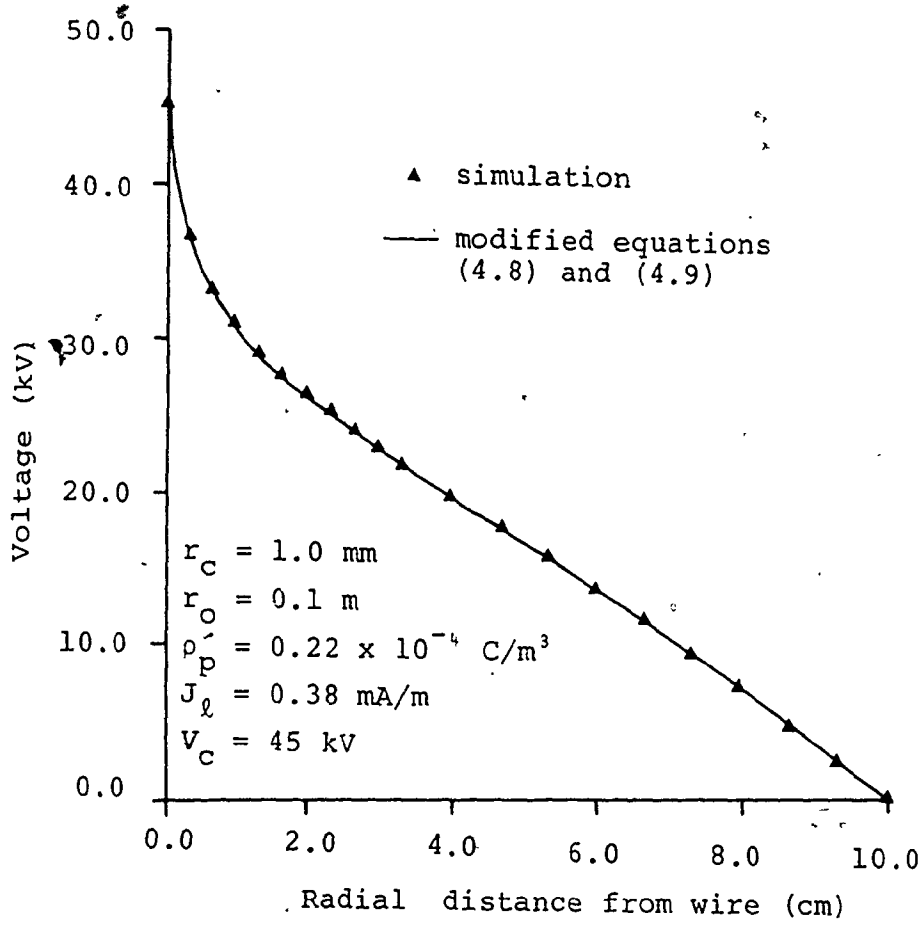

Figure 4.5. Voltage distribution in a cylindrical precipitator under dust loading conditions

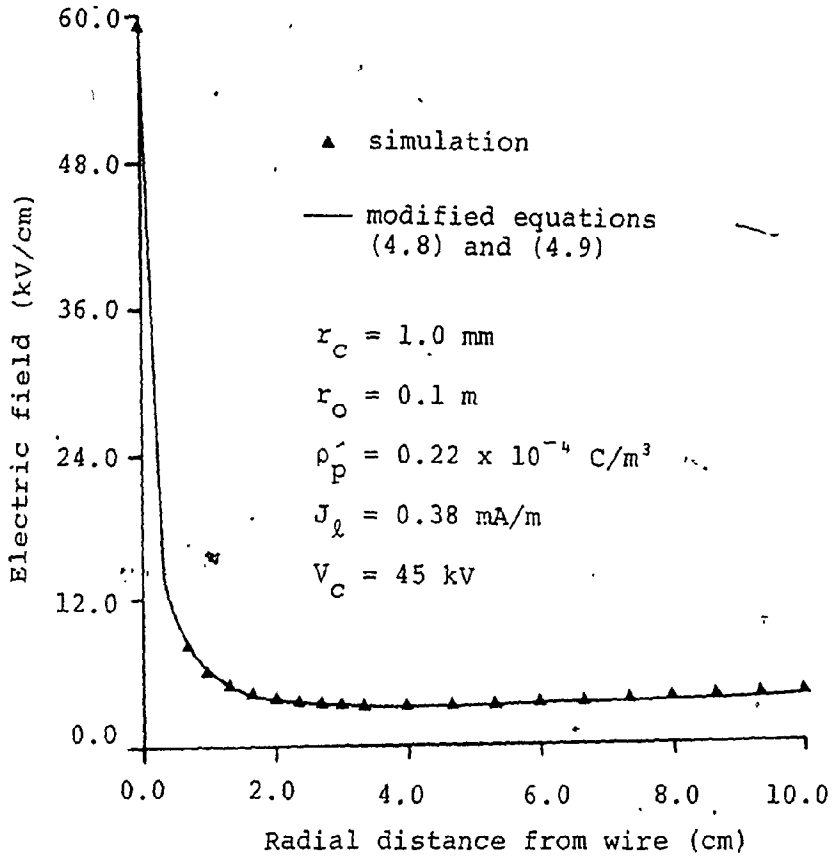

Figure 4.6. Electric field distribution in a cylindrical precipitator under dust loading conditions

CHAPTER FIVE

MODELING OF CORONA CHARACTERISTICS IN A WIRE-DUCT PRECIPITATOR USING THE CHARGE SIMULATION TECHNIQUE

5.1 Introduction

In this chapter it is intended to apply the charge simulation technique to model the electrical conditions in the more complex geometry of duct-type electrostatic precipitators.

Two models are presented. The first represents the electrostatic case in duct-type precipitators, in which the electric field is governed by Laplace's equation. The second includes the condition of corona discharge in clean air for the same geometry, in which case, the field is governed by Poisson's equation. The study involves the evaluation of the electric potential, electric field, current density and charge density in the inter-electrode space as a function of corona current.

Figure 5.1 shows the geometry of a simple duct-type electrostatic precipitator. It consists of two parallel plates and a set of corona wires positioned half way between the plates and equidistant from each other. Due to

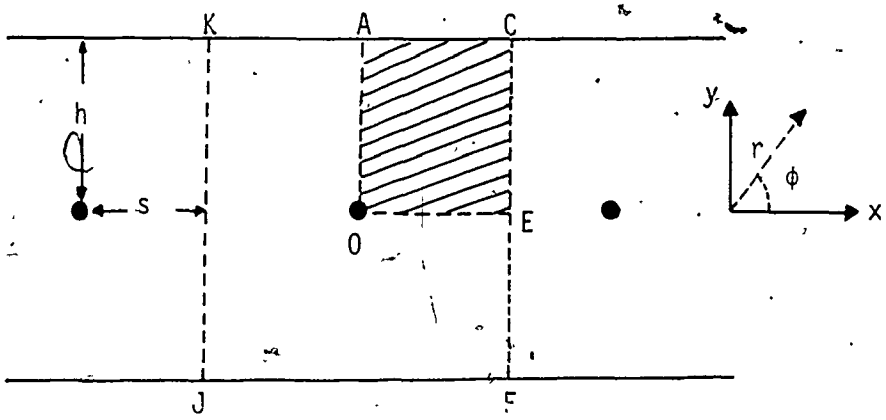

Figure 5.1. Geometry of a duct-type electrostatic precipitator

the double symmetry in the geometry, it is sufficient to study only the shaded area in Figure 5.1, for any number of corona wires, provided symmetry is preserved.

5.2 Electrostatic Model

As mentioned earlier, this geometry has no analytical solution for Laplace's equation, even when considering the problem to be two dimensional in the x-y plane.

Nevertheless Cooperman [61] was able to evaluate the voltage distribution in terms of a rapidly converging infinite series given by equation (5.1).

$$V(x,y) = V_c \sum_{m=-\infty}^{m=\infty} \frac{\ln \dfrac{\cosh(\pi(y-2ms)/2h)-\cos(\pi x/2h)}{\cosh(\pi(y-2ms)/2h)+\cos(\pi x/2h)}}{\ln \dfrac{\cosh(\pi ms/h)-\cos(\pi r_c/2h)}{\cosh(\pi ms/h)+\cos(\pi r_c/2h)}} \qquad (5.1)$$

Similarly, Böhm [62,63] evaluated the electric field distribution in the absence of space charge using the method of mirror images. The electric field components were given by equation (5.2).

$$E_x = \frac{\pi V_c}{2hf} F_x \quad , \quad E_y = \frac{\pi V_c}{2hf} F_y \qquad (5.2)$$

where (f) is a form factor dependent on the precipitator dimensions and given by (5.3) and F_x and F_y are the field shape factors in the x and y directions and are given by equations (5.4) and (5.5) respectively.

$$f = \ln \frac{4h}{\pi r_c} + \sum_{n=1}^{n} \frac{\cosh(\pi n\delta/2)+1}{\cosh(\pi n\delta/2)-1} \qquad (5.3)$$

$$F_x = \sin\frac{\pi}{2}\zeta\{ \frac{\cosh(\pi\eta/2)}{\cosh^2(\pi\eta/2)-\cos^2(\pi\zeta/2)} + \sum_{n=1}^{n} \frac{\cosh(\pi(n\delta-\eta)/2)}{\cosh^2(\pi(n\delta-\eta)/2)-\cos^2(\pi\zeta/2)} + \sum_{n=1}^{n} \frac{\cosh(\pi(n\delta+\eta)/2)}{\cosh^2(\pi(n\delta+\eta)/2)-\cos^2(\pi\zeta/2)}\} \qquad (5.4)$$

$$F_y = \cos\frac{\pi}{2}\zeta\{ \frac{\sinh(\pi\eta/2)}{\cosh^2(\pi\eta/2)-\cos^2(\pi\zeta/2)} - \sum_{n=1}^{n} \frac{\sinh(\pi(n\delta-\eta)/2)}{\cosh^2(\pi(n\delta-\eta)/2)-\cos^2(\pi\zeta/2)} + \sum_{n=1}^{n} \frac{\sinh(\pi(n\delta+\eta)/2)}{\cosh^2(\pi(n\delta+\eta)/2)-\cos^2(\pi\zeta/2)}\} \qquad (5.5)$$

where $\eta = x/h$, $\zeta = y/h$

$\delta = s/h$, n = No. of corona wires

Thus the validity and the accuracy of the electrostatic model presented here may be compared to the solutions presented in equations (5.1) and (5.2).

The concept of the charge simulation technique was directly applied to this model by replacing all the conductor surface charges by discrete infinite line charges of the form shown in figure 5.2. To model the precipitator sections on the left and the right of the central corona

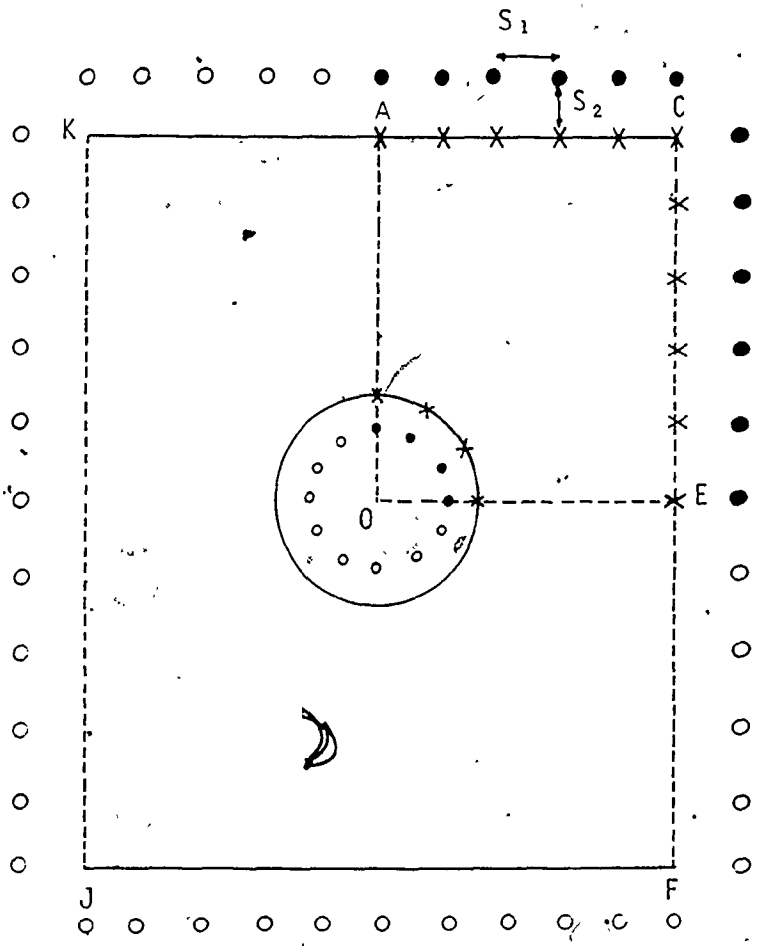

onset charges

onset image charges

X boundary points

Figure 5.2. Location of line charges and boundary points for modeling the electrostatic case

wire, line charges were placed adjacent to the lines (C-F) and (K-J) and the necessary field boundary conditions were satisfied along those two lines. The potential (and field) coefficient matrix was then constructed using the appropriate equations for line charges (refer to section 2.3). The Gaussian elimination method was used for solving the matrix equation (5.6) for the unknown charges, such that their values satisfied certain pre-determined boundary conditions.

$$[PC]_{nxn} [Q]_n = [V]_n \qquad (5.6)$$

where [PC]=potential (and field) coefficient matrix, [Q]=magnitudes of unknown charges, and [V]=potential (and field) values at boundary points.

Considering only the first quadrant, with reference to figure 5.2, which is only a schematic diagram and does not represent the actual number of infinite line charges used in the model, 8 charges were placed inside the circular corona wire and another 31 image charges were placed behind the collecting plate (A-C). Finally, another set of 31 image charges were placed behind the line (E-C) to model the adjacent sections of the precipitator. The image charges were located relative to the boundary points as shown in figure 5.2 such that the ratio S_1 to S_2 was approximately unity.

As in the cylindrical case, it is sufficient to store the positions and values of the charges located in the first quadrant only. Nevertheless, when evaluating the elements of the potential coefficient matrix, all charges in the four quadrants must be considered.

The boundary conditions to be satisfied by the infinite line charges are as follows:

i) $V = V_c$ at all points on the wire surface.

ii) $V = 0$ at all points on the collecting plate.

iii) $E_x = 0$ along the line (E-C).

The above model was programmed and evaluated for a laboratory scale duct-type precipitator as used by Awad [64] having the following dimensions: $h = 3.8$ cm, $s = 3.8$ cm and $r_c = 0.825$ mm. The wire potential was 5 kV.

The results were compared to both Cooperman's and Böhm's infinite series for the voltage and field distributions respectively. The model gave very good agreement to both series as can be seen from figures 5.3, 5.4 and 5.5.

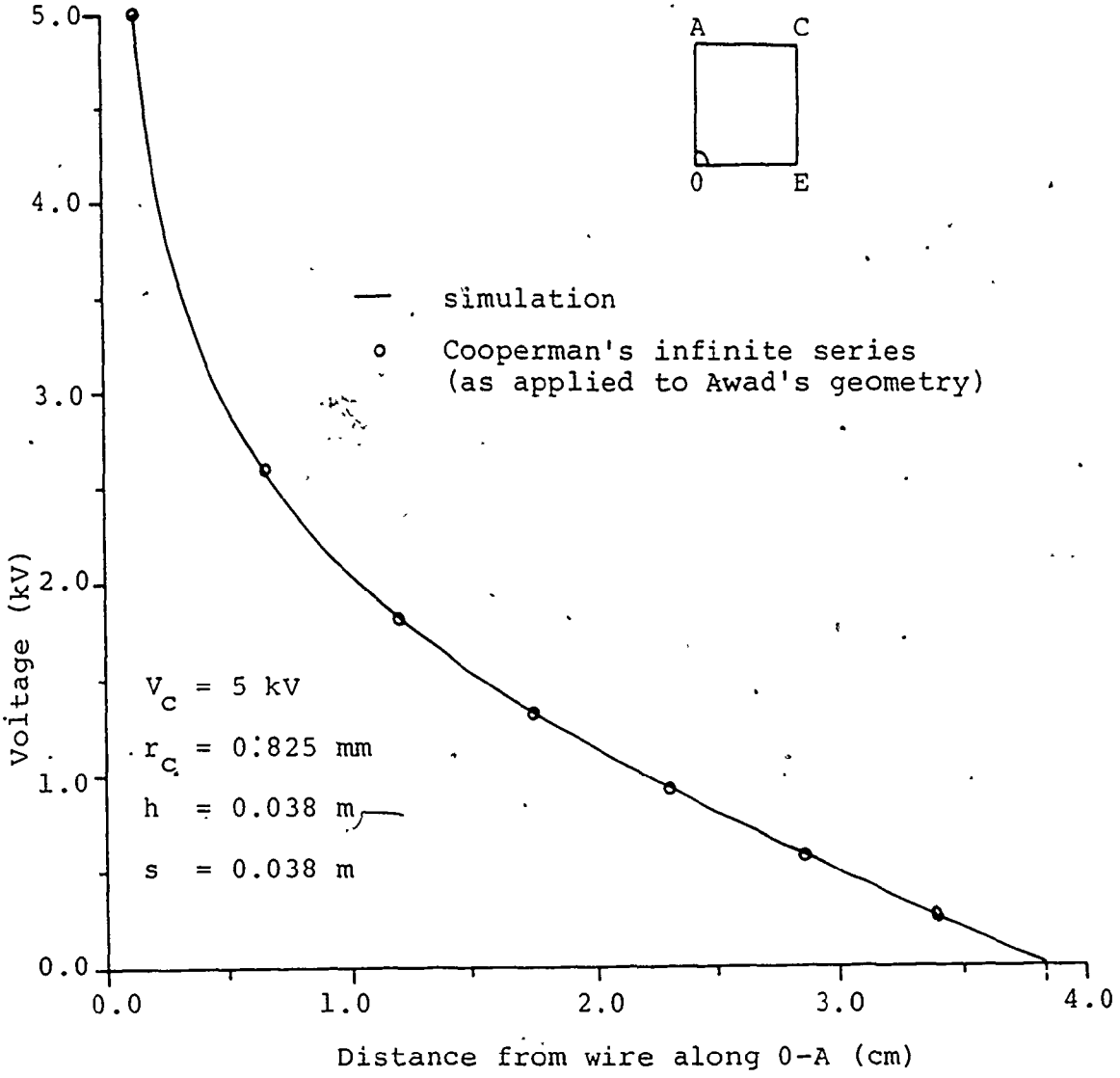

Figure 5.3. Voltage distribution along 0-A for the electrostatic case.

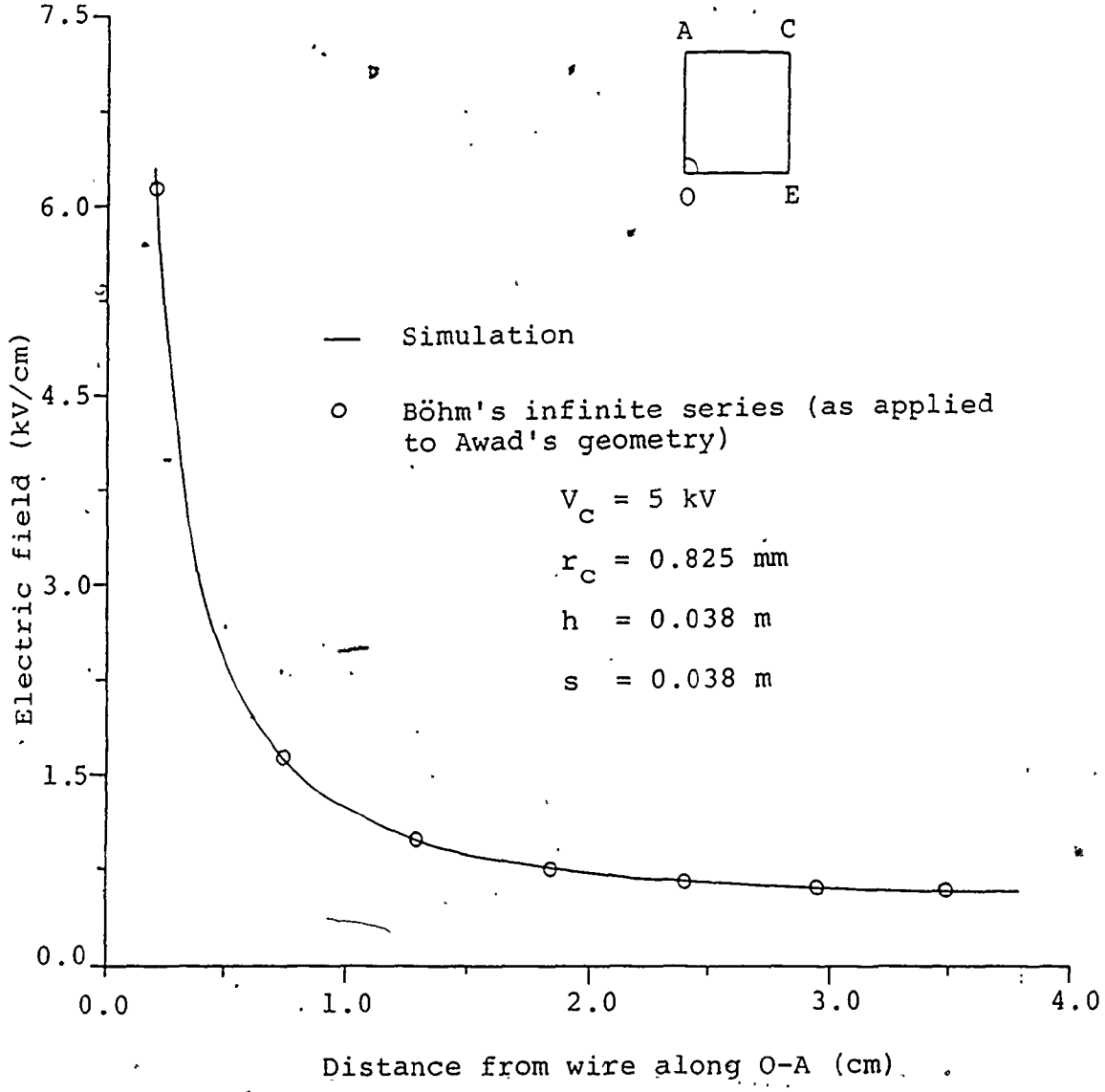

Figure 5.4. Field distribution along O-A for the electrostatic case

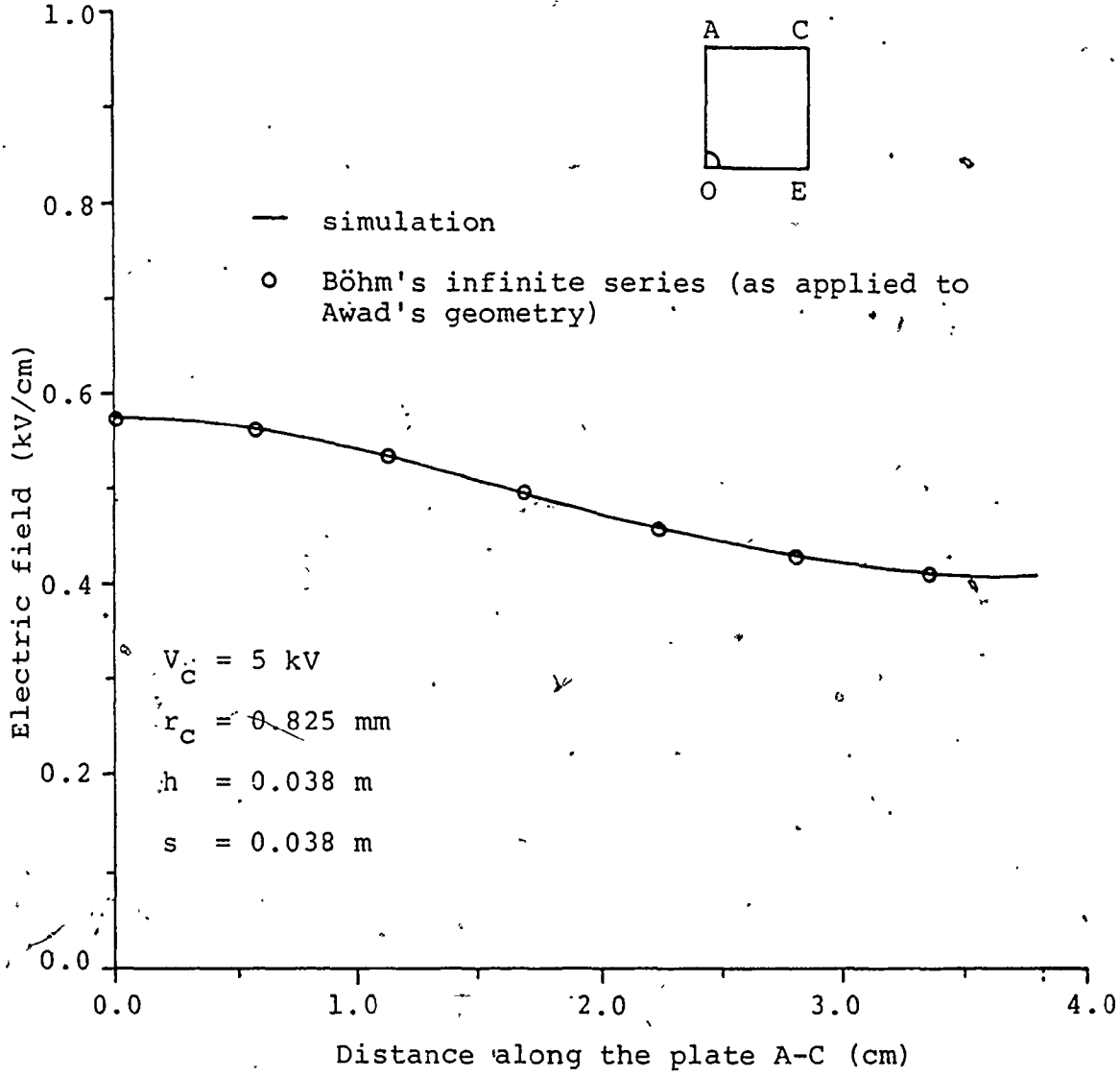

Figure 5.5. Field distribution along the collecting plate in the electrostatic case

5.3 Corona Model

Similar to the cylindrical case, to avoid complications associated with the ill-defined glow region in both positive and negative coronas, the wire is assumed to be a uniform ion emitting source.

This assumption is based on neglecting the ionization zone as well as the fact that for small diameter wires, the electric field is approximately uniform around the wire surface. This was confirmed by the electrostatic model presented here, since the electric field was found to be uniform within less than 0.1 percent around the wire.

In the presence of space charge and under steady-state conditions, the region of interest is governed by Poisson's equation and the current continuity equation. Unlike the cylindrical geometry the two equations here have no analytical solutions.

If one imagines a ray or a tube formed by two lines of field, the amount of current flowing through any cross section of this tube is constant. Thus for a set of field lines emanating from a corona wire and intercepted by an equipotential contour such as in figure 3.5, the current continuity equation has to be satisfied at each segment of the contour.

It was not necessary to account for this physical condition in the cylindrical model since the trajectories of the lines of field were identical (ie. radial) both with and without space charge. Also the equipotential contours were always circular in shape and thus segments of the same contour were equal in length. Moreover, the ionic charge density was only a function of the radial distance (r) and not also the angle (ϕ), thus segments of adjacent contours bounded an equal value of charge density.

When attempting to apply this charge simulation model to the duct-type geometry discrepancies were observed. For example, the trajectories of the lines of field were irregular and did not terminate at the plate. The magnitude and even the polarity of the ionic charges and their images did not match the actual physical characteristics of corona in a duct-type electrostatic precipitator. Furthermore, the potential contours did not remain equipotential as calculations progressed.

Thus modifications were necessary for the duct geometry to overcome the problems that were hidden in the cylindrical geometry due to its rotational symmetry.

The same basic concept of dividing the wire potential V_c into two components V_o and ΔV_c was used. The first component being the corona onset voltage V_o and the second

component ΔV_c, being the voltage required to establish a space charge equivalent to the pre-determined corona current I_c. Thus, similar to the previous approach [65], the infinite line charges used in the model were divided into two groups and superposition was used to arrive at the overall solution.

The first group, which will be referred to as the onset charges (and includes the onset image charges), was placed outside the region where the solution was sought, as was done in the electrostatic case. The wire potential was made equal to the onset voltage V_o. This was achieved by initially assuming an arbitrary wire potential V_o^*. Then, after solving equation (5.6) for the unknown onset charges, the electric field $E_y(0,r_c)$ was evaluated and compared to the onset field E_o from Peek's formula [13]. Later, the onset charges were rescaled by multiplying them by the ratio $(E_o/E_y(0,r_c))$.

The second group was placed inside the region where the solution was sought as shown by figure 5.6. This figure is not to scale and does not include the actual number of charges implemented in the model. These charges represent the ionic space charge and their magnitudes were evaluated such that they contributed a potential ΔV_c to the corona wire and zero potential to the collecting plate while maintaining $E_x = 0$ along the center line between the

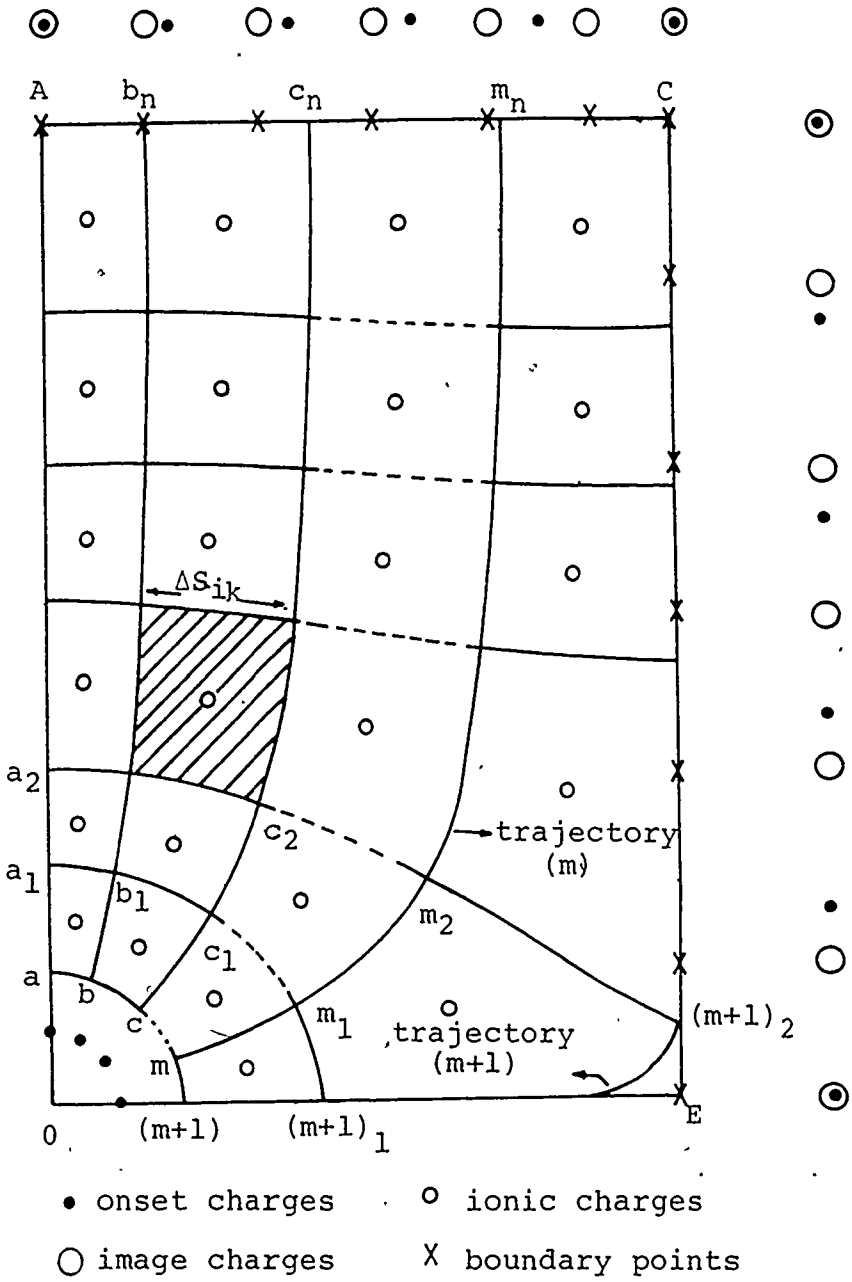

Figure 5.6. Location of line charges and boundary points for modeling the corona case

corona wires (E-C).

The augmented effect of both sets of charges must satisfy the boundary conditions given by equations (5.7), (5.8), (5.9) and (5.10) as well as the current continuity equation (5.11).

$$V(\phi, r_c) = V_c \tag{5.7}$$

$$E(\phi, r_c) \doteq E(\phi, r_c) \tag{5.8}$$

$$V = 0 \quad \text{at plate surface} \tag{5.9}$$

$$E_x = 0 \quad \text{along (E-C)} \tag{5.10}$$

$$I_c = \oint J.dA \tag{5.11}$$

As mentioned earlier, the wire was modeled as a simple ion emitter, thus the commonly used assumption [41] that the ionic charge density is uniformly distributed at the wire surface was considered reasonable.

To evaluate and locate the ionic charges (i.e the second group of line charges) a method similar to the one presented in the cylindrical case was used with some additional modifications. The method was based on finding a set of (n) equipotential contours by extending (m+1) trajectories or field lines (refer to figure 5.6) from the wire surface to the collecting plate.

The major modification was the use of two different processes for evaluating the ionic charges and their associated image charges that are necessary for maintaining the boundary conditions (5.9) and (5.10)

The first process is only applicable to the ionic charges within the first equipotential contour and their images. This process may be summarized in the following steps with reference to figure 5.7.a:

1) Select a set of (m+1) points on the wire surface (e.g. a, b, c ..... (m+1)). Extend trajectories [47] from these points to the corresponding equipotential points (a_1, b_1, c_1 ..... $(m+1)_1$) using only the onset charges.

2) Since all elements of the first equipotential contour are assumed to have the same charge density (ρ_1), then the uniform charge density may be evaluated using equation (5.12). The ionic charges of the first contour are positioned at the average center* of each element and are evaluated using equation (5.13). The numerator in equation (5.12) represents the corona current per meter length of the wire in one quadrant.

$$\rho_1 = \frac{I_c/4L}{\sum_{i=1}^{m} E_{1i} \cdot b \cdot \Delta S_{1i}} \qquad (5.12)$$

*corresponds to the mean of the 4 co-ordinates describing the elemental area

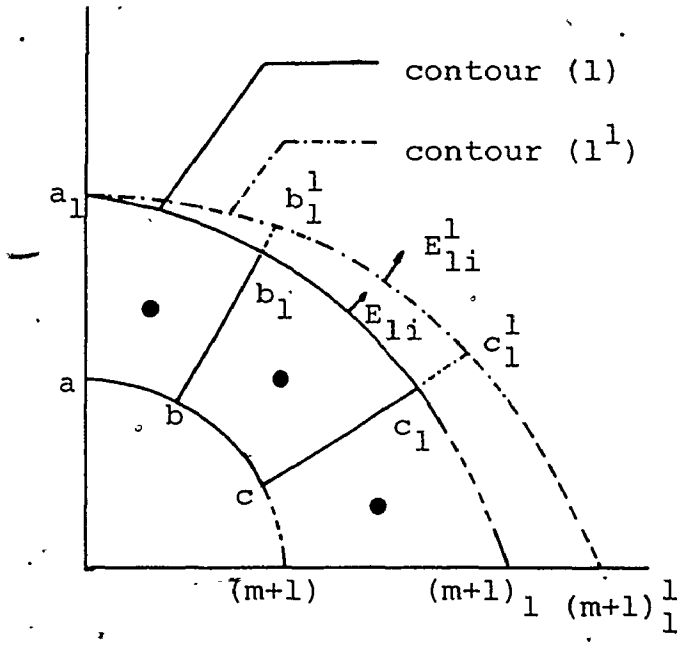

(a) Method of stepping to first contour

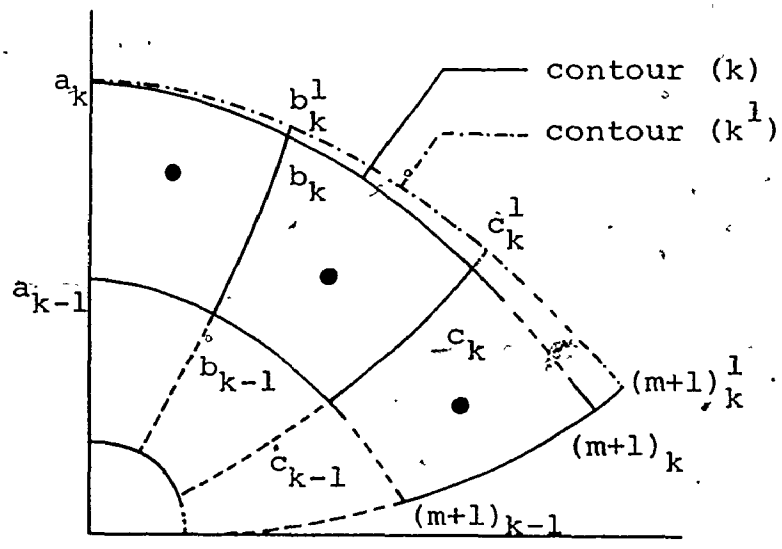

(b) method of stepping to successive contours

Figure 5.7. Iterative procedures for locating the equipotential contours

$$q_{1i} = \rho_1 \cdot A_{1i} \qquad (5.13)$$

3) Due to the presence of the ionic charges, the boundary conditions along (A-C) and (E-C) are distorted. Thus a set of image charges are placed behind the collecting plate (A-C) and behind the center line between the corona wires (E-C). Their purpose is to satisfy equations (5.9) and (5.10) by counter-acting the effect of the ionic charges at these two boundaries.

4) Contour (1) represented by $(a_1, b_1 \ldots\ldots (m+1)_1)$ was equipotential with respect to the onset charges only. Therefore the modified equipotential contour (1^1) represented by $(a_1^1, b_1^1, \ldots\ldots (m+1)_1^1)$ is located taking into consideration the ionic charges and their images.

5) The new element dimensions (A_{1i}^1) and the modified fields E_{1i}^1 (for i=1,m) are re-evaluated, together with the modified charge density (ρ_1^1), the modified ionic charges (q_{1i}^1) and their associated modified images.

6) Steps (4) to (6) are repeated until the percentage difference between ρ_1^n and ρ_1^{n-1} is less than 1 percent.

Finally, the amount of current I_i flowing between each two successive trajectories is evaluated using equation (5.14).

$$I_i = \frac{q_{li}^n}{A_{li}^n} \cdot b \cdot E_{li}^n \cdot \Delta S_{li}^n \quad \text{for } i=1,m \qquad (5.14)$$

where $$I_c = 4L \cdot \sum_{i=1}^{m} I_i \qquad (5.15)$$

The second process which is used for all the remaining contours, is similar to the first (refer to Figure 5.7.b), except for the following differences:

a) Each element at the kth contour has its own independent value of charge density (ρ_{ki}) and subsequently charge (q_{ki}). These are evaluated using equations (5.16) and (5.17) respectively.

$$\rho_{ki} = \frac{I_i}{E_{ki} \cdot b \cdot \Delta S_{ki}} \qquad (5.16)$$

$$q_{ki} = \rho_{ki} \cdot A_{ki} \qquad (5.17)$$

b). The criterion for convergence at the kth contour is that the percentage difference between (q_{ki}^n) and (q_{ki}^{n-1}) be less than 1 percent.

At the end of the calculations, the integrated trajectories should terminate at the grounded plate. This is one method of checking the validity of the model.

In the corona model, the number of onset charges (including the onset image charges) was 40. Those were positioned exactly as prescribed in the electrostatic case,

except that the number of onset image charges were reduced to 16 behind the two lines (A-C and E-C). The number of trajectories used was eleven (m+1=11), making the number of discrete ionic charges per contour equal to ten (m=10). The number of image charges per contour was 40. Twenty of those were positioned behind the collecting plate (A-C) and the remaining 20 were positioned behind the line (E-C). The contour space was graded according to distance from the wire as measured along O-A as shown in Table 5.1 below.

Set No.	No. of Contours	Percent increment of (h-r)
1	5	0.1
2	5	0.5
3	17	1.0
4	5	2.0
5	5	4.0
6	10	5.0

Table 5.1 Contour spacing along O-A starting from the wire surface.

5.3.1 Results of Corona Model

The developed program was applied to a duct-type precipitator whose dimensions and operating conditions were identical to that used by Penney and Matick [31]. Figure 5.8 illustrates the equipotential contours and the lines of field which together constitute the elemental grid produced by the simulation. The precipitator dimensions as well as the operating conditions are included in the figure.

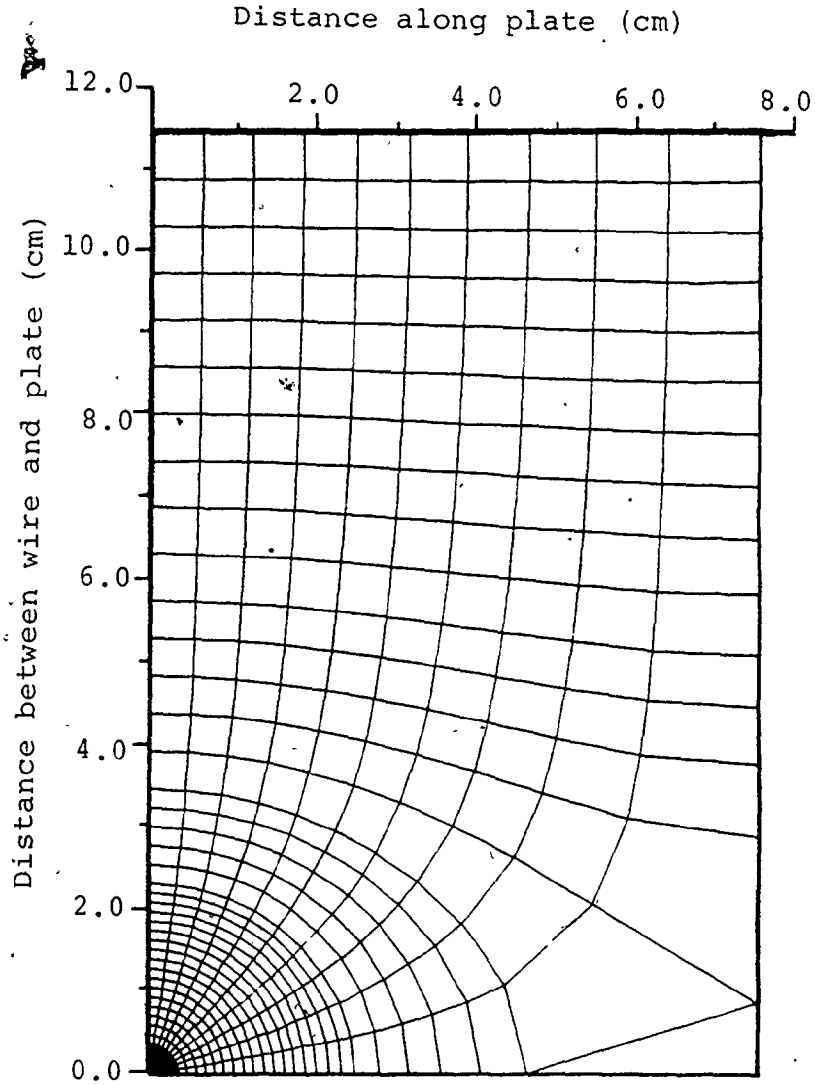

r_c = 0.15 mm

h = 0.11 m

s = 0.076 m

J_ℓ = 0.48 mA/m

V_c = 44 kV

V_o = 11.4 kV

Figure 5.8. Equipotential contours and lines of field constituting the grid

To check the validity of the model, the potential at different points along the collecting plate was evaluated and compared with the expected value of zero. It was found to vary from +3.1 to -1.1 volts (or less than 0.01 percent with respect to V_c). Also the ratio of the tangential to the perpendicular field components (E_x/E_y) at different points along the plate were calculated and found to vary from +0.36 percent to -0.42 percent. Similar evaluations of the ratio (E_x/E_y) were performed along the center line between the corona wires (E-C), these yielded a range from +5.5 percent (at the two ends) to -1.2 percent.

Several researchers [56,66] have used the assumption that the lines of field remain unchanged in direction whether space charge exists or not for a defined set of precipitator dimensions. In figure 5.9 the dashed lines and the solid lines represent the equipotential contours and the lines of field for the electrostatic and corona cases respectively. It is evident from this figure that the lines of field do not coincide for the two cases. Nevertheless, this assumption is valid for the cylindrical geometry, since the lines of field are always radial whether space charge exists or not.

The charge density distribution along a line extending from the wire to the plate is shown in figure 5.10. This figure indicates the necessity of having a finer grid size

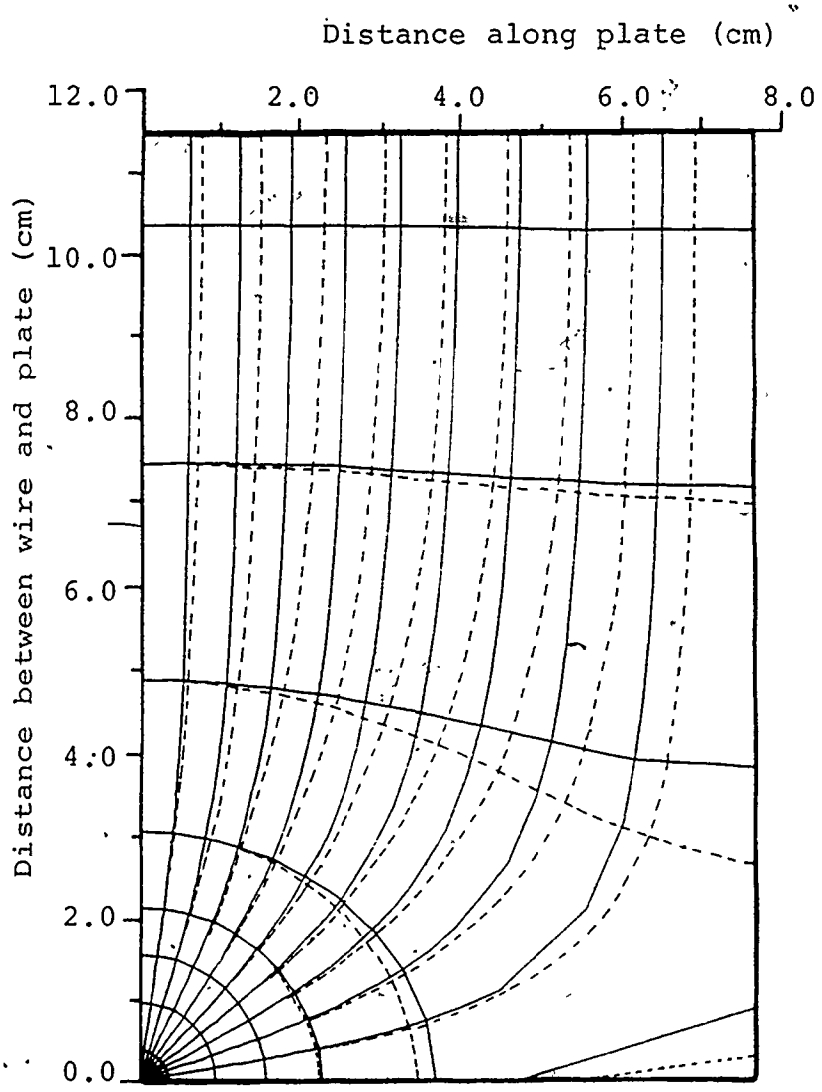

r_c = 0.15 mm

h = 0.11 m

s = 0.076 m

--- Electrostatic case ($V_c = V_o = 11.4$ kV, $J_\ell = 0$)

——. Corona case ($V_c = 44$ kV, $J_\ell = 0.48$ mA/m)

Figure 5.9. Equipotential contours and lines of field for the electrostatic and corona models

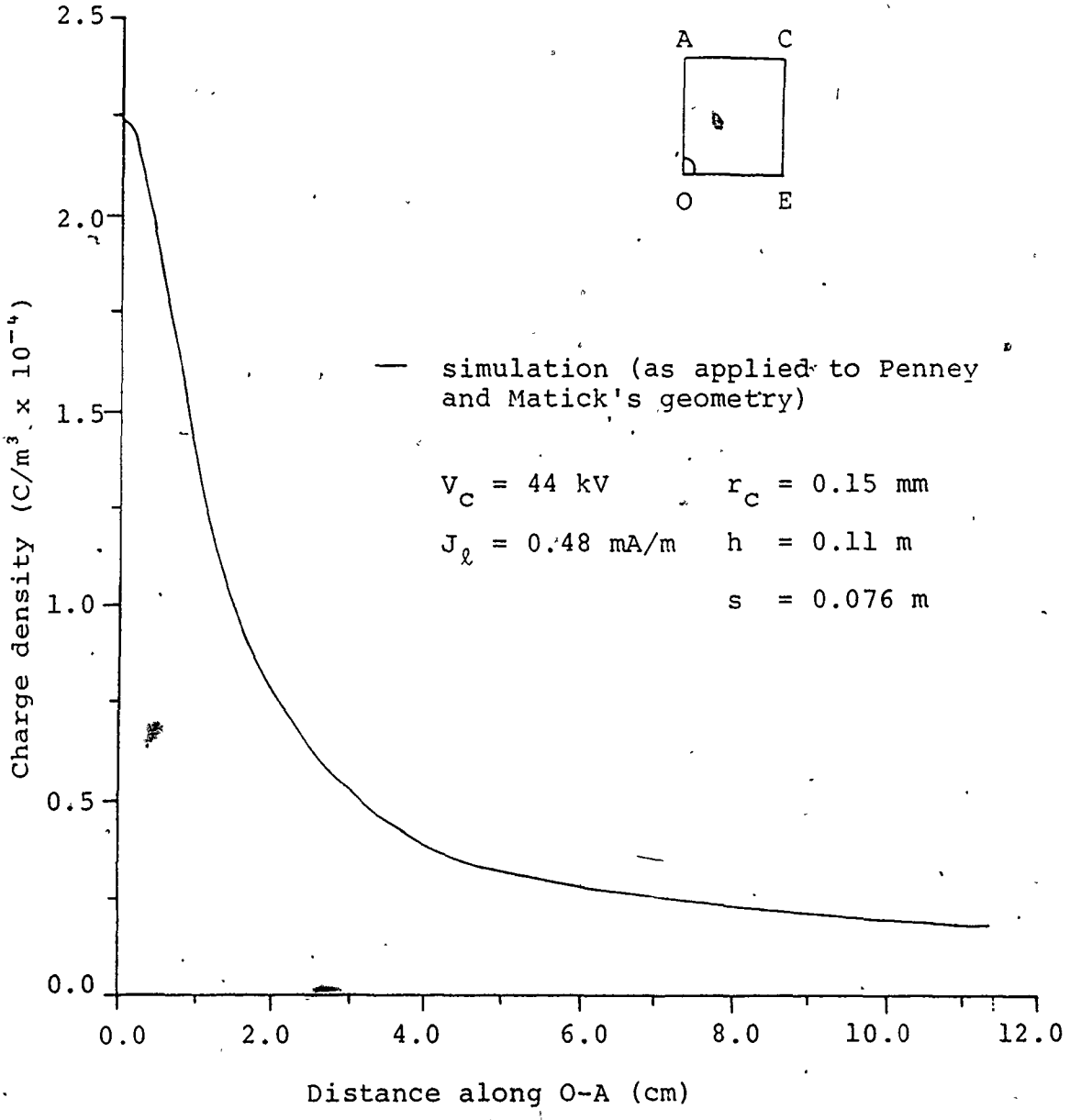

Figure. 5.10. The charge density distribution along O-A

close to the wire, as opposed to a coarser size next to the collecting plate, to accurately simulate the exponential decaying function of the charge density.

The results of the model were compared to Penney and Matick's experimental results. This was done by evaluating the voltage distribution using the simulation routine along (O-A) and (E-C). The results are plotted in figures 5.11 and 5.12 respectively. The upper curves in both figures were the result of using a mobility value of 1.8×10^{-4} $m^2/V.s$. This value of mobility gave a wire voltage V_c = 44 kV as opposed to the experimental value of 43.5 kV required to maintain the pre-determined (input) corona current J_ℓ = 0.48 mA/m. While the lower curves in both figures were the result of using a mobility value of 2.2×10^{-4} $m^2/V.s$. This gave a wire voltage of 40.5 kV.

From both figures, it is evident that the choice of mobility value plays an important role in the accuracy of the simulation model. This is as it should be, since it is well known that the V-I characteristic for a corona discharge is very dependent upon the effective mobility of the charge carriers.

It was also found that the field at point (A) (refer to figure 5.1) changed from 0.33 at $V_c = V_o$ = 11.4 kV to 4.7 kV/cm at V_c = 44 kV. Similarly, the field at point (C)

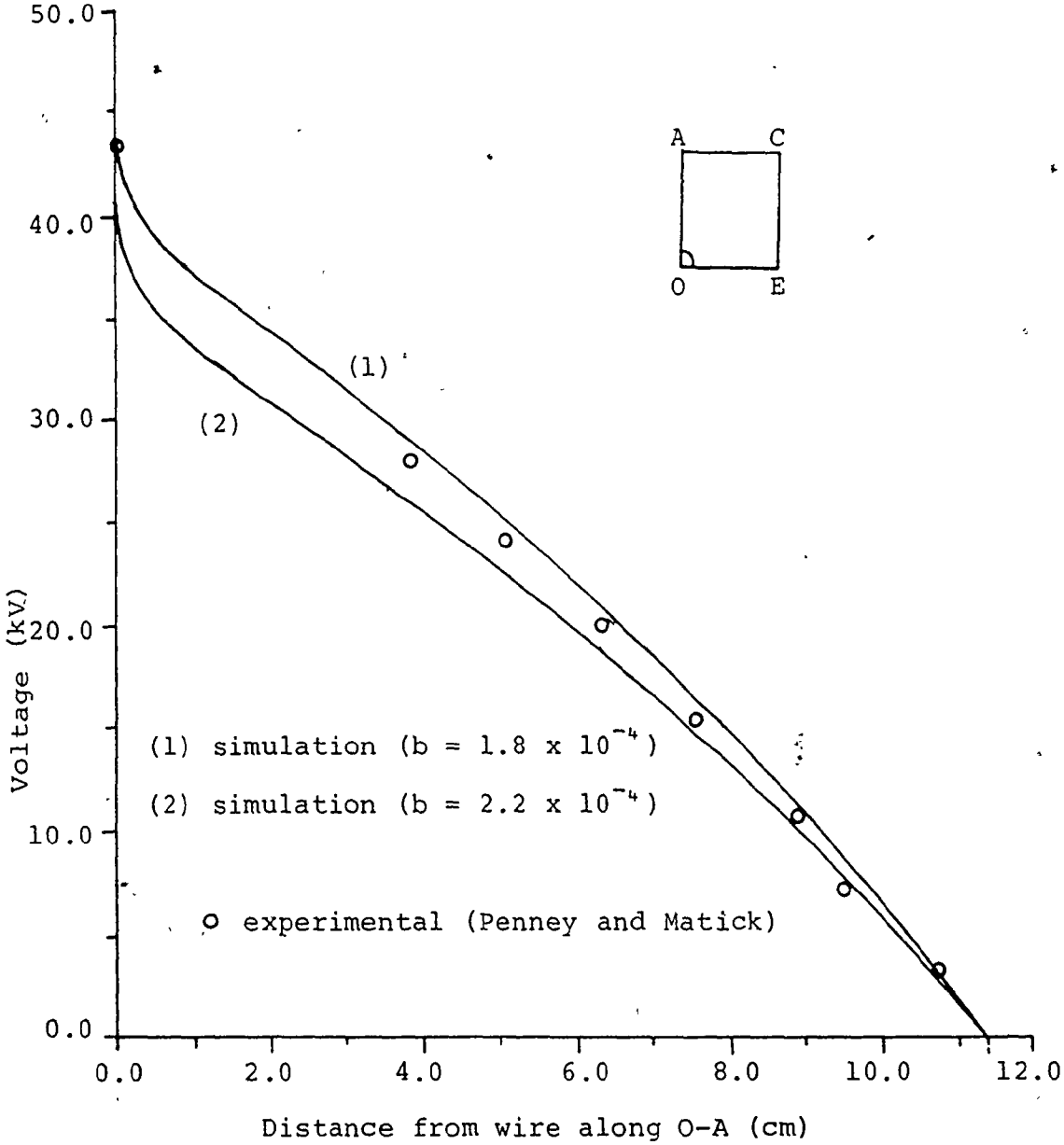

r_c = 0.15 mm h = 0.11 m

J_ℓ = 0.48 mA/m s = 0.076 m

Figure 5.11. Voltage distribution along O-A for two different values of ion mobility

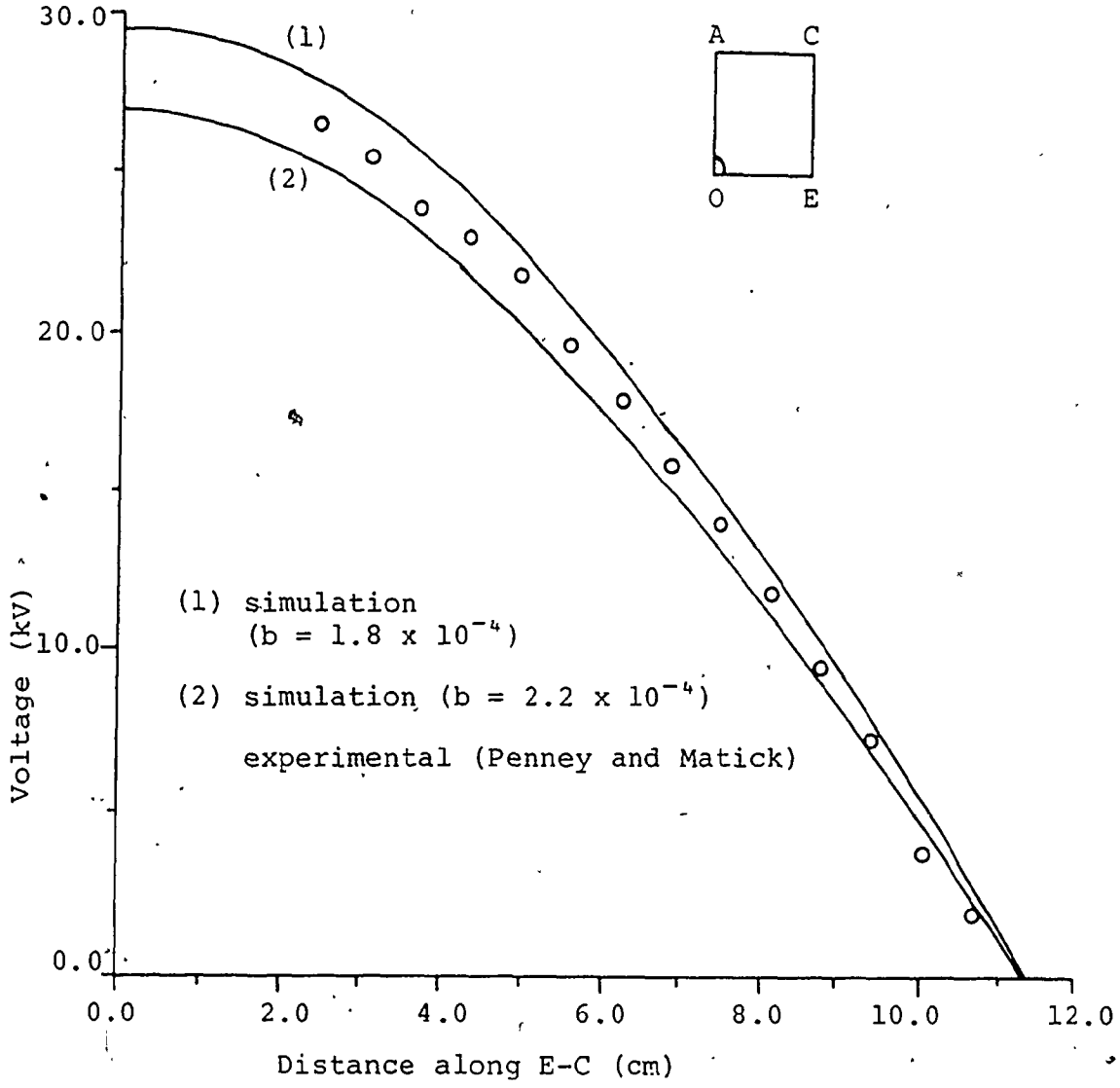

r_c = 0.15 mm h = 0.11 m

J_ℓ = 0.48 mA/m s = 0.076 m

Figure 5.12. Voltage distribution along E-C for two different values of ion mobility

changed from 0.3 to 4.3 kV/cm for the same voltages respectively. Thus increasing the wire potential 3.9 times resulted in the increase of the electric field by approximately 14.3 times at points (A) and (C). This large increase in the electric field value, from the electrostatic case to the corona case, exhibits the significant contribution of space charge in enhancing the field at the collecting walls.

The model was also applied to a precipitator whose dimensions and operating conditions were similar to those of Felici's [30], h = 0.1 m, s = 0.1 m and r_c = 0.127 mm. The corona current input was 0.6 mA/m. It is important to mention here that the current density distribution graphs presented by Felici [30] are apparently missing a multiplying scale factor of two. When evaluating the area under each of these graphs, the resultant current J_ℓ was found to be equal to one half the documented (measured) value.

The current density distribution at the collecting plate was evaluated by equation (5.18), which gives the average current density (J_i) for each element at locations half way between the points (a_n, b_n, c_n ..... $(m+1)_n$).

$$J_i = I_i / \Delta S_{ni} \qquad (5.18)$$

The current density distribution at the plate for Felici's geometry using the simulation is shown in figure 5.13. It can be seen from the figure, that the simulation curve follows a similar pattern to the experimental data, but its magnitude is slightly higher. The percentage difference between the simulation and the experimental data is approximately 17 percent close to point (A) directly below the corona wire.

This difference could be the result of the mobility value assumed here (2.2×10^{-4} $m^2/V.s$) and the result of experimental error in the measurement of the linear corona current J_ℓ which is used as an input parameter to the model. The actual cause of this difference was hard to determine because the experimental applied voltage V_c was not documented.

Another method of checking the model was to normalize both the simulation and the experimental results of figure 5.13. The simulation results were normalized with respect to the value of current density at x = 0, obtained by extrapolating the simulation curve to intercept the ordinate.

The normalized results are shown in figure 5.14. This figure shows that the simulation results tend to diverge from the experimental data as we move towards the center

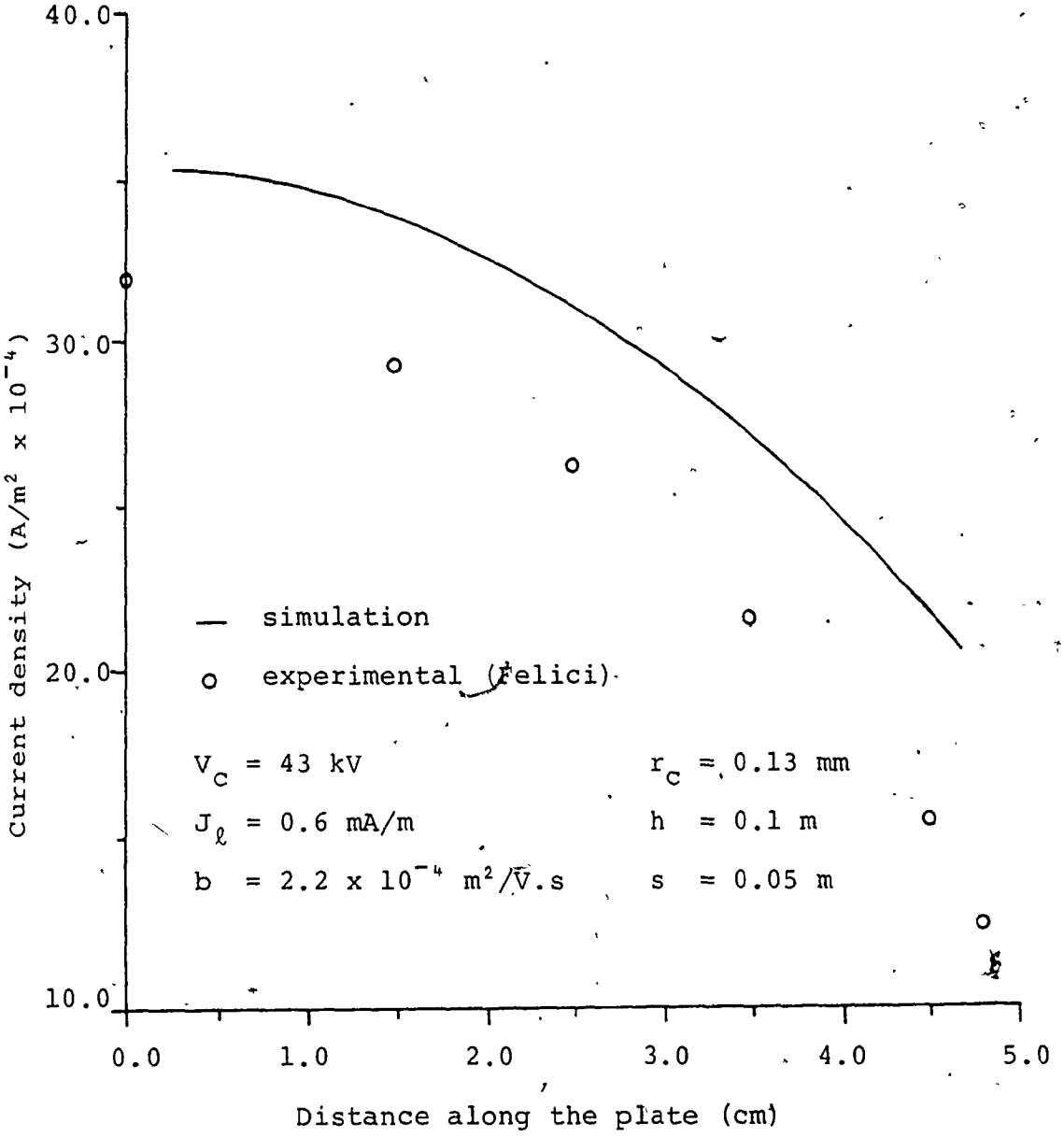

Figure 5.13. The current density distribution along the collecting plate

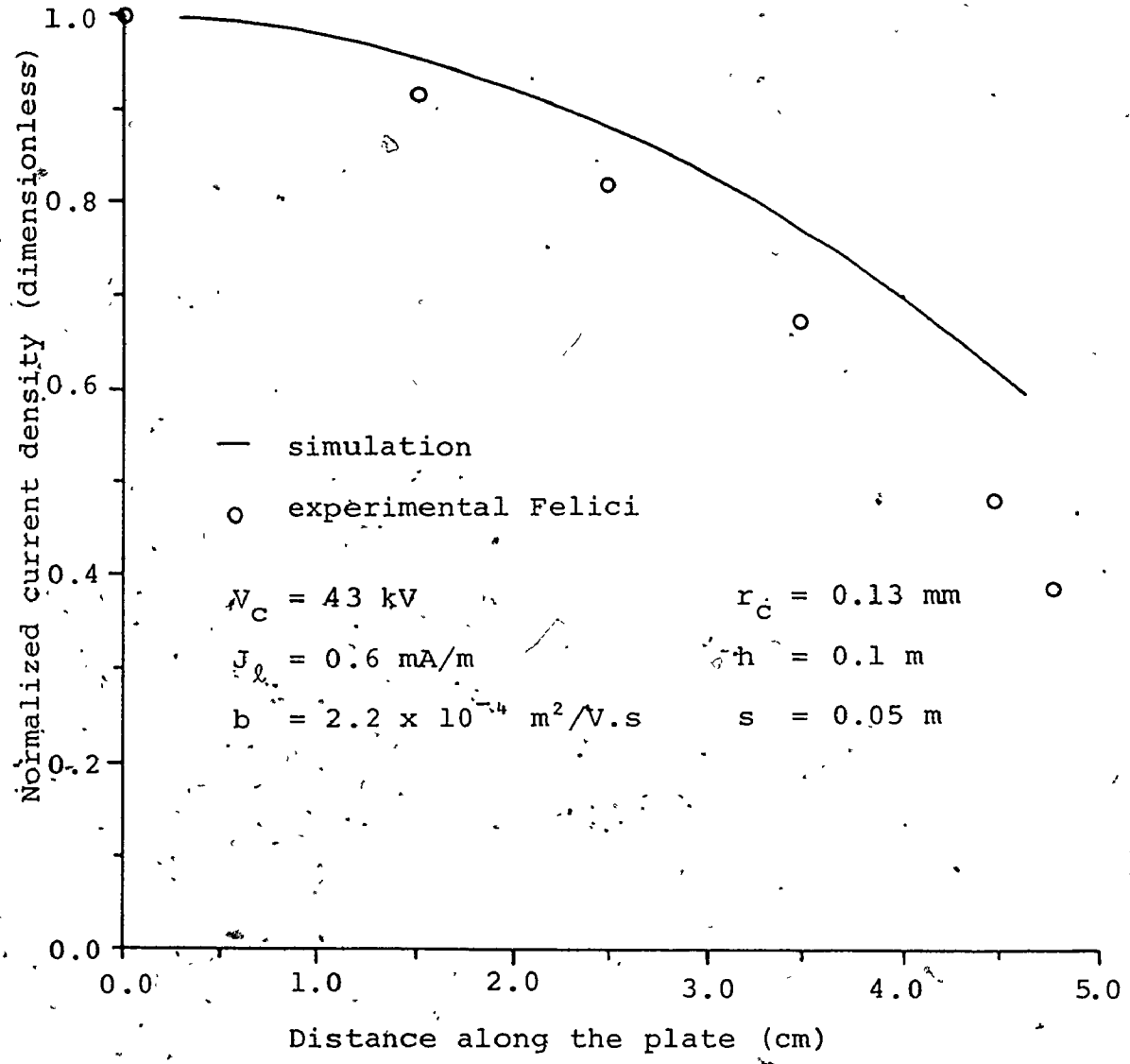

Figure 5.14. The normalized current density distribution along the collecting plate

line (E-C). This was also found to be the case when applying the model to another set of dimensions and operating conditions also given by Felici. The changes from the previous set of dimensions and operating conditions were, s = 0.2 m and J_ℓ = 0.1 mA/m. Figure 5.15 shows the normalized distribution compared to the experimental data for Felici's second geometry.

The deviation of the simulation results from the experimental data is believed to be the result of evaluating the current density as an average value (J_i, using equation (5.18)). This deviation is more significant at the outer elements (close to point E), since those elements are larger in size with respect to those closer to point (A). This is also coupled with the fact that the current density changes more rapidly along the plate adjacent to point (E).

If the number of elements per contour was to be increased, by increasing the number of trajectories, then it could be expected that the simulation results should give better convergence to the experimental data. On the other hand, in doing so the computational time would increase substantially.

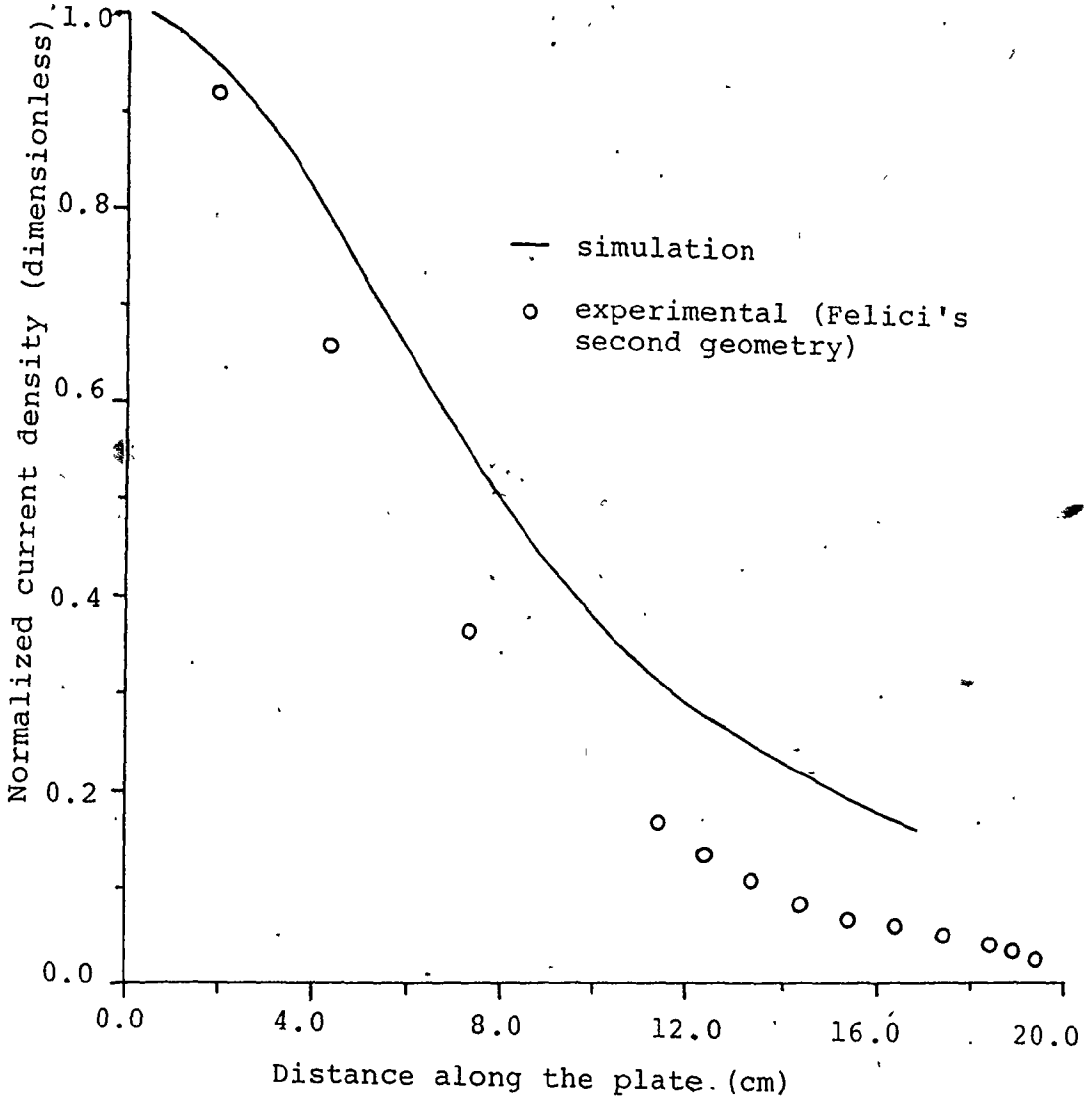

V_c = 17.7 kV r_c = 0.13 mm

J_ℓ = 0.1 mA/m h = 0.1 m

b = 2.2 x 10^{-4} $m^2/V.s$ s = 0.2 m

Figure 5.15. The normalized current density distribution along the collecting plate

The drop off in the magnitude of the experimental data, as we approach point E, is physically because the charge density at that point is equal to zero. Therefore, if one visualizes an infinitesimal area at that point and measure the current flowing through that infinitesimal area, it should be equal to zero. This is difficult to achieve experimentally because of construction limitations of the current detection device.

To investigate this, the model was applied to Tassicker's [29] geometry and operating conditions. Tassicker used a microprobe for measuring the current density at the collecting plate, thus his technique of measurement is probably more accurate than the segmented electrode technique adopted by Felici.

Figure 5.16 shows the current density distribution of positive corona for Tassicker's geometry and operating conditions which were as follows: $h = 0.11$ m, $s = 0.1$ m, $r_c = 0.15$ mm and $J_\ell = 0.1$ mA/m. The ion mobility used was 1.8×10^{-4} $m^2/V.s$. It is evident from this figure that there is a closer fit of the simulation results to the experimental results as compared to figure 5.13 (Felici's geometry), since the percentage difference between the two has dropped to less than 0.5 percent close to point (A). For Tassicker's geometry under negative corona, the simulation results gave good agreement to the experimental

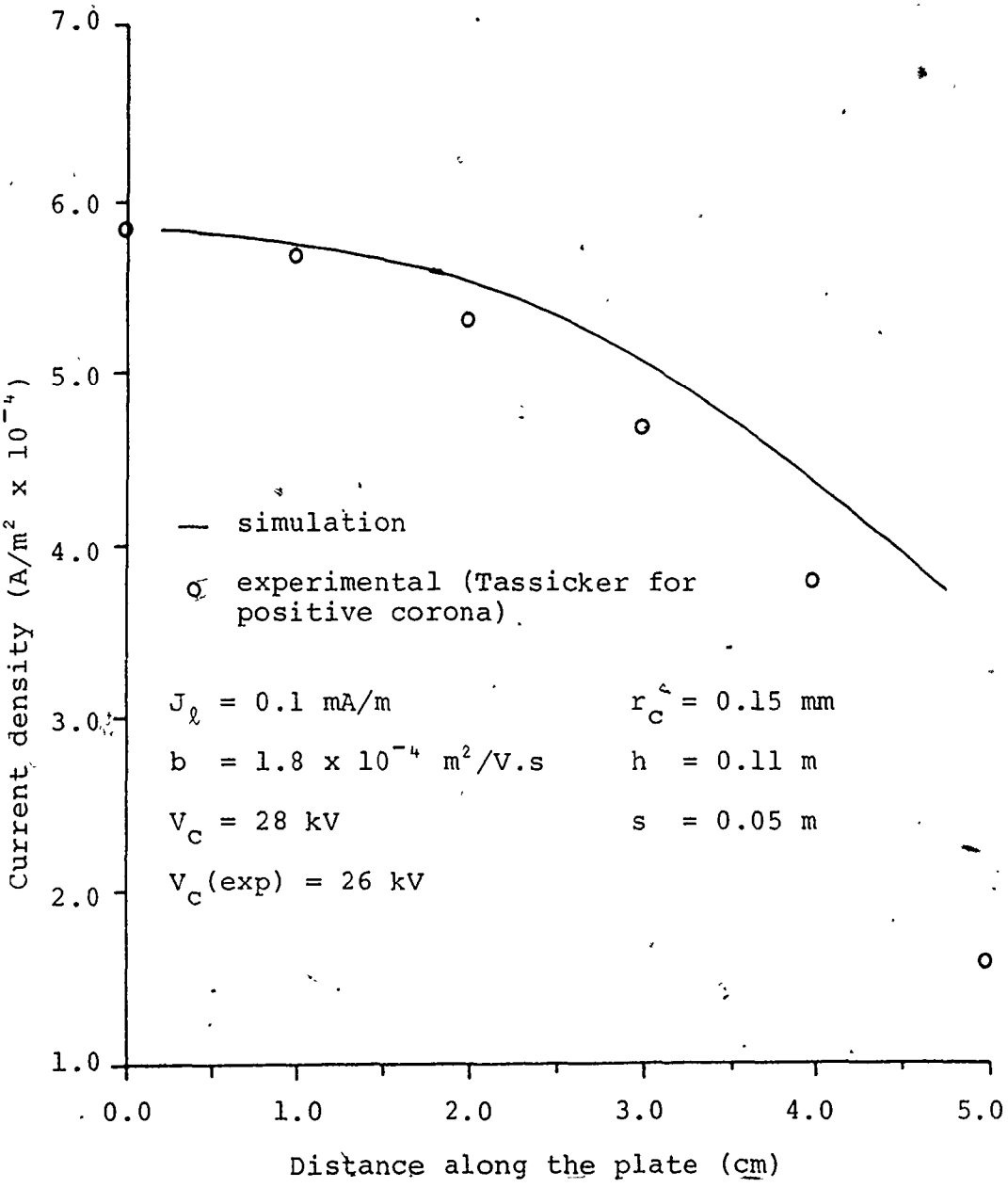

Figure 5.16. The current density distribution along the collecting plate

data as for the positive corona. It was also found that the simulation results are higher than the experimental data as we approach the center line (E-C) as was the case in both of Felici's geometries.

5.3.2 Sensitivity of Corona Model

The sensitivity of the model is defined here as the variations that occur in the output results when changes are made to the input parameters while maintaining the precipitator dimensions constant. Two important input parameters were investigated independently, those were the ion mobility b_i and the linear current density J_ℓ. It was also of importance to investigate how the model is affected by neglecting the finite thickness of the corona ionization zone and the assumption that the corona wire is a uniform ion emitting source.

The following precipitator geometry and operating linear current density were choosen for the above investigation: r_c = 0.127 mm, h = 0.1 m, s = 0.05 m and J_ℓ = 0.34 mA/m, these values correspond to the conditions used in the experimental work that will be cited in chapters seven and eight.

The assumed value of ion mobility that was used as a reference was equal to 1.8×10^{-4} $m^2/V.s$, in which case the wire potential V_c, evaluated by applying the developed model to the above conditions, was equal to 37 kV.

To investigate the sensitivity of the model to variations in the magnitude of ion mobility, the ion mobility was increased from 1.8 to 1.9 and 2.2×10^{-4} $m^2/V.s$, these correspond to a percentage increase of 5.6% and 22% respectively. The result was that the value of V_c decreased to 36.2 and 34.1 kV respectively. This is expected since it is a well known fact that the higher the ion mobility, the higher is the current, provided that the voltage is maintained constant. It was also found that the electric field at the collecting wall was reduced by 2.8% and 9.5% for the increased value of ion mobility, although the corresponding reductions in the wire potential V_c were only 2.2% and 7.8% respectively. This difference between the drop in the electric field at the wall and the wire potential is probably due to the non-linearity of the problem.

To investigate the sensitivity of the model to variations in the linear current density, the ion mobility was assigned it's original value and the value of J_ℓ was increased once by 10% and the second time by 30% from 0.34 mA/m to 0.37 and 0.44 mA/m resectively. This resulted in

the increase of V_c by 4.0 and 10.2 percent, from 37 kV to 38.5 and 41.2 kV respectively. The increase in potential was accompanied by an increase in the electric field at the collecting wall by about 4.6 and 10.6 percent respectively. Again the non-linearity is observed.

To investigate the effect of neglecting the ionization zone in the developed model, a process similar to the one used in the cylindrical case was used. The process is based on initiating the field line trajectories from a circular circumference of $r = 3r_c$ rather than $r = r_c$. Also the electric field at this new boundary is equated to E_o at $r = r_c$ as evaluated by Peek's formula . Finally, the wire potential V_c is evaluated at $r = r_c$.

The above process gave a value of 36.99 kV for the wire potential V_c as opposed to the value of 37 kV obtained by the original model which neglects the presence of an ionization zone. No variations were observed, when applying the above process, in any other electrical parameters.

The preceding analysis indicates that the output results of the model are sensitive to variations in the magnitude of the ion mobility and the linear current density, which are input parameters to the model. Actual variations in the ion mobility value may be encountered

during experimental work due to variations in temperature, pressure and humidity [67]. Also variations in the magnitude of the corona current may occur as a result of corona instability. Such variations are in the range of ±10%.

The above analysis also indicates that neglecting the ionization zone and assuming that the corona wire is an ion emitting source is a reasonable assumption.

Thus the developed model is believed to be suitable for the purpose of predicting the electrical characteristics of duct-type precipitators. It also eliminates the cost and time needed in constructing and experimenting with proto-type models to measure similar electrical characteristics.

CHAPTER SIX

PRESENT STATUS OF WIDE-DUCT ELECTROSTATIC PRECIPITATORS

6.1 Introduction

In recent years there has been increased interest in the use of wide-duct precipitators, particularly in Japan and Europe. Some authors [68,69] have shown that the precipitator efficiency increased or remained unchanged as the duct spacing was increased for the same precipitator volume. This was under the condition that the applied voltage is correspondingly increased to maintain a constant average gap field, $E_{av} = V_c/h$. This appears to be in contradiction to the Deutsch equation (6.1).

$$\eta = 1 - \exp(-A\omega/v_g) \tag{6.1}$$

Since the collection area is decreased with the increase of duct spacing, these results would seem to imply an increase in the magnitude of the particle migration velocity, ω. Although it is known that the effective migration velocity is governed by a number of factors including electrical, mechanical and aerodynamic, the classical value for this term may be calculated using equation (6.2).

$$\omega = \frac{2P\varepsilon_0 E_p E_c a}{3\mu} \qquad (6.2)$$

From equation (6.2), it can be seen that the migration velocity is proportional to the precipitating field E_p at the collecting wall as well as the charging field E_c. This equation has long been considered to be independent of the duct spacing, but the recently observed enhanced performance of wide-duct spacings, suggests that the migration velocity is a function of the duct spacing. Many theories and experiments have been presented to explain the so called wide spacing effect and are discussed in the following sections.

6.2 Proposed Theory and Experiments for Wide-Duct Electrostatic Precipitators

Heinrich [69,70] proposed a theoretical explanation based on the classical Deutsch equation. According to his theory equation (6.1) can be written as follows.

$$\eta = 1 - e^{-k} \qquad (6.3)$$

where $$k = A\omega/v_g = cI_c/v_g \qquad (6.4)$$

c being a constant that is determined experimentally.

White [71] suggested another relation in which k is given below as.

$$k = c' P/v_g \qquad (6.5)$$

where c´ is also a constant to be determined experimentally.

In both equations (6.4) and (6.5), the collection area no longer appears. It is interesting to observe that in equation (6.5) the efficiency is expressed as a function of power input per volume rate of flow, whereas in equation (6.4) the efficiency is expressed as a function of current input per volume rate of flow.

Misaka et. al [68] made experimental investigations using fly ash samples and changing the spacing from 0.25 m to 0.75 m, while keeping the wire to wire spacing constant. The applied voltage V_c, was changed proportionally with the spacing h, so as to preserve a constant average inter-electrode field $E_{av} = V_c/h$. They observed that the migration velocity ω increased with the increase of duct spacing. Another important observation was that the electric field at the collecting walls also increased with the increase of duct spacing, this was stated to be the result of the added space charge in the larger spacings.

Noso [72] carried out experimental studies which were based on constant current density operation for all the duct spacings investigated. He showed that the performance of wide spacing is not always superior to the conventional

spacing in duct-type electrostatic precipitators, but rather depends on the gas and dust conditions. Furthermore, wide-duct spacings are not suitable for high dust concentrations because of the excessive sparking. Thus it is recommended, for cases where wide-duct spacing is economically justified but high dust concentrations are involved, to use a conventional spacing in the first field where the concentration is high and use wider spacing for the following fields where the concentration is less due to precipitation in the first field. More recently, this view has been shared by Lindau and Matts [73]. Finally, Noso recommended an optimum spacing of 0.4 to 0.6 m from the view points of performance and cost.

Matts [74] showed experimentally and by developing a formula for the precipitator efficiency, that increasing the duct spacing would give better performance only if the precipitator efficiency is originally high at the conventional spacing. He also observed that for low gas velocities, increasing the duct spacing does not enhance the precipitator performance. This was thought to be the result of the reduced turbulence.

Masuda and co-workers [75] conducted experiments in a wet-type electrostatic precipitator for the following two duct spacings: 0.25 and 0.5 m. When doubling the spacing, while maintaining a constant average electric field (E_{av} =

V_c/h) for the two spacings of 3.2 kV/cm, the migration velocity was more than doubled (2.16 times). When further increasing E_{av} to 4 kV/cm for the larger spacing a further rise in ω was achieved (2.51 times).

Golkowski [76] developed a simplified electrical model for the duct-type electrostatic precipitator using lumped parameters. He showed that the migration velocity ω is proportional to the duct spacing through the following equation.

$$\omega = \frac{K}{A} I_c^2 R_g \qquad (6.6)$$

where K is a scaling factor that is determined experimentally and R_g is the resistance of the inter-electrode gap excluding the resistance at the two electrodes. Since R_g, according to [76], is proportional to h, therefore ω is also proportional to h.

6.3 Characteristic Features of Wide-Duct Precipitators

The increase of duct spacing at a constant precipitator volume results in cost reductions for the discharge and collecting electrodes, rapping elements and construction. On the other hand, the higher voltage required results in cost increases for the power pack, insulators, bushings etc. Therefore the magnitude of the duct spacing, providing the maximum economical advantage,

is largely dependent on the precipitator size. It is recommended [75] not to resort to wide spacing if the gas volume to be handled is less than 1000 m^3/min.

A distinct advantage is the ease in maintenance work enabled by the increased gap. For wet-type precipitators the quantity of irrigation water needed and the capacity of the water treatment system are reduced. The wide-duct spacing is particularly attractive for roof-mounted precipitators because of the reduced total weight.

The technical optimum value of duct spacing lies usually in the range of 0.4 to 0.6 m [75]. The corresponding voltage is 80 - 150 kV.

6.4 Electrical Characteristics of Wide-Duct Precipitators

It is evident, from the above discussions, that wide-duct precipitators are gaining wide popularity primarily because of the cost reductions achieved without sacrificing performance.

Most of the studies performed on wide-duct precipitators, as presented in section 6.2, seem to concentrate on the performance of such precipitators and little attention, if any, is given to the electrical characteristics persisting in such precipitators. It is

proposed that a comparative study of the electrical characteristics of wide-duct precipitators to those of conventional spacings, can give some insight to the so called wide spacing effect.

This can be readily achieved by implementing the developed corona model [77] for duct-type electrostatic precipitators. This model is expected to be more accurate when applied to wide-duct spacing, as opposed to standard spacing, since the increased spacing is more compatible to the assumptions used in the model.

No experimental data was found in the literature for the electrical conditions in wide-duct precipitators. Thus experiments were carried out on a laboratory scale electrostatic precipitator. Details of the experimental set-up and the measuring techniques are given in chapter seven.

CHAPTER SEVEN

EXPERIMENTAL SET-UP

7.1 General Description of the Apparatus

The experimental set-up is given schematically in figure 7.1. It consists of a section of a duct-type electrostatic precipitator, which had one fixed plate while the other was movable and could be adjusted to achieve plate to plate spacings of 0.2, 0.4 and 0.6 m. The corona wires used were 0.25 mm in diameter and made of chromel-A. The wire to wire spacings could be varied in multiples of 0.05 m. The wires were energized from a common bus bar connected to a high voltage D.C. power supply. The two plates were grounded, either directly or through an ammeter. A current probe similar in concept to that of Tassicker's [78] was used for monitoring the current density distribution at the fixed plate along the x - direction. An exhaust fan was placed at one end of the precipitator to prevent the build-up of ozone concentrations due to corona discharge.

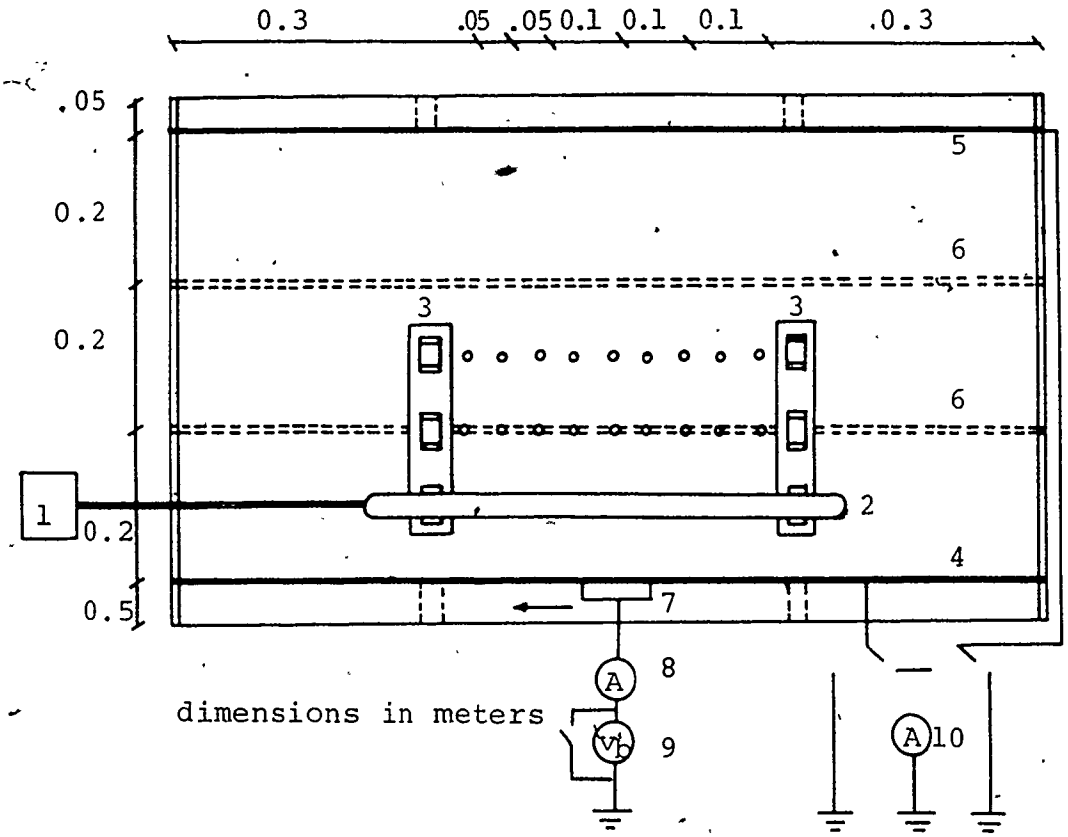

1. High voltage D.C. supply
2. Bus bar
3. Bus bar supports
4. Fixed plate
5. Movable plate
6. Slots for movable plate
7. Probe and probe support
8. Electrometer
9. D.C. power supply
10. Ammeter

Figure 7.1. Schematic top view of the experimental set-up

7.2 Power Supply

The power supply used was a Universal Voltronics high voltage D.C. power supply, model BAL 100-18. The output voltage was continuously adjustable from zero to 100 kV with a maximum output current of 18 mA. The output voltage was measured using the meter provided on the control panel of the power supply and was calibrated with respect to the potential drop measured across a 100 MΩ high voltage resistor immersed in an oil tank and grounded through a digital milliammeter.

7.3 Measurement of Plate Current

The ground wire from each plate was connected to a switching board which allowed for the measurement of the total corona current or the measurement of each plate current independently. For the three duct spacings investigated, it was found that the percentage difference between the two plate currents was less than 3%. This indicates that for all the duct spacings, the corona wires were reasonably aligned half way between the two plates.

7.4 Design of Current Probe and Mobile Support

A special current probe was built and mounted on a mobile support. The latter was then mounted on the fixed plate through a slot such that it could be moved horizontally (in the x-direction), along the center line of the fixed plate, a distance of 0.1 m to the left and right of the central corona wire.

A schematic diagram of the current probe and it's support is shown in figure 7.2. The probe support consists of a rectangular galvanized steel plate to which was glued a rectangular plexi-glass block.

The current probe consisted of a short length of magnet wire that was soldered at one end to a panel mount B.N.C. female connector. The other end, was set flush with the probe plate surface as shown in figure 7.2. The B.N.C. connector was fixed to the plexi-glass block using four screws.

7.4.1 Measurement of Current Density

The probe current, in the order of nano amperes, was measured by a Keithley Instruments electrometer model 602. To evaluate the current density the value of the measured current was divided by the probe surface area which was

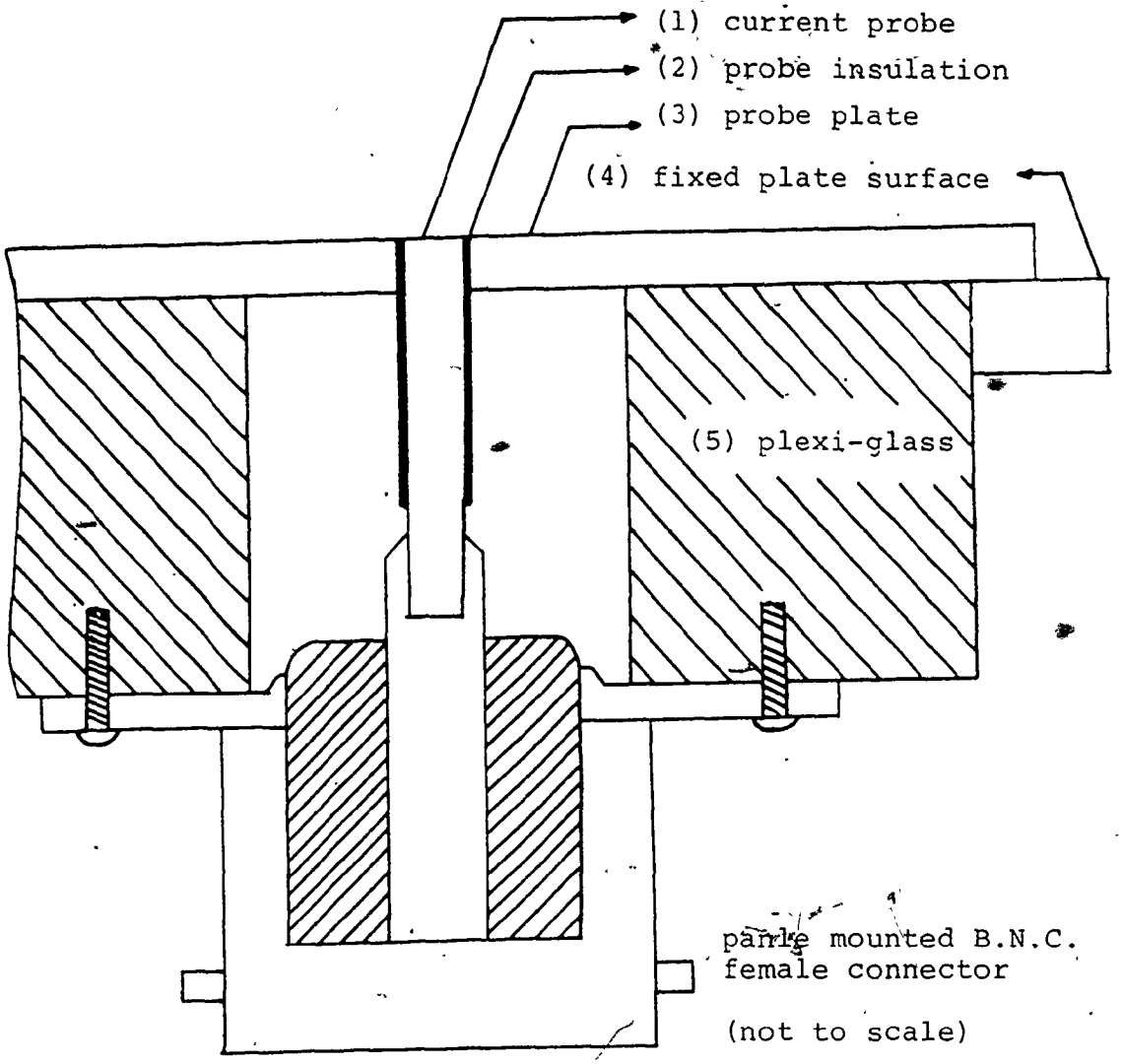

dimensions:

(1) probe diameter = 0.126 mm
(2) insulation thickness of probe = 0.05 mm
(3) thickness of probe plate = 1.6 mm
(4) thickness of fixed plate = 3.2 mm
(5) thickness of plexi-glass = 25.0 mm

Figure 7.2. Schematic diagram of the current probe (after Tassicker [78])

equal to 1.28×10^{-6} m^2.

7.4.2 Measurement of Electric Field

The technique developed by Tassicker [78] was adopted here to evaluate the electric field at the fixed plate. The complete details of Tassicker's technique and related theory are given in Appendix 5.

7.5 Experimental Difficulties

The major difficulties that were encountered during experimentation are discussed below.

7.5.1 Effect of Exhaust Fan

When measurements of the current density distribution were performed, it was found that the corresponding readings to the left and the right of the central wire were not identical. The higher values were consistently observed at the plate portion nearer to the precipitator outlet. This was determined to be the result of the ion drift by the action of the exhaust fan. This was overcome by turning the fan "OFF" during measurements and later turning it "ON" between each experiment to allow for the ozone removal.

7.5.2 Choice of Polarity

When measuring the probe currents under negative corona large fluctuations were observed and in some cases the current would drop to about 10% of it's nominal expected value. This was because the current probe had a relatively small surface area, thus it was very sensitive to the corona localized glow points or tufts that appear in rapid motion on the wire surface in negative corona [9]. Thus it was found necessary to use positive corona to obtain more stable readings from the current probe.

7.5.3 Determination of Linear Corona Current

Initially only three corona wires were used. For the three duct spacings: 0.2, 0.4 and 0.6 m, the average linear corona current density J_ℓ (later referred to as J_ℓ(average)) was held constant at 0.1 mA/m. This was achieved by increasing the applied voltage until the total corona current measured from the two plates was equal in magnitude to the value calculated by equation (7.1).

$$I_{tot} = J_\ell \cdot (\text{No. of wires x length of a single wire}) \quad (7.1)$$

The three precipitator geometries were applied to the charge simulation model using a mobility value of 1.8×10^{-4} $m^2/V.s$, a wire to wire spacing of 0.1 m, while maintaining

a value of 0.1 mA/m for the linear corona current. The output voltage V_c evaluated by the model showed very good agreement to the corresponding experimental value for the smallest duct spacing of 0.2 m. This was not the case for the larger spacings. It was found that the model gave values of V_c greater than the experimental values by 7% and 19% for the 0.4 and 0.6 m spacings respectively.

When the number of wires were increased to 5 while maintaining the same value of 0.1 mA/m for the average linear corona current, the above percentage differences dropped to 2% and 6.5% resepectively. It should be noted here that only the experiments were repeated while it was not necessary to repeat the computer runs since they are independent of the number of wires as long as symmetry is preserved.

From the above results and from theoretical expectations, it is clear that if an array of corona wires are energized from one bus bar, each corona wire will emanate a different value of corona current per unit length. The outer wires, which are subjected to lesser opposing electric fields, will contribute the largest value of linear corona current, while the central wire will contribute the smallest value of linear corona current. This phenomena has also been observed and investigated by Lawless and Sparks [79].

In the case considered here the corona onset voltage V_o predicted by the model for the increasing order of duct spacing was 10.9, 15.1 and 19.3 kV. These values are slightly higher than the experimental values of 10.3, 14.5 and 18 kV. This is as expected, since the corona model assumes a constant onset potential for all corona wires, whereas for the experimental set-up the effect of end wires is to cause the outer wires to reach corona at a potential lower than that of the inner wires. Since the experimental onset potentials documented here correspond to those of the outer wire, thus it makes sense that their values should be lower than those predicted by the corona model.

To evaluate the corona onset potential for the central wire, the formula developed by Lawless and Sparks was used [79]. Applying this formula to the three duct spacings: h = 0.1, 0.2 and 0.3 m, it was found that the corona onset potential at the central wire was equal to 10.8, 16.1 and 22.4 kV, while the corona onset potential at the outer wires was equal to 9.9, 13 and 16.3 kV respectively. It is interesting to observe that the value of onset potential predicted by the corona model, lies in between the values of onset potential predicted for the central and outer wires using Lawless and Spark's relation. This was found to be the case for the three duct spacings investigated.

According to the preceeding analysis, it is clear that for an array of wires connected to the same bus bar, the onset potential for each wire is different. This difference approaches zero for an infinite number of wires such as assumed in the charge simulation model. This explains the better agreement observed between the corona model results and the experimental results for five wires as compared to three wires. Based on this, further agreement may be achieved by increasing the number of corona wires in the experimental set-up. This was not done because of construction limitations.

Since the apparatus was constructed without the provision for measuring the corona current emanating from each wire independently, it was considered sufficient to evaluate the linear corona current J_ℓ of the central wire by integrating the measured current density distribution along the plate from a point below the central wire to the center line between corona wires, as shown by equation (7.2).

$$J_\ell = 4 \int_0^s J.dx \qquad (7.2)$$

The value of J_ℓ evaluated from equation (7.2) was used (later referred to as J_ℓ(integrated)) as the input parameter to the charge simulation model, rather than the average experimental linear current density that was evaluated by equation (7.1). Using this new value of J_ℓ in

the developed model gave good agreement to the experimental data for all the duct spacings investigated. This is clearly seen from Table 7.1.

7.6 Experimental Procedure and Results

Prior to each set of experiments the corona wires and the probe plate were cleaned with petroleum solvent (Varsol). Weights were added to the ends of the corona wires to ensure straightness and minimum vibration. All experiments were conducted at room temperature and pressure. The ambient relative humidity ranged from 40 to 65 percent.

The experiments were repeated a minimum of four times for each geometry and for each operating condition. The Reproducibility achieved ranged from 3% to 12% for moderate and low values of linear current density respectively.

From these results, the validity of the charge simulation model can be confirmed for wide duct electrostatic precipitators. This is performed in the next chapter together with an analysis of some important electrical characteristics of wide duct precipitators.

Table 7.1 Comparison of simulation results to the experimental data

Wire to Wire Spacing (2s) (m)	Wire to Plate Spacing (h) (m)	Experimental Applied Voltage (V_c(exp)) (kV)	Linear Corona Current (mA/m)		Wire Potential as Evaluated by Charge Simulation Model (kV)	
			J_ℓ (average) According to Equ.(7.1)	J_ℓ (integrated) According Equ.(7.2)	$V_c \equiv J_\ell$ (avg)	$V_c \equiv J_\ell$ (integ)
0.1	0.1	22.5	0.1	0.1	23.4	23.4
0.1	0.2	49	0.1	0.082	53.5	49.2
0.1	0.3	77	0.1	0.066	92.2	76.7

CHAPTER EIGHT

ANALYSIS OF WIDE-DUCT PRECIPITATORS IN CLEAN AIR CONDITIONS

8.1 Introduction

The objective of this chapter is to determine the changes in the electrical conditions that occur in duct-type precipitators as the duct spacing is increased. This involves the evaluation of the electric field, the potential, the current density and charge density distributions in clean air conditions.

The corona model [77], presented in chapter five, is used here along with the experimental measurements that were performed on the experimental set-up presented in chapter seven.

8.2 Wide-Duct Spacing in Clean Air

In this study the only geometric parameters are the wire to plate spacing (h), and the wire to wire spacing (2s). The corona model is applied to a duct precipitator with variable duct spacing under the following two general operating conditions:

a) Constant linear corona current J_ℓ.

b) Constant wire potential V_c.

The results of each operating mode are presented separately in the following sub-sections.

8.2.1 Constant Linear Corona Current Density

For a variable duct spacing precipitator the following two cases were investigated under the condition of constant linear corona current density J_ℓ.

i) Constant spacing between corona wires (2s).

ii) Constant ratio of wire to plate and wire to wire spacing (h/2s).

In both cases, the corona wire radius was equal to 0.127 mm (as in the experimental set-up), the linear corona current J_ℓ was held constant at 0.1 mA/m and the ion mobility was assumed equal to 1.8×10^{-4} $m^2/V.s$ corresponding to the condition for positive corona.

In the first case, the wire to wire spacing was held constant at 0.1 m. It is important to mention here that this case corresponds to constant current density at the collecting walls. The three wire to plate spacings investigated were similar to those achieved experimentally, h = 0.1, 0.2 and 0.3 m,

Figures 8.1 to 8.3 give the experimental and simulation results for the current density distribution at the collecting plate for the three duct spacings. The corresponding electric field distributions at the plate are given in figures 8.4 to 8.6.

As expected, using J_ℓ (integrated) gives better agreement to the experimental data for the duct spacings of 0.2 and 0.3 m. For the smallest spacing both the average and integrated linear current densities were equal, as seen from figures 8.1 and 8.4.

Since, in this section it is only intended to investigate the operational mode of constant linear corona current, then only the simulation results which used J_ℓ (average) = 0.1 mA/m will be considered in the following discussion.

It can be seen from figures 8.1 to 8.3, that the potential necessary for maintaining a current of 0.1 mA/m was 23.4, 53.5 and 92.2 kV for spacings of 0.1, 0.2 and 0.3 m respectively. This corresponds to an average field ($E_{av} = V_c/h$) of 2.3, 2.7 and 3.1 kV/cm. Thus an increase in the duct spacing by a factor of 3, required an increase of potential by a factor of 3.9 to maintain the same current.

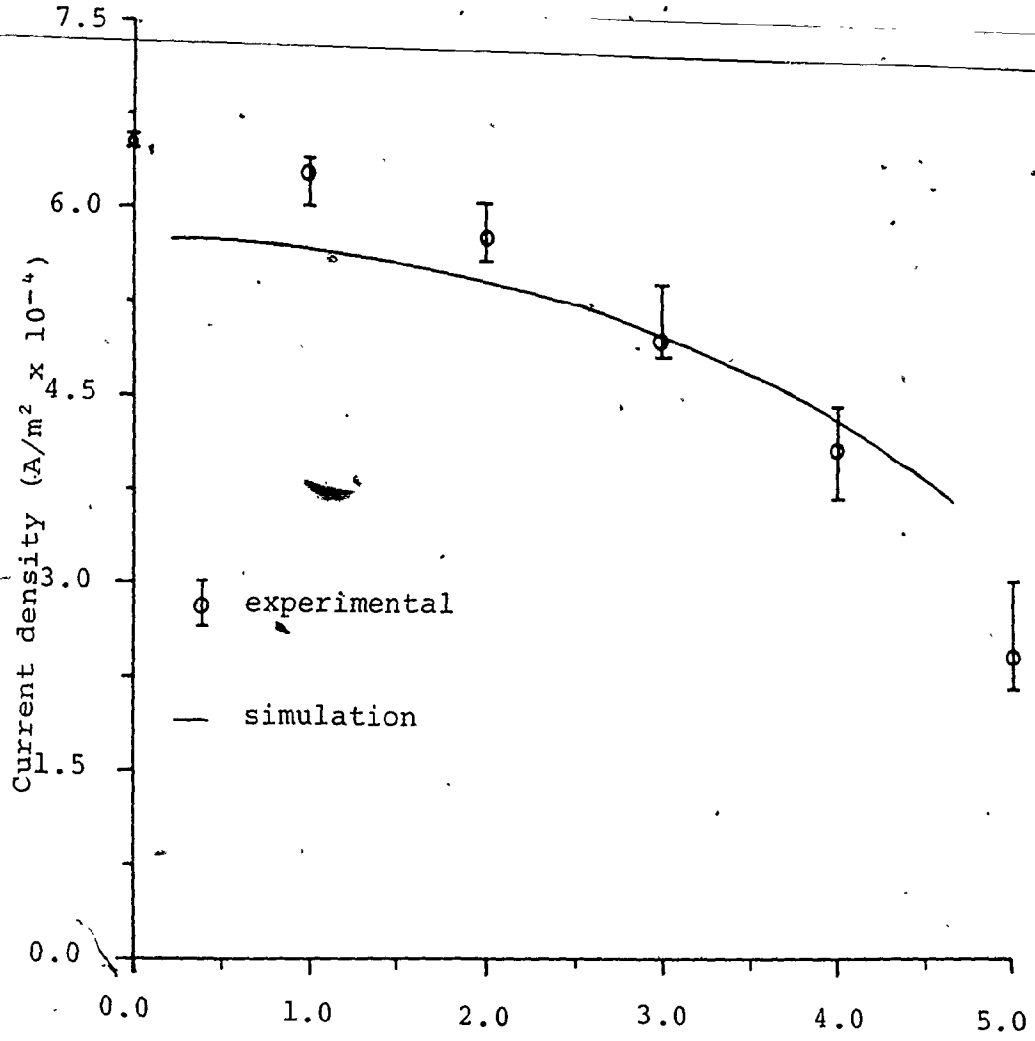

r_c = 0.127 mm

h = 0.1 m

s = 0.05 m

J_ℓ (integrated) = 0.1 mA/m

J_ℓ (average) = 0.1 mA/m

$V_c \equiv$ (integrated) = 23.4 kV

$V_c \equiv$ (average) = 23.4 kV

V_c(exp) = 22.5 kV

Figure 8.1. Experimental and simulation current density distributions at the collecting plate for h = 0.1 m.

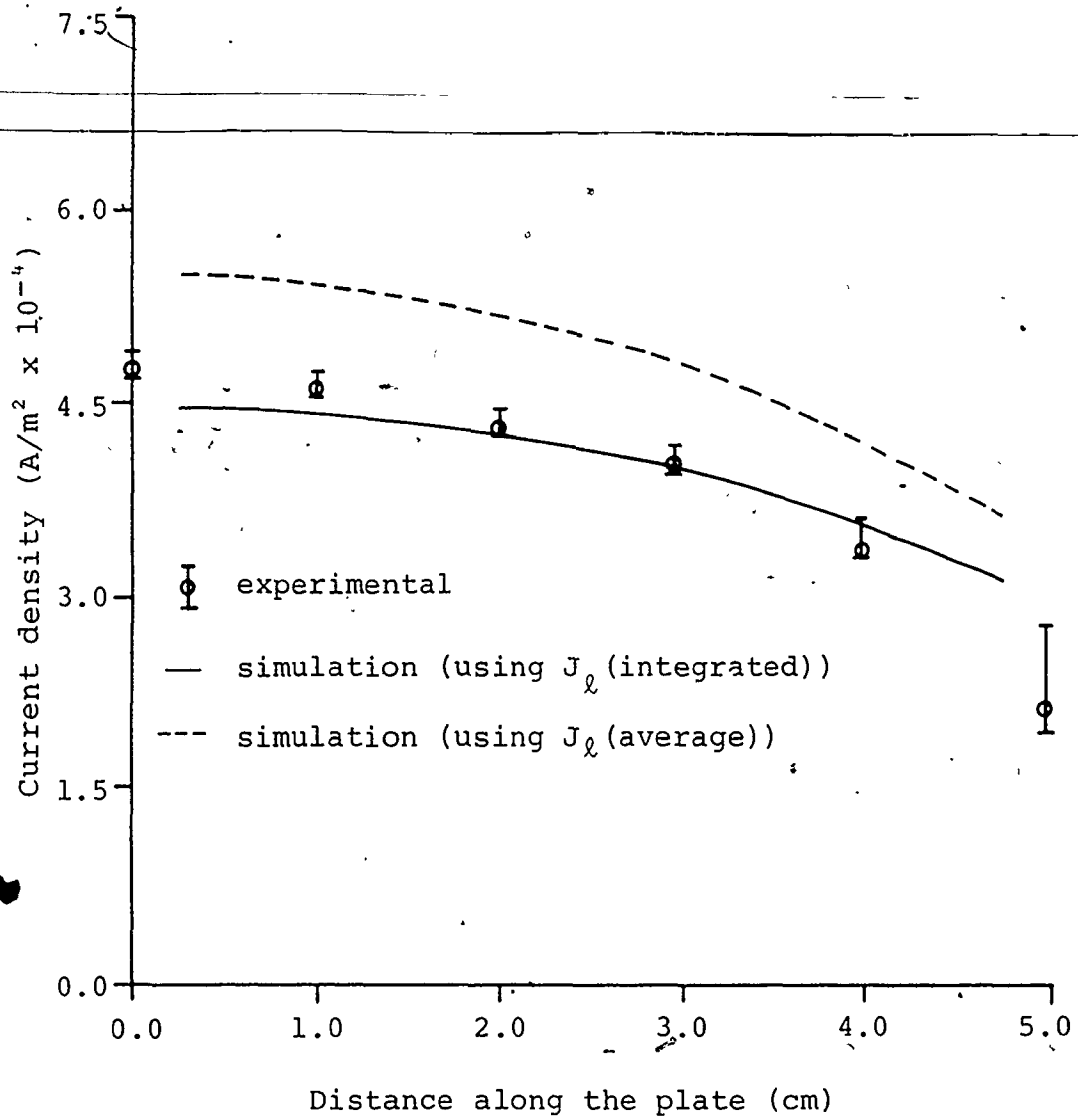

r_c = 0.127 mm

h = 0.2 m

s = 0.05 m

J_ℓ (integrated) = 0.08 mA/m

J_ℓ (average) = 0.1 mA/m

$V_c \equiv$ (integrated) = 49.2 kV

$V_c \equiv$ (average) = 53.5 kV

V_c (exp) = 49.0 kV

Figure 8.2. Experimental and simulation current density distributions at the collecting plate for h = 0.2 m.

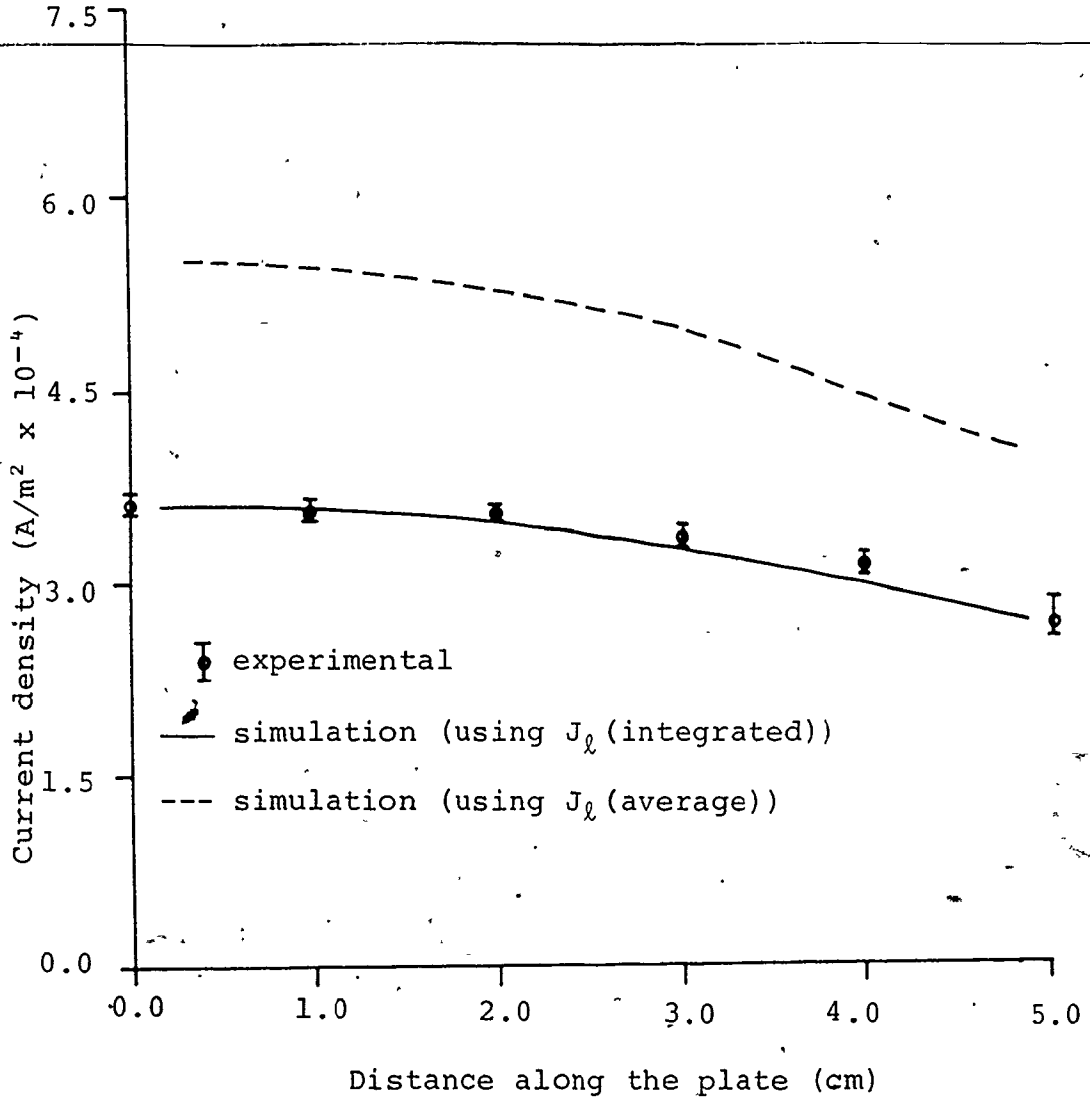

r_c = 0.127 mm

h = 0.3 m

s = 0.05 m

J_ℓ (integrated) = 0.066 mA/m

J_ℓ (average) = 0.1 mA/m

$V_c \equiv$ (integrated) = 76.7 kV

$V_c \equiv$ (average) = 92.2 kV

V_c(exp) = 77.0 kV

Figure 8.3. Experimental and simulation current density distributions at the collecting plate for h = 0.3 m

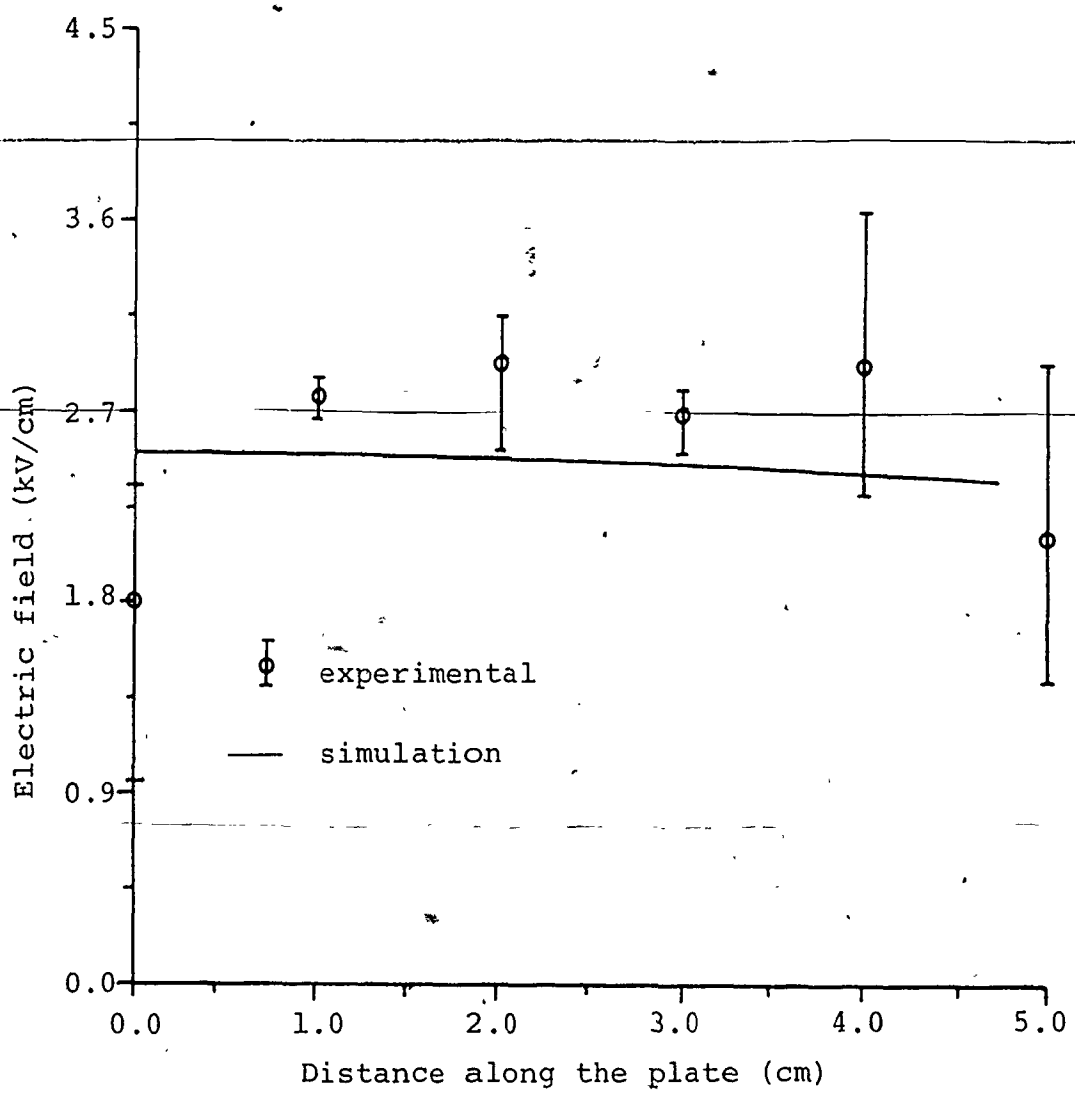

r_c = 0.127 mm J_ℓ (integrated) = 0.1 mA/m

h = 0.1 m J_ℓ (average) = 0.1 mA/m

s = 0.05 m $V_c \equiv$ (integrated) = 23.4 kV

$V_c \equiv$ (average) = 23.4 kV

V_c(exp) = 22.5 kV

Figure 8.4. Experimental and simulation electric field distributions at the collecting plate for h = 0.1 m

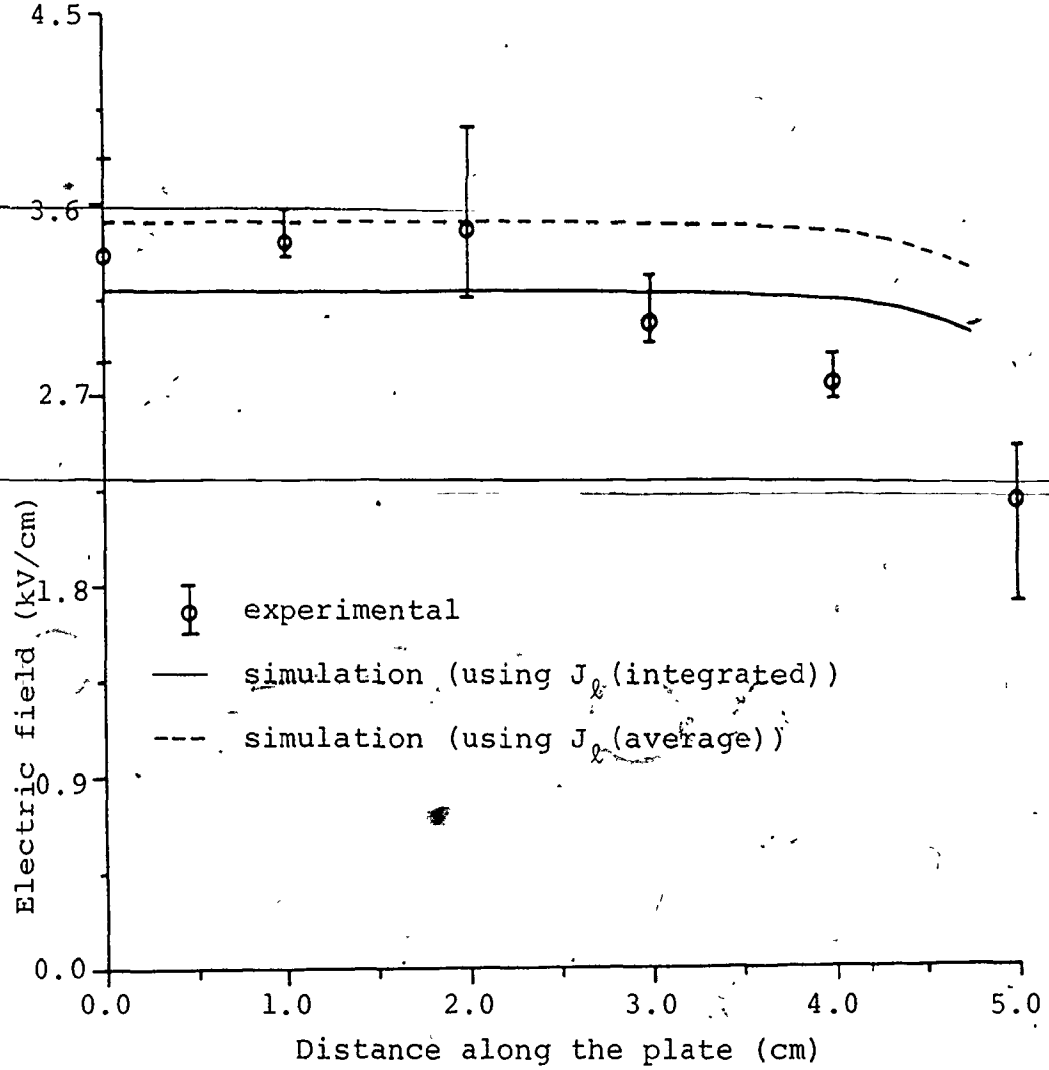

r_c = 0.127 mm J_ℓ(integrated) = 0.08 mA/m

h = 0.2 m J_ℓ(average) = 0.1 mA/m

s = 0.05 m $V_c \equiv$ (integrated) = 49.2 kV

$V_c \equiv$ (average) = 53.5 kV

V_c(exp) = 49.0 kV

Figure 8.5. Experimental and simulation electric field distribution at the collecting plate for h = 0.2 m

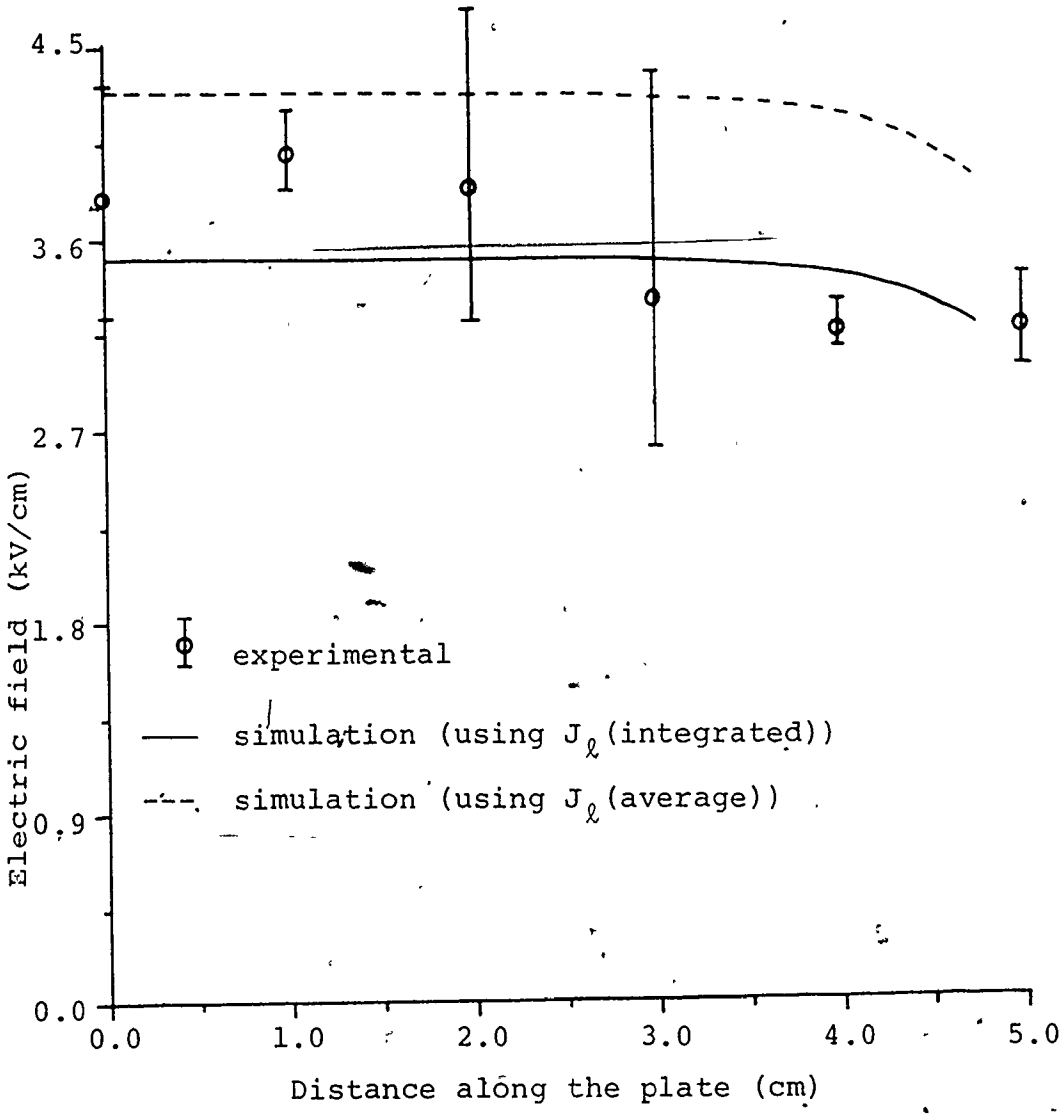

r_c = 0.127 mm J_ℓ(integrated) = 0.066 mA/m

h = 0.3 m J_ℓ(average) = 0.1 mA/m

s = 0.05 m $V_c \equiv$(integrated) = 76.7 kV

$V_c \equiv$(average) = 92.2 kV

V_c(exp) = 77 kV

Figure 8.6. Experimental and simulation electric field distributions at the collecting plate for h = 0.3 m

From figure 8.1, it is seen that the current density distribution drops off in magnitude towards the center line between corona wires. This is in agreement to the experimental observations of Felici [30] and Tassicker [29]. Increasing the wire to plate spacing from 0.1 to 0.2 and 0.3 m, as in figures 8.2 and 8.3 respectively, resulted in a more uniform current density distribution at the collecting walls. This is due to the increased uniformity of space charge adjacent to the collecting walls, as indicated by the results of the corona model for the three duct spacings, while maintaining the linear corona current constant.

Although the experimental results for the electric field distribution at the collecting plate vary within a relatively large range (see figures 8.4 to 8.6), the simulation results (particularly when using J_ℓ (integrated)) give a reasonably good fit to them. From these figures, it is seen that for a constant linear corona current of 0.1 mA/m the electric field at a point directly below the wire was 2.5, 3.5 and 4.3 kV/cm for the increasing order of duct spacing. The wider the duct spacing the more is the decrease in the electric field near the center line between corona wires. The field drops to 2.4, 3.3 and 3.8 kV/cm at this center line for the same increasing order of duct spacing.

From figure 8.7, it is also seen that the charge density at the walls decreased as the duct spacing was increased. This is expected, since for the three spacings investigated the linear corona current J_ℓ was held constant, thus a reduction in the charge density had to exist to counteract the increase in field as the duct spacing was increased.

It was also of interest to notice that the point of minimum field, along a line extending from wire to plate, was always approximately 2 cm away from the corona wire regardless of the duct spacing and that the field distributions along that line were similar for the three spacings investigated. This is shown in figure 8.8. It is interesting to compare these results with those of Sekar [25]. Referring to his figure 7 it can be seen that he also showed that the point of minimum field, along the same line, occured approximately 2 cm away from the corona wire. However, the field distributions were different in magnitude probably because he had different current levels for the three spacings. This phenomena could be a possible explanation to the experimental observations of Inculet et. al [80]. In their work, they were charging pellets by shooting them in a direction parallel to a corona wire in a cylindrical geometry. This was performed for the entire inter-electrode space in the radial direction. They observed that adjacent to the wire the charge acquired by

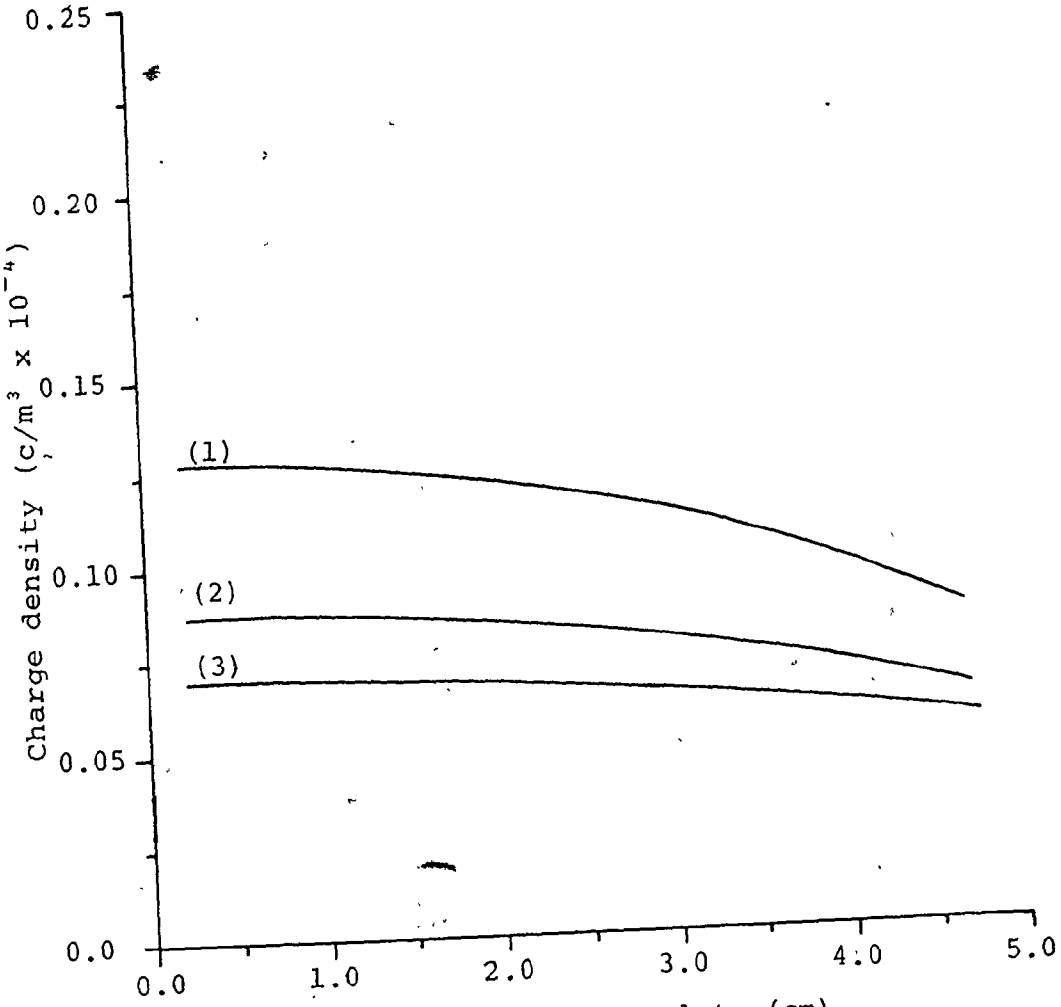

(1) h = 0.1 m, V_c = 23.4 kV
(2) h = 0.2 m, V_c = 53.5 kV
(3) h = 0.3 m, V_c = 92.2 kV

J_ℓ = 0.1 mA/m
r_c = 0.127 mm
s = 0.05 m

Figure 8.7. Ionic charge density distributions along the plate under constant linear current density.

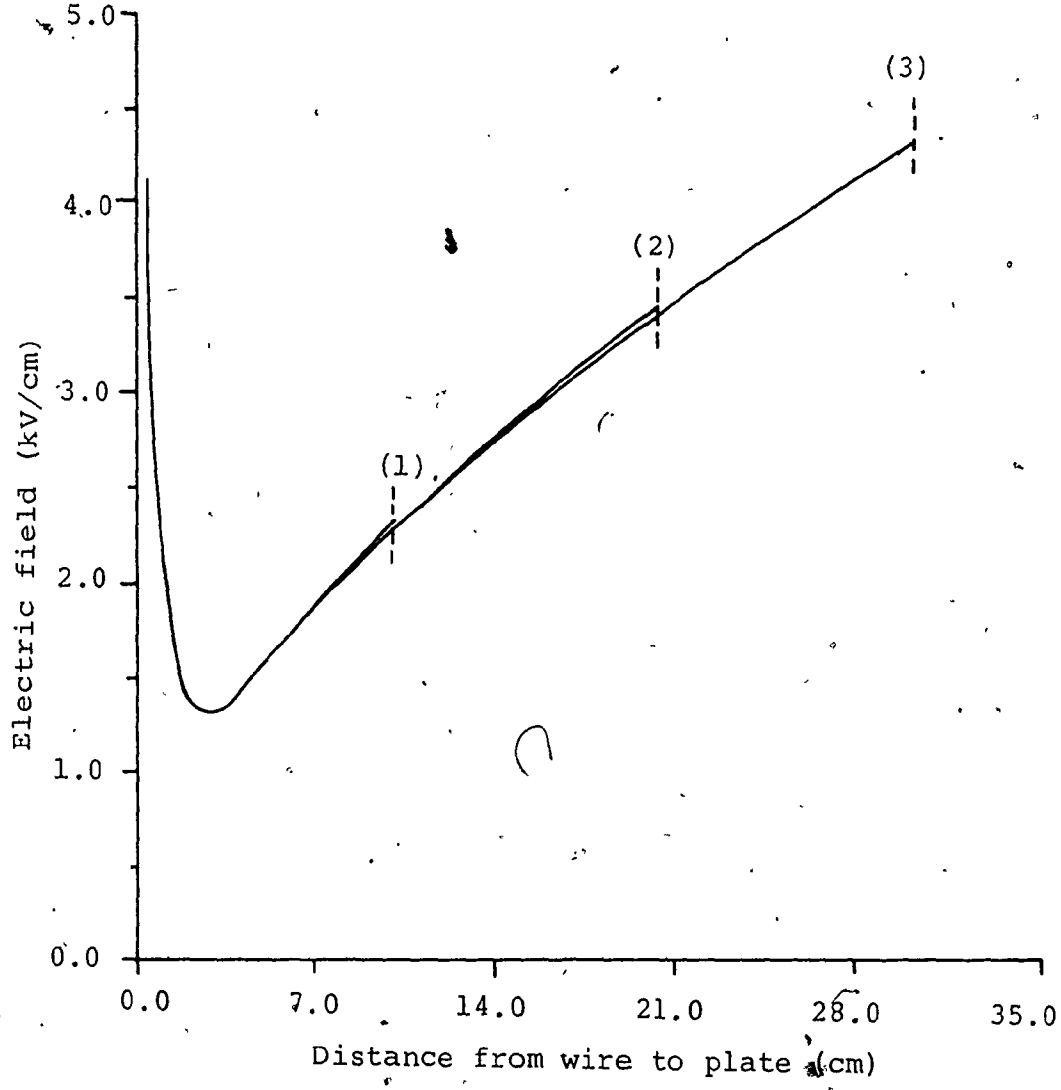

(1) h = 0.1 m, V_c = 23.4 kV

(2) h = 0.2 m, V_c = 53.5 kV

(3) h = 0.3 m, V_c = 92.2 kV

J_ℓ = 0.1 mA/m

r_c = 0.127 mm

s = 0.05 m

Figure 8.8. Electric field distribution along a line extending from wire to plate under constant linear current density

the pellets was relatively high and dropped to a minimum at about 2 cm away from the corona wire and then increased again further out in the gap. According to the previous analysis, it is most likely that the point where minimum charging occured (adjacent to the wire) corresponds to the point of minimum field.

In the second case, the ratio of wire to plate and wire to wire spacing was held constant at 2:1, while keeping J_ℓ = 0.1 mA/m. The three spacings investigated were similar to those of the first case.

The potential that was required to maintain the prescribed current was 30.4, 53.5 and 76.6 kV for the duct spacings of 0.1, 0.2 and 0.3 m respectively. Thus for a constant ratio (h/2s), the increase in potential to maintain the same current level was a factor of 2.5, when tripling the duct spacing. This is considerably lower than that for the first case (constant s), where the factor was 3.9.

The field distributions along the plate for the three spacings are shown in figure 8.9. It is interesting to observe that all the distributions have nearly the same value along the plate, with the smallest spacing having the highest magnitude.

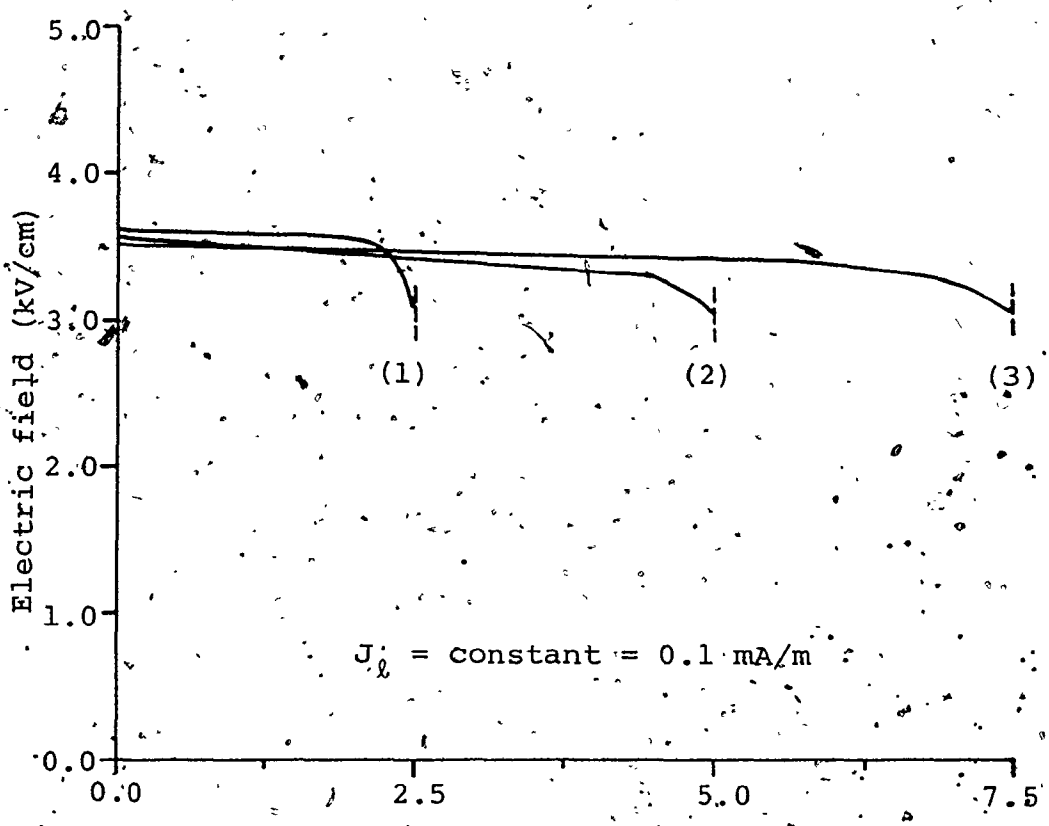

(1) h = 0.1 m, 2s = 0.05 m V_c = 30.4 kV

(2) h = 0.2 m, 2s = 0.10 m V_c = 53 kV

(3) h = 0.3 m, 2s = 0.15 m V_c = 76.6 kV

Figure 8.9. Electric field distribution along the plate for constant (h/2s) and constant linear corona current

It was also found that for the three spacings, the point of minimum field along a line extending from wire to plate was at about 2 cm away from the corona wire.

Table 8.1 includes some of the significant data for the previously presented precipitator dimensions operated at a constant linear corona current of 0.1 mA/m. In the table, the ratio of the electric field at the plate (E_p) to the average electric field in the gap ($E_{av} = V_c/h$) is defined as the electric field enhancement factor.

From this table it can be seen that for a constant wire to wire spacing the field enhancement factor increases from 1.1 at h = 0.1 m to 1.4 at h = 0.3 m, but what is more significant is that the absolute value of the average field (E_{av}) is increased by 35% and similarly the value of the field at the plate is increased by 72%. This implies better precipitator performance, since the particle charging and precipitating fields are both increased. Considering that the migration velocity ω, is proportional to ($E_{av}E_p$), then for the above percentage increases, the predicted increase in migration velocity would be 132% or more than doubled.

To achieve the above percentage increases, the applied potential had to be increased by a factor of four, while the collecting area was reduced only by a factor of three

Table 8.1. Field enhancement factor for variable duct spacings under constant linear corona current = 0.1 mA/m

	Wire to Wire Spacing (m)	Wire to Plate Spacing (m)	Voltage (kV)	E_{av} (kV/cm)	E_p (kV/cm)	Ratio E_p/E_{av}
Constant Wire to Wire Spacing	0.1	0.1	23.4	2.3	2.5	1.1
	0.1	0.2	53.5	2.7	3.5	1.3
	0.1	0.3	92.9	3.1	4.3	1.4
Constant Ratio of (h/2s) = 2:1	0.05	0.1	30.4	3.0	3.6	1.2
	0.10	0.2	53.5	2.7	3.5	1.3
	0.15	0.3	76.6	2.6	3.5	1.4

(assuming constant precipitator volume). This represents a typical situation where the economic factors governing the capital and operating costs of the precipitator have to be carefully considered to justify the increased duct spacing.

For a constant ratio of (h/2s), the field enhancement factor increased from 1.2 at h = 0.1 m to 1.4 at h = 0.3 m. This was not accompanied by an increase in the average field, but rather a reduction was observed. Similarly, the field at the plate was insignificantly changed. Thus compared to the case of constant wire to wire spacing, one would not expect any enhanced collection in the precipitator performance.

From table 8.1, it is also observed that reducing the wire to wire spacing by one half while keeping the duct spacing constant, would require an increase of about 30% in potential to maintain the same current. This is accompanied by an increase of 30% and 44% in the average and plate fields respectively, or rather an increase of 87% in the migration velocity.

From the analysis of table 8.1, the following conclusions can be made for an operating mode of constant linear corona current.

i) For a given precipitator volume, increasing the duct spacing while keeping the wire to wire spacing constant, can enhance the precipitator performance. For this case, capital cost reductions are achievable as a result of reducing the number of corona wires, collecting electrodes, supporting members, rapping elements etc. On the other hand, as a result of the higher voltage needed, cost increases are encountered in the power supplies, insulators, bushings etc. As for the operating costs, the corona power per wire is increased while the total number of wires is decreased and thus the net change in costs will depend upon the relative magnitudes of these factors. Furthermore, cost reductions may be expected in maintenance. Thus this approach for performance enhancement, has also to be studied from the economical point of view.

ii) For a given precipitator volume, increasing the duct spacing while keeping (h/2s) constant, will not lead to any enhancement in the precipitator performance and may also result in cost increase. The cost increase in this case would probably be less than that for case (i), since the increase of duct spacing is also accompanied by a decrease in the number of corona wires between each two successive plates. This in turn reduces the amount of necessary accessories such as bushings, power supplies etc.

iii) Finally, for a given precipitator volume within the range of experimental parameters studied here, the results suggest that reducing the wire to wire spacing while keeping the duct spacing constant should enhance the precipitator performance. However, this method of performance enhancement is accompanied by increase in costs.

8.2.2 Constant Wire Potential

For this mode of operation, the wire to wire spacing was held constant at 0.1 m, the corona wire radius was 0.127 mm and the potential was fixed at 35 kV. The three duct spacings investigated were 0.1, 0.2 and 0.3 m.

The value of the linear current density J_ℓ at the central wire, corresponding to V_c = 35 kV, was evaluated by integrating the measured current density distribution at the plate (refer to equation (7.2)). These integrated values for J_ℓ were found to be equal to 320^{+13}_{-10}, $34^{+2.4}_{-1.0}$ and $7^{+0.9}_{-0.8}$ μA/m for the duct spacings of 0.1, 0.2 and 0.3 m respectively.

From the above experimental ranges, it can be concluded that for a more stable corona, such as for the smallest duct spacing, the experimental error is relatively decreased.

The above values of J_ℓ were applied (as input parameters) independently to the corona model along with their respective geometrical values. The value of ion mobility used was 1.8×10^{-4} $m^2/V.s$ corresponding to positive corona.

Results of the model indicated that the potential V_c necessary to maintain the above values of linear current densities was 36, 35 and 33kV for the increasing order of duct spacing. The reason for the slight deviation of the calculated potentials from the experimental value of 35 kV, is probably due to the experimental error in measuring the current density.

The electric field distributions at the collecting plate for the three spacings, as evaluated by the model and measured experimentally, are shown in figure 8.10.

Figures 8.11 to 8.13, give the current density distributions at the collecting plate for the three duct spacings.

It was of interest, in this case, to find that the average ionic charge density along a line extending from wire to plate was reduced to 50% and 7% for h = 0.2 and 0.3 m respectively, as compared to h = 0.1 m. The corresponding reductions in the average electric field

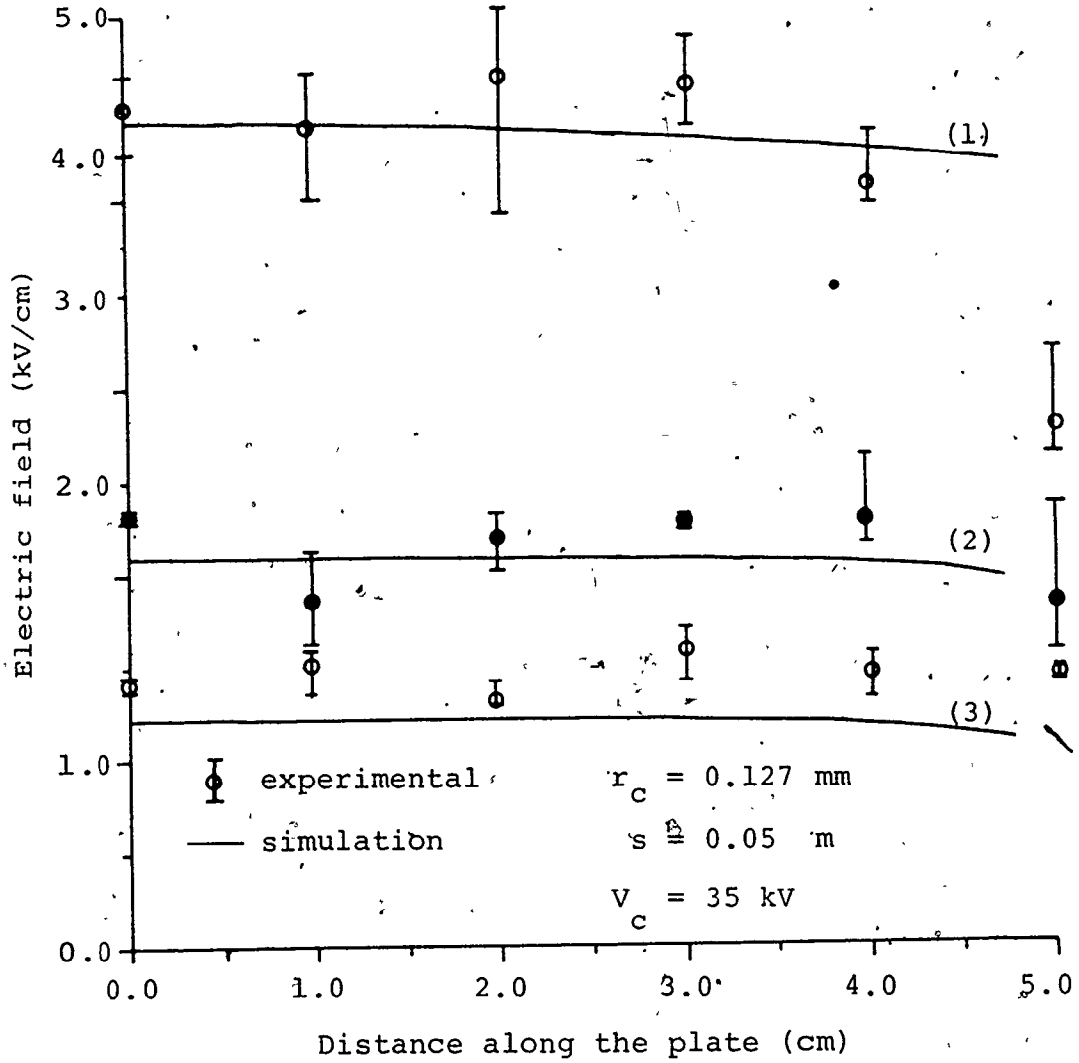

(1) h = 0.1 m J_ℓ = 0.320 mA/m

(2) h = 0.2 m J_ℓ = 0.034 mA/m

(3) h = 0.3 m J_ℓ = 0.007 mA/m

Figure 8.10: Experimental and simulation electric field distribution along the collecting plate at constant operating potential.

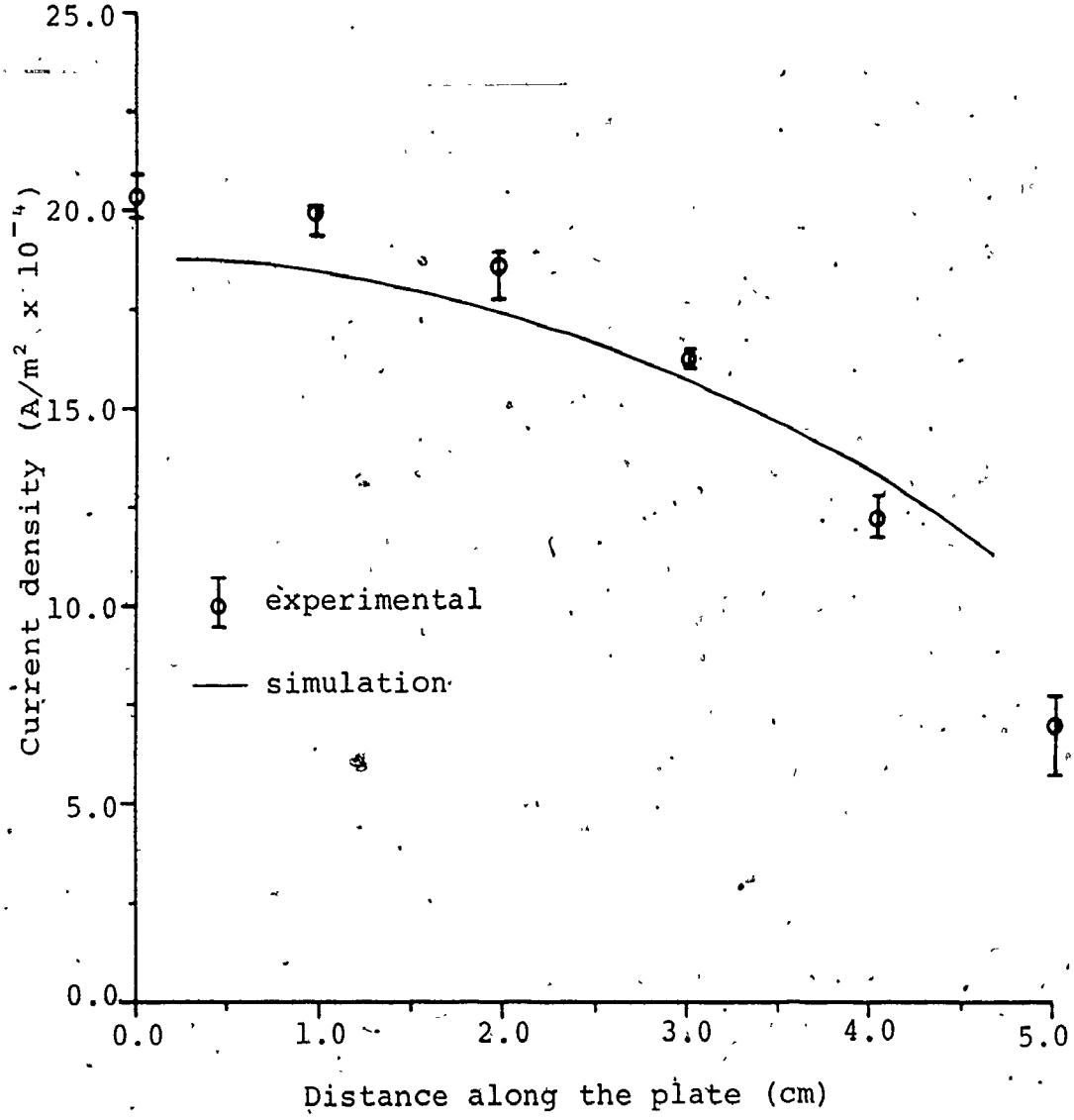

r_c = 0.127 mm J_ℓ = 0.32 mA/m

h = 0.1 m V_c = 36 kV

s = 0.05 m V_c(exp) = 35 kV

Figure 8.11. Experimental and simulation current density distributions at the collecting plate for constant applied potential and h = 0.1 m

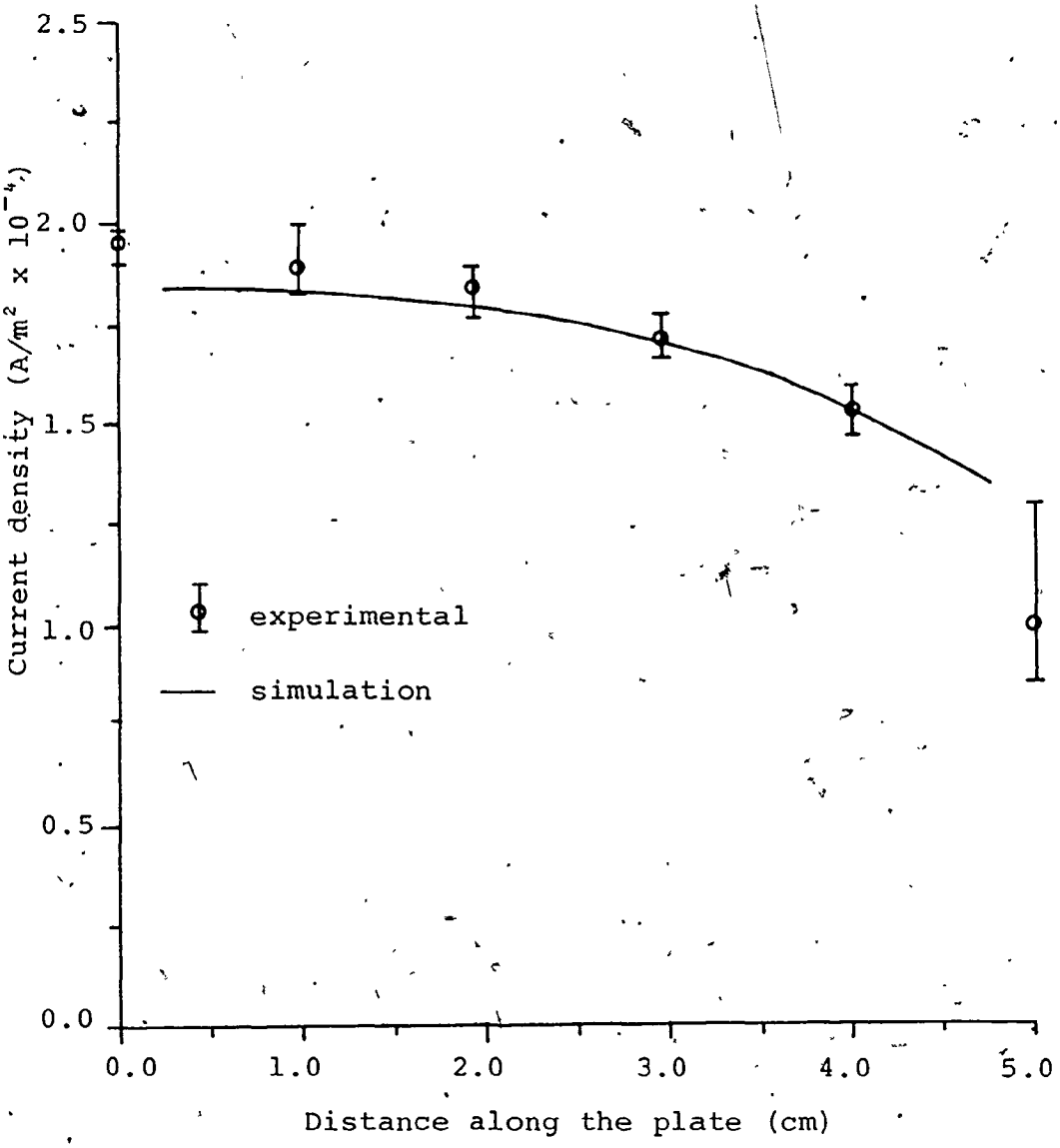

r_c = 0.127 mm J_ℓ = 0.034 mA/m

h = 0.2 m V_c (exp) = 35 kV

s = 0.05 m V_c (exp) = 35 kV

Figure 8.12. Experimental and simulation current density distributions at the collecting plate for constant applied voltage and h = 0.2 m

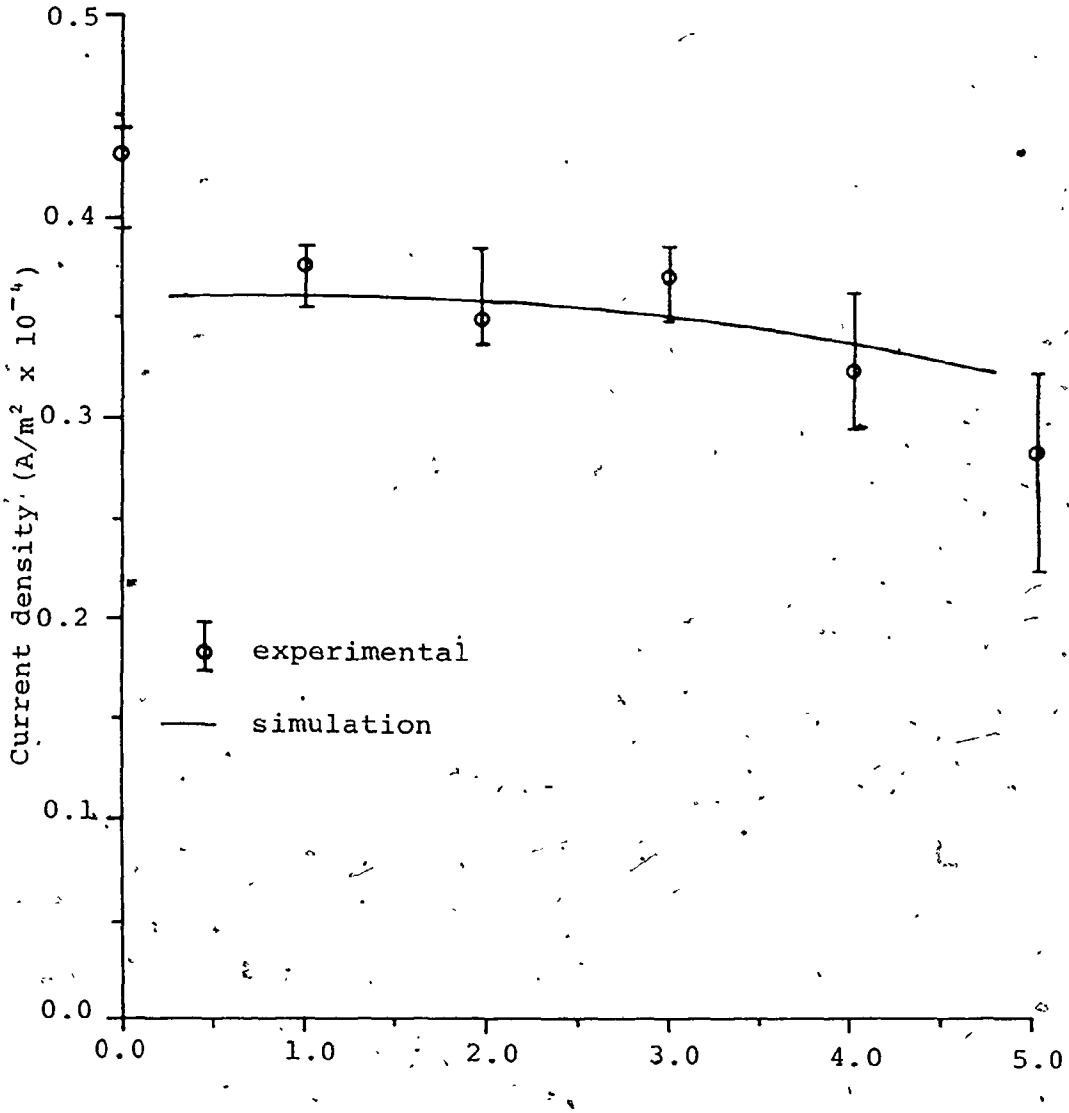

r_c = 0.127 mm J_ℓ = 0.007 mA/m

h = 0.3 m V_c = 33 kV

s = 0.05 m V_c(exp)= 35 kV

Figure 8.13. Experimental and simulation current density distribution at the collecting plate for constant applied voltage and h = 0.3 m .

(E_{av}) were 51% and 28%. The large difference between both percentage reductions for the largest duct spacing is probably because the electrostatic field (at 35 kV) is comparable in magnitude to the electric field due to ion space charge. This is more clearly understood by evaluating the ratio of the average electrostatic field (V_o/h) to the average ionic field (V_c/h) for the three duct spacings. When this was performed the results were: 31, 43 and 55% for the increasing order of duct spacing.

Table 8.2 includes some of the significant data for the previously presented precipitator dimensions operated at a constant potential of 35 kV.

It is clear from this table, that increasing the duct spacing while keeping the applied potential constant will result in the degradation of the precipitator performance. This is simply because of the reduction in both the average and the plate fields (E_{av} and E_p respectively), which leads to a reduction in the migration velocity ω.

So far the corona model only accounts for ionic space charge. It is of significant practical interest to observe the changes in the electrical conditions if space charge effects due to charged particles were also considered, for both the conventional and wide duct spacings. This study is presented in the following chapter.

Table 8.2. Field enhancement factor for variable duct spacings under constant applied voltage = 35 kV

Wire to Wire Spacing (m)	Wire to Plate Spacing (m)	Voltage (kV)	Linear Current Density, J_ℓ (mA/m)	E_{av} (kV/cm)	E_p (kV/cm)	Ratio E_p/E_{av}
0.1	0.1	35	0.320	3.5	4.4	1.26
0.2	0.1	35	0.034	1.8	2.1	1.17
0.3	0.1	35	0.007	1.2	1.25	1.04

CHAPTER NINE

MODELING OF CORONA QUENCHING PHENOMENA FOR CONVENTIONAL AND WIDE DUCT PRECIPITATORS

9.1 Introduction

This chapter describes the results of an investigation of the corona quenching phenomena in conventional and wide-duct precipitators. The corona model presented in chapter five is modified here to account for particle space charge in the inter-electrode gap. The study involves the evaluation of the potential, the electric field, the ionic and particle space charge densities as well as the current density distributions. Particular consideration is given to the effect of particle space charge on the field enhancement at the precipitator walls in wide-duct precipitators and standard precipitators exposed to corona quenching.

9.2 Charge Simulation as Applied to Corona Quenching

An approach similar to the one used for the cylindrical geometry was adopted here to include the effect of particle space charge in the corona model developed for duct-type precipitators.

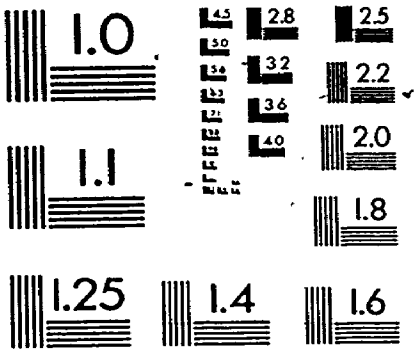

Thus, the calculation procedure involved evaluating the wire potential V_c required to maintain an assumed linear corona current J_ℓ. The wire potential was assumed to be made up of three components V_o, ΔV_i and ΔV_p. The first component being the corona onset potential V_o, the second ΔV_i represents the potential required to establish the ionic space charge (ρ_i) and the third ΔV_p represents the added potential drop due to the particle space charge ρ_p. Thus in figure 5.6, each line charge in an individual element was replaced by two line charges, one representing the ionic charge and the other representing the particle charge within the element.

As in the cylindrical case, it is assumed for the duct geometry that turbulent remixing maintains a uniform distribution of the particles across the duct. Therefore, the particles contribute zero net current in the field direction in this turbulent zone, in which case the current density in the turbulent zone is given as,

$$J = \rho_i b_i E \qquad (9.1)$$

On the other hand, in the region immediately adjacent to the grounded plate, previously referred to as the collecting zone, where the collection of the charged particles contributes a finite current component in the field direction, the current density is given as,

$$J = (\rho_i b_i + \rho_p b_p) E \qquad (9.2)$$

The value of the uniform particle space charge

density, ρ_p', is calculated as for the cylindrical case using equation (9.3).

$$\rho_p' = \xi\varepsilon_o PSE^*_{av} \qquad (9.3)$$

The corona quenching model differs from the corona in clean air model in the following respects:

i) Each element in the new model includes an extra line charge to account for the particle charge density. The magnitude of the line charge (q_p) is evaluated according to equation (9.4), which assumes a uniform particle space charge density, ρ_p', according to equation (9.3).

$$q_p = \rho_p'(\text{area of element}) \qquad (9.4)$$

ii) The current contributed by the charged particles according to equation (9.2) is only considered in the set of elements bounded by the last two equipotential contours (refer to figure 5.2).

iii) In carrying out the calculations in the simulation routine, the electrostatic case is first evaluated as in the previous model. Later, the uniform particle space charge density ρ_p' is evaluated according to equation (9.3). For each contour, the particle charge (q_p) within each element is evaluated using equation (9.4), while the ionic charges (q_i) within the same elements are evaluated such that they alone satisfy the current continuity equation.

Also for each contour the image charges that are required to preserve the boundary conditions take into consideration the added effect of the charged particles. In extending a trajectory out from one contour to the other, the particle charges (q_p) are treated in the same manner as the ionic charges (q_i).

9.3 Corona Quenching in Conventional Duct Spacing

In both models, corona in clean air and corona quenching, the linear corona current J_ℓ is defined as an input parameter and the wire potential V_c is obtained as one of the output parameters after the computer run has been completed. Thus a comparison of different precipitator geometries operated at the same current level is easily achieved. Comparisons based on constant voltage operation would be very costly in terms of computer time.

To obtain some insight as to what values of linear corona current J_ℓ should be used under conditions of dust loading to approximately achieve a constant operating voltage, several runs of both models were performed on a conventional duct spacing precipitator having the following dimensions: $h = 0.1$ m, $2s = 0.1$ m and $r_c = 0.127$mm.

When using the corona in clean air model, two linear current densities were investigated, 0.1 and 0.5 mA/m.

When using the corona quenching model, three values of J_ℓ were investigated, 0.01, 0.3 and 0.5 mA/m. For these three cases the dust loading ρ'_p was assumed equal to 0.44×10^{-4} C/m^3. From equation (9.3) this corresponds to, $S = 5$ m^2/m^3, $E^*_{av} = 5$ kV/cm, $P = 2$, $\xi = 1$ and $a = 5$ μm.

Results of the five runs were collected to approximate the two V-I characteristics shown in figure 9.1. From this figure it is obvious that predicting the corona suppression ratio necessary for maintaining a constant wire potential is a very difficult task and requires some iterative scheme.

It was of interest to observe the total charge density distributions (ionic + particle) along a line extending from wire to plate, these are given in figure 9.2. For the lowest current the ionic charge density was on the average about 9 percent of the total charge density, this increased to about 70 percent for the highest current.

Using the same precipitator geometry and holding J_ℓ constant at 0.5 mA/m, runs were performed using the corona quenching model for the following values of $\rho'_p = 0.0$, 0.44, 0.88 and 1.76×10^{-4} C/m^3.

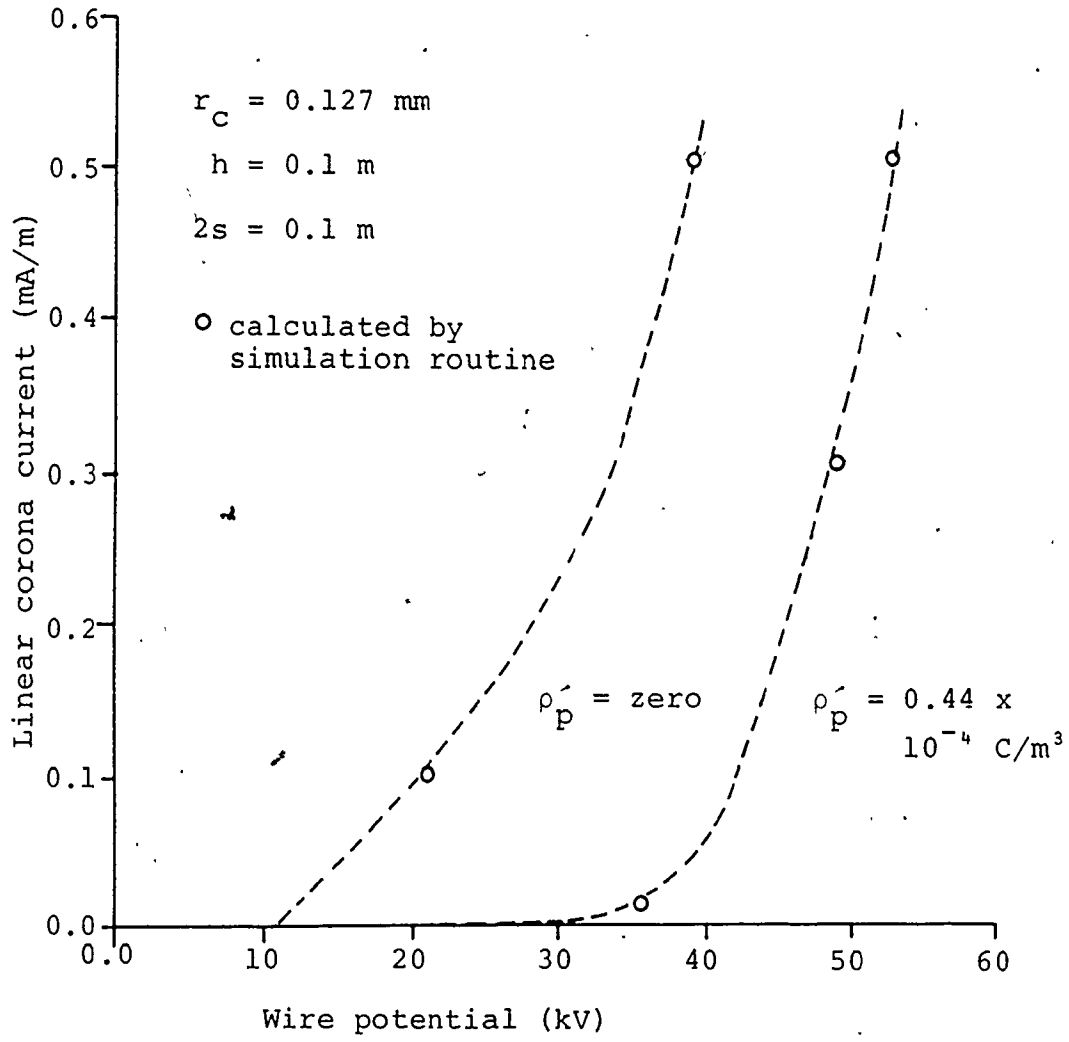

Figure 9.1. V-I characteristics for a conventional duct spacing precipitator under clean air and dust loading conditions

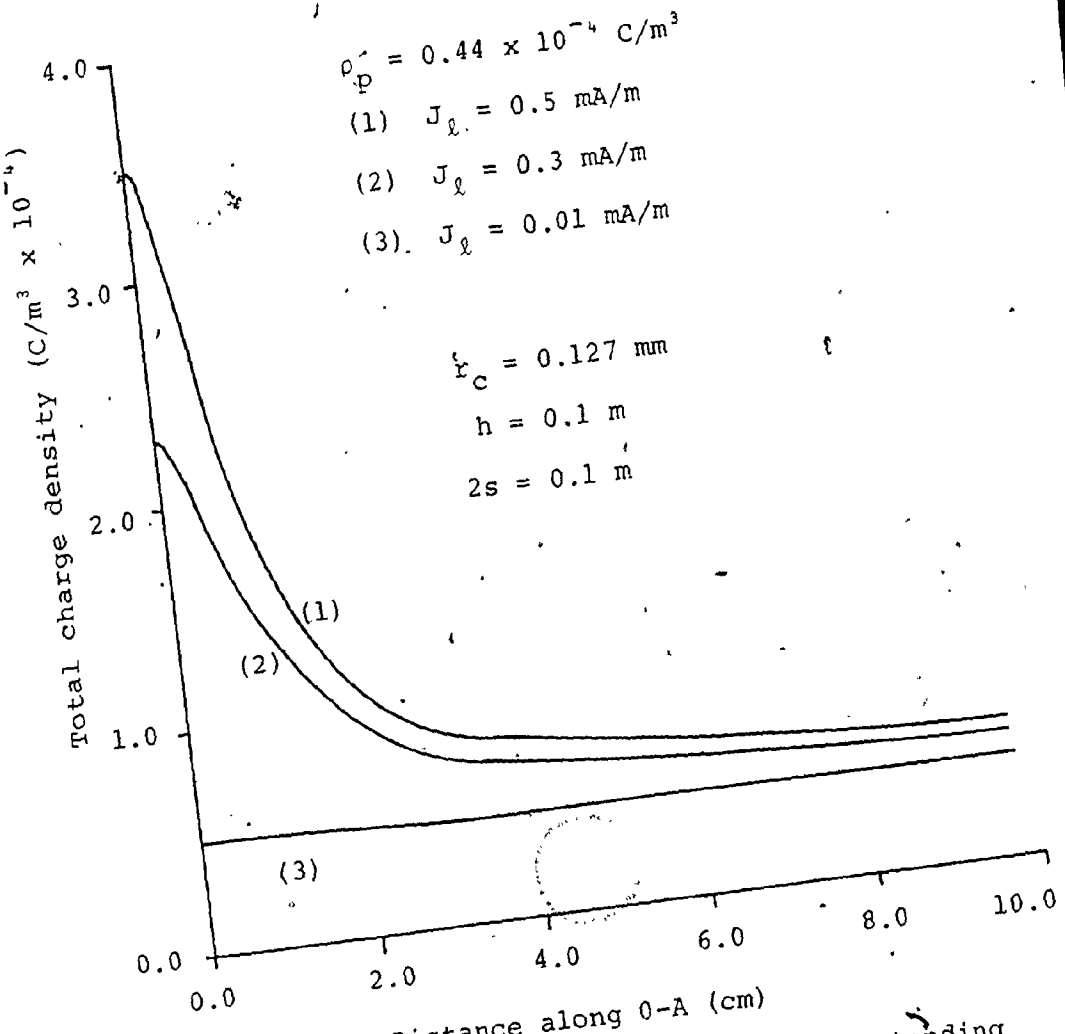

Figure 9.2. Total charge density along a line extending from wire to plate under dust loading

Figure 9.3 shows the voltage required to maintain this current for the different values of ρ_p. It is interesting to observe that this relation is linear indicating that the voltage drop ΔV_p due to particle space charge is directly proportional to the particle charge density.

The electric field at the plate at a point directly below the corona wire was 5.0, 8.6, 12.8 and 21.8 kV/cm for the increasing order of ρ_p. Such high values of electric field at the collecting wall would cause the precipitator to go into breakdown. This indicates that the assumed charging level for the particles cannot be attained physically. Thus either the linear corona current or the particle charging factor ξ or both have to be reduced to match real life operating conditions.

9.4 Corona Quenching in Wide-Duct Precipitators

To investigate the quenching phenomena in wide-duct precipitators, the three spacings previously presented in clean air were studied, those were 0.1, 0.2 and 0.3 m. For the three spacings, the wire to wire spacing was 0.1 m and r_c = 0.127 mm.

The above three spacings were investigated for the following two cases:

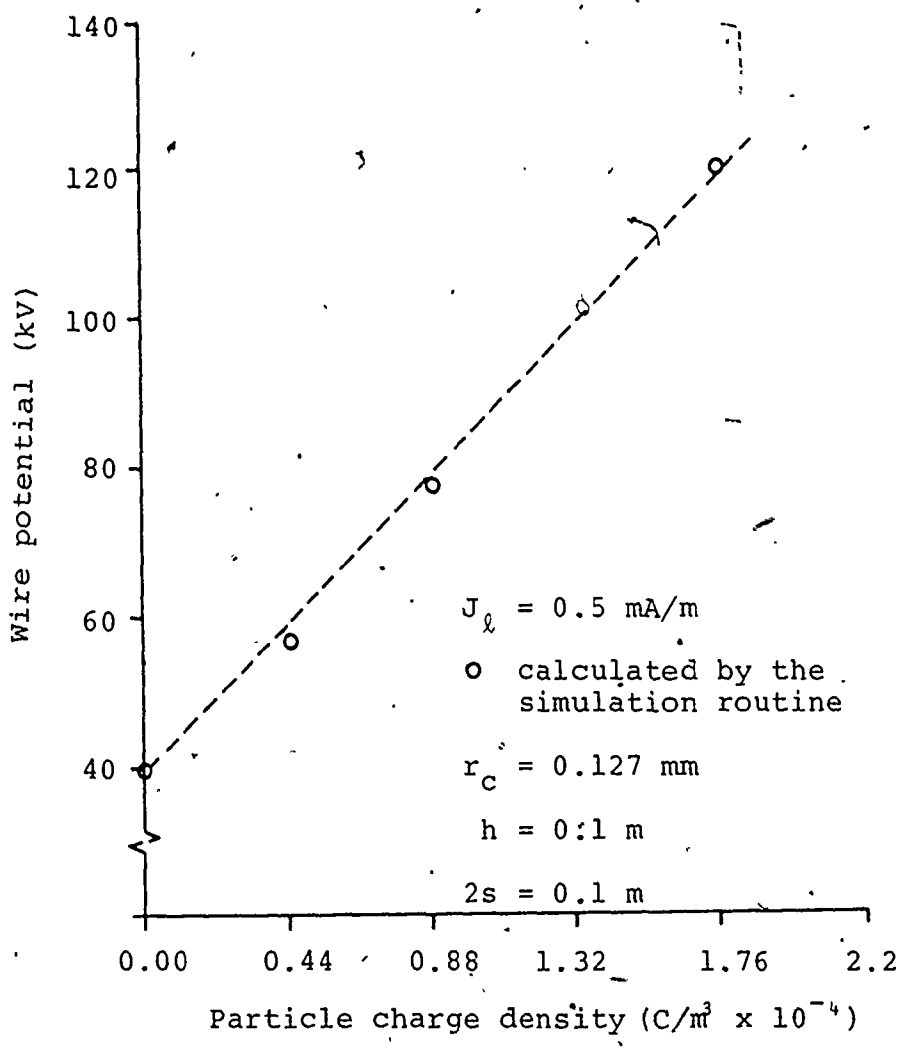

Figure 9.3. Corona wire potential for variable particle charge density under fixed linear corona current

i) A uniform particle space charge density is held constant at 0.44×10^{-4} C/m^3 and the current J_ℓ is reduced to one tenth its value compared to the clean air condition (J_ℓ = 0.01 mA/m).

ii) The linear corona current was held at 0.01 mA/m and the particle charge density ρ_p' is reduced by one tenth to 0.44×10^{-5} C/m^3.

For the first case, it was found that the potential required to maintain a current of 0.01 mA/m was 36.8, 119 and 253 kV for spacings of 0.1, 0.2 and 0.3 m respectively. Again the last two values of potential represent unrealistic operation presumably because the assumed value of particle charge density is too high.

For the second case, more realistic operating conditions were achieved since the wire potentials were 15, 31 and 54 kV for the increased order of duct spacing.

Once more it can be observed that an increase in the duct spacing, corresponds to an increase in the magnitude of the electric field at the collecting wall. This is shown in figure 9.4. When the duct spacing was increased by a factor of 3, the electric field, at the plate at a point directly below the corona wire, was enhanced by a factor of 2. This is even a larger enhancement than that

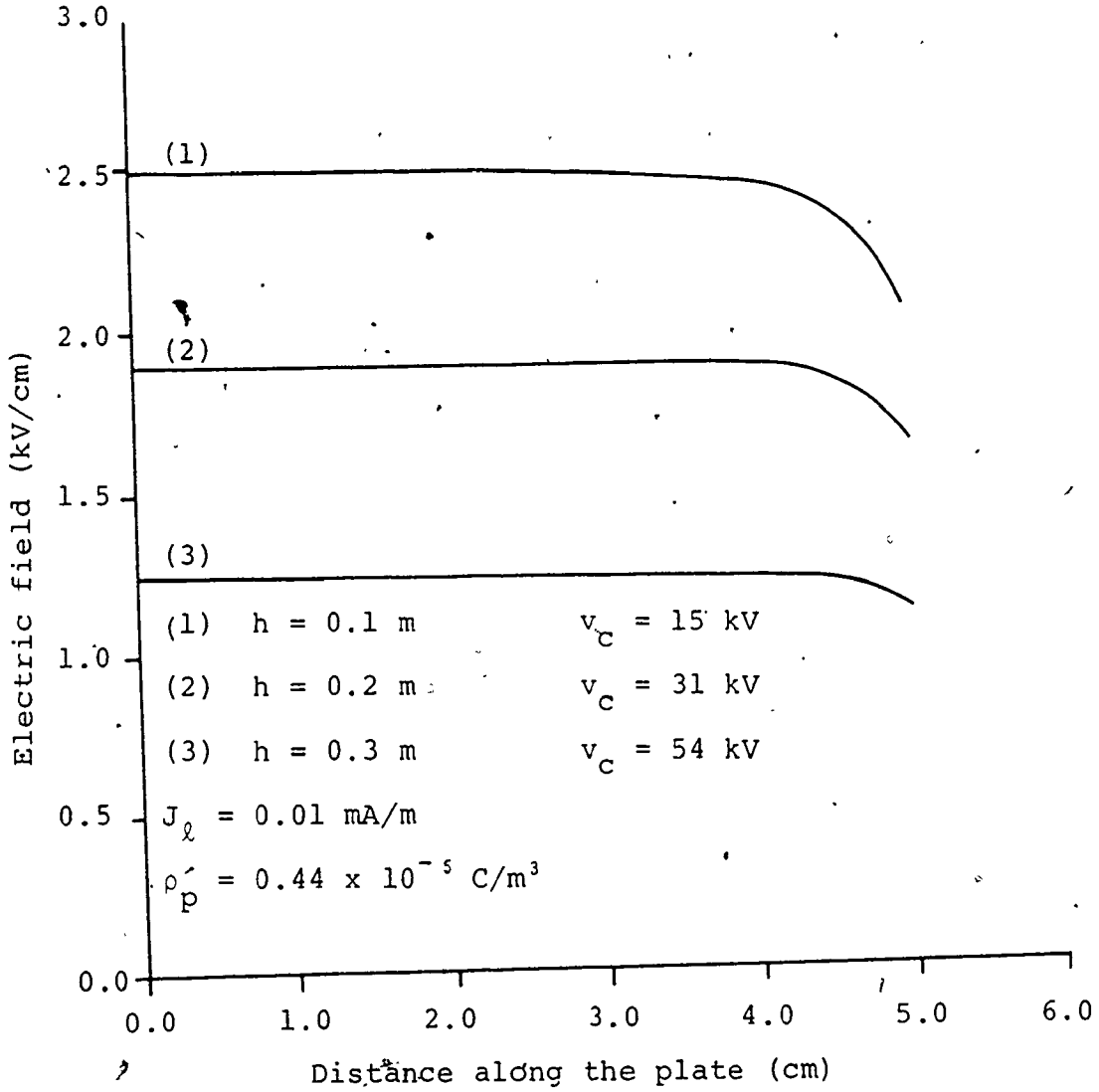

Figure 9.4. Electric field distribution along the plate under dust loading conditions

which was observed for clean air (1.7) for the same ratio of duct spacing but for only one tenth the amount of current. This extra enhancement is due to the presence of the particle space charge.

Some of the significant data associated with the two particle space charge densities investigated, at constant linear corona current of 0.01 mA/m, are given in table 9.1.

It is of interest to observe that the field enhancement factor (E_p/E_{av}) increases as the duct spacing increases. When the particle charge density was increased ten times while maintaining the value of J_ℓ constant, a significant increase in the field enhancement factor was observed for all the spacings as compared to the lower value of particle charge density. This illustrates the contribution of particle space charge to the electric field enhancement at the collecting walls. It should be noted here that the last two values in table 9.1 represent unrealistic operation, since the electric fields at the plate are higher than 6 kV/cm, in which case breakdown would probably occur.

For the case where $\rho_p' = 0.44 \times 10^{-5}$ C/m^3, increasing the duct spacing by a factor of 3, caused an increase of 20% and 100% in the average and plate fields respectively. This corresponds to an increase of 140% in the migration

Table 9.1 Field enhancement factor with corona quenching at constant current = 0.01 mA/m as a function of duct spacing

Particle Charge Density (C/m^3)	Wire to Wire Spacing (m)	Wire to Plate Spacing (m)	Voltage (kV)	E_{av} (kV/cm)	E_p (kV/cm)	Ratio E_p/E_{av}
	0.1	0.1	15	1.5	1.24	0.8
0.44×10^{-5}	0.1	0.2	31	1.5	1.9	1.27
	0.1	0.3	54	1.8	2.51	1.39
	0.1	0.1	36.8	3.6	5.5	1.5
0.44×10^{-4}	0.1	0.2	119	5.9	10.7*	1.8
	0.1	0.3	253	8.3	15.6*	1.9

*indicates breakdown

velocity, if one assumes that ω is proportional to $(E_{av} E_p)$. This percentage increase in ω is large than that obtained for clean air conditions (135%), particularly when considering that the linear current density J_ℓ and applied voltage V_c for this case were only 10% and 60%, respectively, of those values used in clean air.

It seems, from table 9.1, that an appropriate maximum particle space charge density lies in the mid-range of 0.44×10^{-4} and 0.44×10^{-5} C/m^3. This result is confirmed by the recent work of Lindau and Matts [73]. In their work they showed that if the particle charge density is less than 10^{-5} C/m^3, in conventional duct spacings, then the effects in terms of corona quenching and high collecting plate field strength (causing breakdown) are limited. For larger values of particle space charge density, these effects become more significant. They also observed that increasing the duct spacing enhances these effects.

Finally, from the above analysis, it can be seen that the corona quenching model is a convenient method to evaluate the electrical effects caused by changing experimental parameters such as, duct width, wire to wire spacing, wire radius, linear current density and particle space charge.

CHAPTER TEN

CONCLUSIONS

This chapter elaborates on the main conclusions, recommendations and suggestions for future studies. These are summarized as follows:

A. Preliminary Study

Initially, a study was performed on the major analytical solutions and numerical methods [22, 23, 24, 25, 33, 36 and 41], suggested by other researchers, for solving Poisson's equation and the current continuity equation which govern the electrical conditions in the duct-type geometry. The following conclusions were made from this study:

i. The V-I characteristics for duct-type precipitators may be evaluated using P. Cooperman's and G. Cooperman's suggested relations, bearing in mind that they are both approximate solutions. These relations can give good agreement to experimental measurements under certain circumstances.

ii. The use of conformal transformations is another method by which the general shape of the V-I characteristics may be obtained. But this method is not recommended for evaluating electrical parameters, such as

potential, electric field and charge density, in the inter-electrode gap because of it's relatively poor accuracy.

iii. The finite difference technique is not sufficiently accurate particularly when using a grid where all the elements are of the same size. The technique could probably be enhanced by using a successive graded grid, but this would require considerable effort for setting-up the problem as well as increase the computational time.

iv. The finite element method appears to be the most accurate and reliable technique currently available in the literature, but still further improvement is desirable in the method of evaluation of the charge density distribution. The draw-back of this technique is that it requires excess computational time as compared to the other methods mentioned above.

B. Cylindrical geometry

The charge simulation technique was successfully adapted to model the electrical conditions that exist in cylindrical precipitators. For this geometry, three models were developed.

The first model represented the electrostatic case, where no space charge exists. The results of the model were in good agreement to the voltage and field distributions as evaluated by the analytical solution of Laplace's equation for this geometry.

The second model represented corona in clean air. These results also showed good agreement to the voltage, field and charge density distributions as evaluated by the analytical solution of Poisson's equation for this geometry.

The third model predicted the potential, electric field, ionic and particle space charge density distributions in the presence of dust loading (corona quenching). This model showed good agreement to the results of the suggested modified solution of Poisson's equation in the presence of uniform particle space charge.

The modified solution mentioned above differs from that of Pauthenier's classical solution [52] in that it assumes that the inter-electrode gap is divided into two zones. The first being the turbulent zone, which constitutes the main volume of the precipitator. In this zone the corona current is essentially carried only by the ions while the charged particles contribute a net zero component in the field direction. In the second zone,

which is adjacent to the collecting walls and is referred to as the collecting zone, both the ion and particle space charge act as current carriers. A further modification was introduced with the intent of accounting for a uniform particle space charge density as well as allowing for fractional charging of the particles to their Pauthenier limit, a situation of particular significance in the case of corona quenching.

C. Duct-type preciptators in clean air

The charge simulation technique was successfully extended to model the electrostatic and corona conditions under clean air conditions for the duct-type precipitator geometry.

The electrostatic model gave very good agreement to both Cooperman's [61] and Böhm's [62] infinite series for the voltage and electric field distributions respectively.

The results of the corona model, showed good agreement to the experimental data of Penney and Matick [31], Felici [30] and Tassicker [29]. The results of figure 5.9 also showed clearly that the commonly used assumption that the space charge affects only the magnitude but not the direction of the electric field is incorrect in general.

In the corona model, the corona discharge is assumed uniform along the high voltage electrode, thus the problem is reduced to two dimensions. This assumption is approximately true for positive corona. Whereas for negative corona, the corona takes the form of localized tufts of random distribution along the electrode surface. The fact that these emitting spots are in continous motion along the surface, tends to make the corona discharge uniform. Hence, the assumption is also approximately true for negative corona. This is even more true for the corona quenching case, where the charging time constant of the particles may reach a few seconds.

To simulate more accurately the case of negative corona, a three dimensional model would be required. In doing so the infinite line charges are to be replaced by finite line charges and possibly point charges. As a result, the number of simulating charges would tremendously increase and a super computer may be required. Considering these facts and for the reasons presented above, the use of a two dimensional model is sufficient.

The sensitivity analysis performed for the corona model showed that for an error of 10% in the value of linear corona current density, the corresponding error in the estimated wire potential V_C and the plate electric field E_p is 4% and 4.6% respectively. Similarly an error

of about +20% in the value of ion mobility, leads to errors of -8% and -10% in the estimated value of wire potential and plate electric field respectively. This part of the study also confirmed the validity of the assumption that the corona wire may be considered an ion emitting source and that the thickness of the ionization zone may be neglected.

The drawback of the corona model is that it requires much computational time. The author was unable to compare the C.P.U time required for running the charge simulation model to that required for running the finite element model developed by Davis and Hoburg [41], because their computer coding was unavailable. Nevertheless, the distinct advantages of the charge simulation model over the finite element model are:

i. Both Poisson's equation and the current continuity equation are solved simultaneously rather than being solved alternatively using an iterative process.

ii. The charge simulation method does not require the pre-construction of a fixed grid, rather the grid is constructed as the calculations proceed.

iii. The grid constructed by the charge simulation technique represents a plot of the lines of field and equipotential contours.

iv. The charge simulation technique does not require any initial guesses.

D. Wide duct precipitators

The literature survey conducted on wide duct precipitators revealed that all the studies that were performed on wide duct precipitators were mainly concerned with the performance of such precipitators and little attention has been given to the electrical conditions that exist in such precipitators.

Thus an experimental apparatus was constructed to measure the electric field and current density distributions at the collecting plate of a variable duct spacing laboratory scale electrostatic precipitator.

The experimental results showed that for a finite array of corona wires operated at the same potential, the corona current emanating from each wire is different. The outer wires had the highest linear corona current density, while the central wire had the lowest. Similarly, the corona onset voltage for such an array of wires also

varies, with the outer wires exhibiting corona at a lower potential than the central ones. These results confirm the observations of Lawless and Sparks [79].

In addition the experimental results showed good agreement with the results of the charge simulation model and further confirms the validity of the developed model.

The study conducted to investigate the electrical conditions of wide duct precipitators as compared to those of standard duct spacing yielded the following results:

i. For constant linear corona current, if the duct spacing is increased while keeping the wire to wire spacing constant, the electric field enhancement factor (E_p/E_{av}) is also increased. This is also accompanied by an increase in the magnitude of both the plate field (E_p) and the average field (E_{av}), thus persumably increasing the collection forces.

ii. For constant linear corona current, if the duct spacing is increased while keeping the ratio (h/2s) constant, there is practically no change in the electric field enhancement factor. There is also no increase in the magnitude of both the plate field and the average field. Thus one would not expect any enhancement in the precipitator performance. However,

this approach may result in construction and operational cost reductions.

iii. For constant applied voltage, increasing the duct spacing while keeping the wire to wire spacing constant, resulted in the decrease of the electric field enhancement factor, the plate field and the average field. Thus this approach is not recommended.

It was interesting to observe in this study that for all the geometries considered and for all the operating conditions, the point of minimum electric field along a line extending from wire to plate was always approximately 2 cm away from the corona wire.

E. Corona quenching in duct-type precipitators

The corona in clean air model, for duct-type precipitators, was modified to account for a uniform particle space charge density. The same assumptions used for the corona quenching model in the cylindrical geometry were applied to the duct geometry.

Results of the corona quenching model indicated that for a constant linear corona current and constant uniform particle space charge, the increase of the duct spacing is accompanied by an increase in the electric field

enhancement factor. This increase is significantly larger than that observed under clean air conditions. This indicates a strong contribution of particle space charge to the enhancement of the electric field at the precipitator walls. It is suggested that an appropriate maximum particle space charge density lies in the mid-range of 0.44×10^{-4} and 0.44×10^{-5} C/m^3.

The corona quenching model was shown to be a convenient method for evaluating the electrical effects caused by changing experimental parameters, whether they be changes in the physical dimensions or changes in the operating conditions.

F. General

The charge simulation models presented here eliminate the cost and time needed in constructing and experimenting with proto-type models to predict the electrical characteristics of electrostatic precipitators in clean air as well as under dust loading conditions.

Finally, the successful use of the charge simulation technique to predict an unknown space charge distribution is of significant importance as it opens the door to investigate similar characteristics of other geometries, such as those used in high voltage switchgear, transmission

lines and terminations.

Appendix 1

Classification of Computer Models Based on the Charge Simulation Technique

The Fortran coding for the programs developed based on the charge simulation technique, is accessible by attaching to the User File Directory (UFD) entitled "ELECTROSTATICS" and later to the sub-UFD entitled "PRECIPITATORS" on the Prime 400 mainframe available at the Seam Laboratory, Faculty of Engineering Science, The University of Western Ontario.

The files available in this sub-UFD are listed below:

1. HELP: a help file that contains instructions for running the files that follow.

2. CYL-STAT: used for evaluating the electrical conditions that exist in cylindrical precipitators under Laplacian fields (electrostatic case).

3. CYL-COR: used for evaluating the electrical conditions in cylindrical precipitators in the presence of corona discharge in clean air.

4. CYL-COR-QU: used for evaluating the electrical conditions in cylindrical precipitators in the presence of corona quenching due to dust loading.

5. DUCT-STAT: used for evaluating the electrical conditions that exist in duct-type precipitators under Laplacian fields.

6. DUCT-COR: used for evaluating the electrical conditions in duct-type precipitators in the presence of corona discharge in clean air.

7. DUCT-COR-QU: used for evaluating the electrical conditions in duct-type precipitators in the presence of corona quenching due to dust loading.

Appendix 2

Finite Element and Characteristics Methods

Finite Element Method

Use of the finite element method to determine the potential distribution V, for a known charge density ρ is based upon a principle of variational calculus [48], whereby the solution of Poisson's equation is equivalent to minimizing the function.

$$F(V) = 0.5 \int_{vol} (\varepsilon_o |\nabla V|^2 - 2\rho V)\, dVol \qquad (A.2.1)$$

The variation of V over each element is approximated by a linear interpolation function.

$$V(x,y) = a_0 + a_1 x + a_2 y \qquad (A.2.2)$$

with a resultant constant electric field within any particular element.

$$E = -a_1 \hat{x} - a_2 \hat{y} \qquad (A.2.3)$$

Representation of the variation of V over each element in terms of the nodal values of V and imposition of the minimization condition $\partial F(V)/\partial V = 0$ for the entire set of elements leads to a set of simultaneous equations for values of V at the nodes.

Method of Characteristics

The method of characteristics is based on a technique whereby the partial differential equation governing the evolution of charge density becomes an ordinary differential along specific characteristic space-time trajectories

In the inter-electrode region, the current continuity equation, written in terms of charge density ρ and current density J, requires:

$$\nabla . J = \nabla . \rho b E = 0 \qquad (A.2.4)$$

Also the electric field is related to the charge density by Gauss's law [49].

$$\nabla . E = \frac{\rho}{\varepsilon_o} \qquad (A.2.5)$$

Combining equations (A.2.4) and (A.2.5) leads to a partial differential equation governing the evolution of charge density as follows.

$$E . \nabla \rho = - \frac{\rho^2}{\varepsilon_o} \qquad (A.2.6)$$

Along the space-time trajectory defined by $dr/dt = bE$, the left-hand side of the above equation represents the convective derivative of charge density. This equation (A.2.6) is reduced to an ordinary differential equation.

$$\frac{d\rho}{dt} = -\frac{b\rho^2}{\varepsilon_0} \qquad \text{(A.2.7)}$$

along the characteristic line

$$\frac{dr}{dt} = bE \qquad \text{(A.2.8)}$$

The solution of equation (A.2.7) yields the following equation.

$$\rho = \left[\frac{1}{\rho_0} + \frac{bt}{E}\right]^{-1} \qquad \text{(A.2.9)}$$

where ρ_0 is the charge density at the starting point of the characteristic line.

The characteristic line is presented as a set of straight line increments drawn across individual triangles of the finite element grid. Since the electric field within each element is constant, then the time dt required to traverse the triangle boundaries dr along the characteristic line may be evaluated using equation (A.2.8). Then the value of t is used to evaluate the charge density ρ from equation (A.2.9).

Appendix 3

Solution of Poisson's Equation and the Current Continuity Equation for a Cylindrical Geometry

When using cylindrical co-ordinates the divergence of a vector $\bar{A}$ is given by equation (A.3.1), while the Laplacian of a function f is given by equation (A.3.2).

$$\nabla \cdot \bar{A} = \frac{1}{r}\frac{\partial}{\partial r}(rA_r) + \frac{1}{r}\frac{\partial A_\phi}{\partial \phi} + \frac{\partial A_z}{\partial z} \qquad (A.3.1)$$

$$\nabla^2 f = \frac{1}{r}\frac{\partial}{\partial r}\left(r\frac{\partial f}{\partial r}\right) + \frac{1}{r^2}\frac{\partial^2 f}{\partial \phi^2} + \frac{\partial^2 f}{\partial z^2} \qquad (A.3.2)$$

Applying the above two equations to Poisson's equation and the current continuity equation respectively, for an infinitely long coaxial cylindrical system, yields.

$$-\frac{1}{r}\frac{d}{dr}\left(r\frac{dV}{dr}\right) = \frac{\rho}{\varepsilon_o} \qquad (A.3.3)$$

$$-\frac{1}{r}\frac{d}{dr}\left(r\rho\frac{dV}{dr}\right) = 0 \qquad (A.3.4)$$

From equation (A.3.4) it is clear that the term in between brackets is a constant. Since at $r = r_c$, the electric field is equal to E and the charge density is equal to ρ_e, then this constant is equal to $r_c \rho_e E_o$. From the previous analysis, it can be concluded that

$$\frac{dV}{dr} = \frac{r_c \rho_e E_o}{r \rho} \qquad (A.3.5)$$

When substituting equation (A.3.5) in equation (A.3.3), the following equation for the charge density distribution is derived.

$$\rho(r) = \frac{\sqrt{E_o \rho_e \varepsilon_o r_c}}{f_1(r)} \qquad (A.3.6)$$

where $f_1(r) = \sqrt{r^2 + K_2^2 - r_c^2}$ (A.3.7)

and $K_2 = \sqrt{\frac{E_o \varepsilon_o r_c}{\rho_e}}$ (A.3.8)

The potential at any radial distance (r) is given as

$$V(r) = V_c - \int_{r_c}^{r} \left(\frac{dv}{dr}\right) . dr \qquad (A.3.9)$$

Substituting equations (A.3.5) and (A.3.6) in equation (A.3.9) and solving, yields the following equation for the wire potential V_c.

$$V_c = K_1 \{ f_1(r_o) - K_2 + K_3 [\ln(r_c/r_o) + \ln(K_3 + K_2) - \ln(K_3 + f_1(r_o))] \} \qquad (A.3.10)$$

where $K_1 = \sqrt{\frac{E_o \rho_e r_c}{\varepsilon_o}}$

and $K_3 = \sqrt{K_2^2 - r_c^2}$

Appendix 4

Flow Chart of the Corona Model for

Cylindrical Precipitators in Clean Air

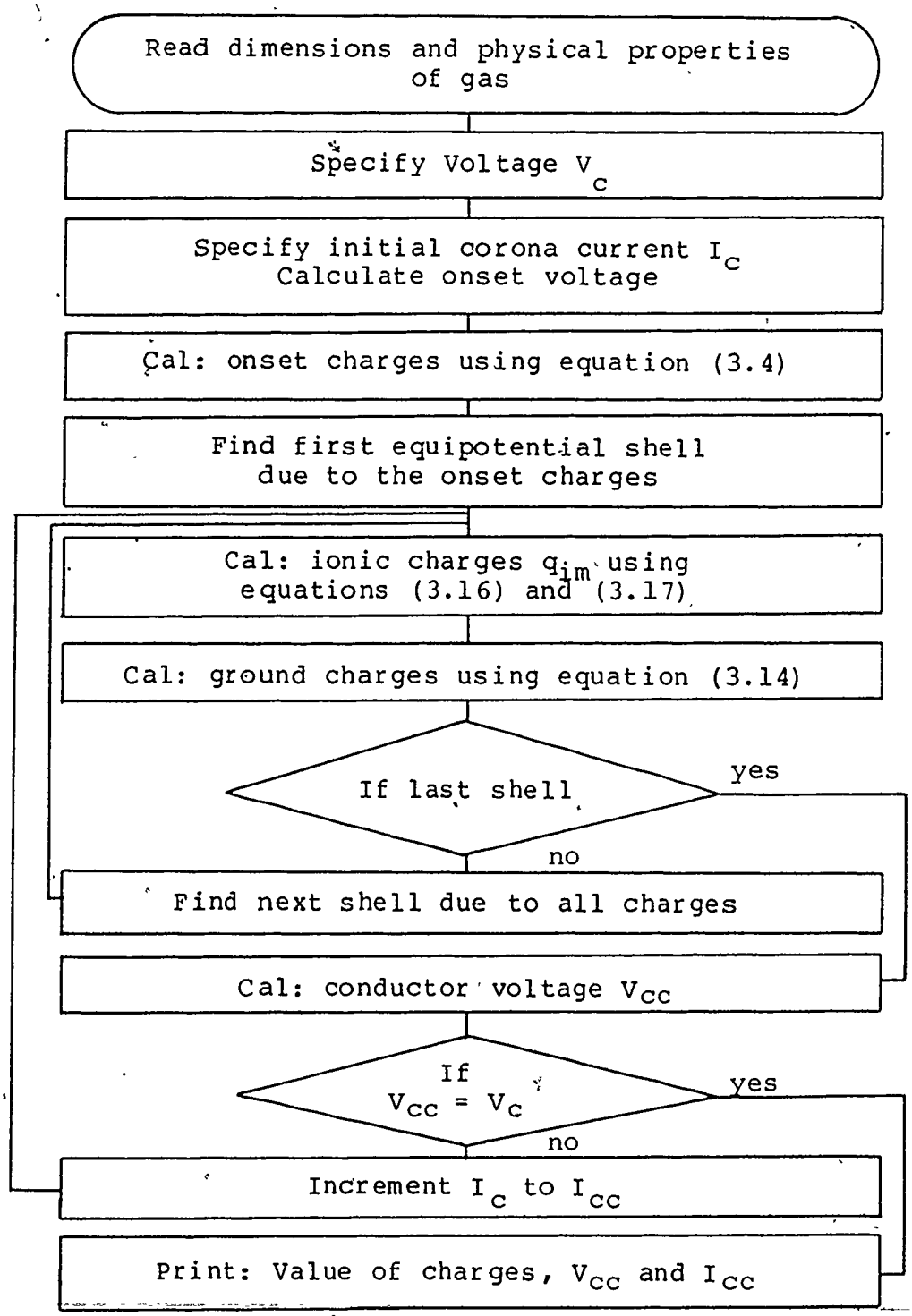

Appendix 5

Measurement of Electric Field Using a Biased Current Probe

As shown in figure A.5.1 the probe is connected in series with an ammeter and a variable d.c voltage bias source. The ammeter used had to be operated in a floating mode when the bias voltage was applied.

When determing current density, the bias voltage is set to zero, the probe then causes neither mechanical nor electrical perturbation. The current density is simply evaluated using equation (A.5.1).

$$J = \frac{I_o}{(\pi/4)D_i^2} \qquad (A.5.1)$$

With negative bias applied to the probe, while positive ions flow into it, the probe current I is larger than I_o. With positive bias, the curent decreases. This is plotted in the manner of figure A.5.2, as I/I_o against V_b. This typical characteristic always shows a straight region about the origin. Tassicker [78] has shown that the slope of this straight-line region is proportional to the ambient electric field E_o.

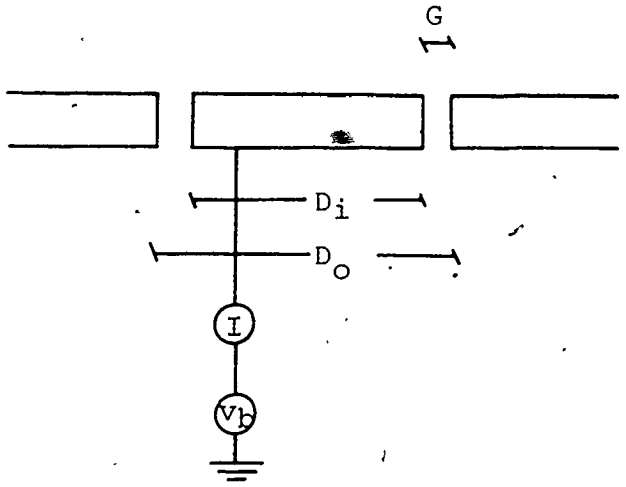

Figure A.5.1. Microarea boundary electrode with provision for bias

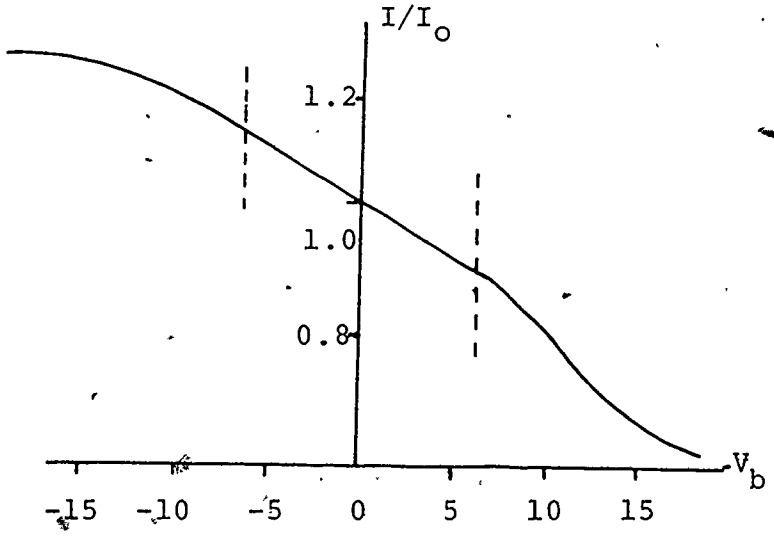

Figure A.5.2. Generalized probe characteristic

Consider the following two cases:

i) The bias voltage is equal to zero and the electric field E_o, in the presence of space charge, is uniform just at the probe and the area surrounding it. This case is presented by figure A.5.3.a, from which the electric flux at the probe surface may be calculated as.

$$\psi_o = AE_o\varepsilon_o \qquad (A.5.2)$$

where A is the surface area of the probe.

ii) In the second case, consider that the electric field E_o is not present and the probe is biased with a negative voltage, as shown by figure A.5.3.b. In this case the flux arriving at the probe surface may be calculated as.

$$\psi_1 = \int_{\text{surface}} D.dA = Q = C_oV_b \qquad (A.5.3)$$

where C_o represents the capacitance between the top surfaces of the probe and the surrounding plate. Here the capacitance of the gap is neglected.

Superposition of the above two cases is acceptable provided, the distribution of the space charges in the former is not altered by the application of the latter field and also if the field in the region of the probe is locally Laplacian.

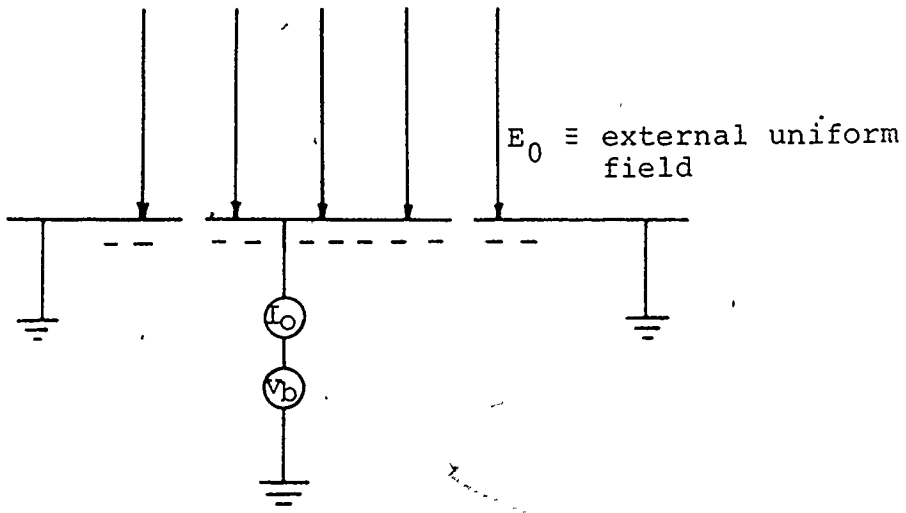

(a) $V_b = 0$

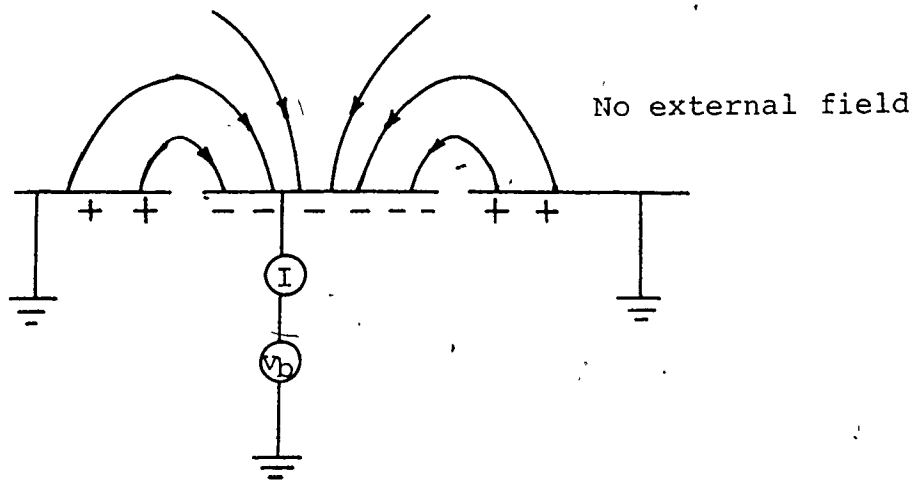

(b) V_b = negative bias

Figure A.5.3. Lines of field at probe surface with and without bias voltage

By superposition the total current entering the probe may be given as.

$$I = b\rho\frac{\psi}{\varepsilon_o} \qquad \text{(A.5.4)}$$

where the total flux ψ is equal to

$$\psi = \psi_o + \psi_1 \qquad \text{(A.5.5)}$$

By dividing both sides of equation (A.5.5) by ψ_o, the following equation is attained.

$$\frac{I}{I_o} = 1 + \frac{C_o V_b}{A\varepsilon_o E_o} \qquad \text{(A.5.6)}$$

Equation (A.5.6) gives the straight-line relationship shown by figure A.5.2. Since for a given probe, $C_o/A\varepsilon_o$ is a fixed geometrical constant, the ambient electric field may be determined immediately.

The value of C_o is evaluated using equation (A.5.7).

$$C_o = 2D_i\varepsilon_o\{1.079 + 0.5\ln(1 + D_i/4G)\} \qquad \text{(A.5.7)}$$

REFERENCES

[1] G.W. Penney, "Electrostatic Precipitators of High-Resistivity Dust", AIEE Tech. paper 51-201, 1951.

[2] G.S.P. Castle, "Mechanisms Involved in Fly Ash Precipitation in the Presence of Conditioning Agents - A Review", IEEE Trans. on Industry Applications, Vol. IA-16, No. 2, March/April 1980, pp. 297-302.

[3] M.B. Awad and G.S.P. Castle, "Corona Quenching in Electrostatic Precipitators", Industry Applications Society Conference Record, 1974, pp. 945-954.

[4] C.F. Gallo, "Corona - A Brief Status Report", IEEE Trans. on Industry Applications, Vol. IA-13, No. 6, Nov./Dec. 1977, pp. 550-557.

[5] M. Pauthenier and M. Moreau-Hanot, "La Charge des Particules Spheriques dans Un Champ Ionise", J. Physique et Radium , 3, 1932, pp. 590-613.

[6] A.D. Moore (Editor), Electrostatics and it's Applications, Wiley Interscience, 1973, pp. 197.

[7] J.D. Cobine, Gaseous Conductors, Dover Publications, New York, N.Y., 1958.

[8] L.B. Loeb, Electrical Coronas, Their Basic Physical Mechanisms, University of California Press, Berkeley, 1965.

[9] E. Nasser, Fundamentals of Gaseous Ionization and Plasma Electronics, Wiley Interscience, New York, 1971.

[10] W. Strauss (Editor), Air Pollution Control, Wiley Interscience, New York, Part I, 1971, pp. 234-238.

[11] N.H. Malik and A.H. Qureshi, "Breakdown Mechanisms in Sulphur-Hexafluoride", IEEE Trans. on Electrical Insulation, Vol. EI-13, 1978, pp. 135-145.

[12] M.B. Awad and G.S.P. Castle, " Ozone Generation in an Electrostatic Precipitator With a Heated Corona Wire", Journal of Air Pollution Control Association, Vol. 25, No. 4, April 1975, pp. 369-374.

[13] F.W. Peek, Dielectric Phenomena in High-Volatge Engineering, McGraw-Hill, 1929, Chapter 4.

[14] A.D. Moore, op. cit., pp. 200-201.

[15] H.J. Lowe and D.H. Lucas, "The Physics of Electrostatic Precipitation", British Journal of Applied Physics, Supplement No. 2, 1953, pp. S40-S47.

[16] M. Robinson, "Movement of Air in the Electric Wind of the Corona Discharge", AIEE Trans., Part 1, Vol. 80, 1961, pp. 143-150.

[17] H.J. White, Industrial Electrostatic Precipitation, Addison-Wesley Publishing, 1963, Chapter 6.

[18] M. Robinson, "A Modified Deutsch Efficiency Equation for Electrostatic Precipitation", Journal of Atmospheric Environment, Vol. 1, 1967, pp. 193-204.

[19] G.W. Penney, " Some Problems in the Application of the Deutsch Equation to Industrial Electrostatic Precipitaion", Journal of Air Pollution Control Association, Vol. 19, No. 8, Aug. 1969, pp. 596-600.

[20] H. Singer, H. Steinbigler and P. Weiss, "A Charge Simulation Method for the Calculation of High Voltage Fields", IEEE Trans. PAS, Vol. PAS-93, Sept./Oct. 1974, pp. 1660-1668.

[21] A.A. Elmoursi and N.H. Malik, "Field Uniformity of a High Voltage Test Electrode System", IEEE Trans. on Electrical Insulation, Vol. EI-18 (1), Feb. 1983, pp. 89-92.

[22] P. Cooperman, "A Theory for Space-Charge-Limited Currents With Application to Electrical Precipitation", AIEE Trans., part 1, Vol. 79, 1960, pp. 47-50.

[23] P. Cooperman, "Dust Space Charge in Electrical Precipitaion", AIEE Trans. on Communications and Electronics, Vol. 82, 1963, pp. 324-326.

[24] G. Cooperman, "A New Current-Voltage Relation for Duct Precipitators Valid for Low and High Current Densities", IEEE Trans. on Industry Applications, Vol. IA-17, 1981, pp. 236-239.

[25] S. Sekar and H. Stomberg, "On the Prediction of Current-Voltage Characteristics for Wide-Plate Precipitators", Journal of Electrostatics, Vol. 10, 1981, pp. 35-43.

[26] W. Strauss (Editor), op. cit., pp. 245.

[27] V.I. Vasyaev and I.P. Vereshchagin, "Method of Calculating the Field Strength During Corona Discharge", Electric Tech. U.S.S.R, Vol. 2, 1971,

pp. 91-102.

[28] M. Robinson and J. Shepherd, "Preliminary Report on Wide Plate Spacing", Research and Development, Research-Cottrell, 1977 (in-house report).

[29] O.J. Tassicker, "Aspects of Forces on Charged Particles in Electrostatic Precipitators", Ph.D. Thesis, Wollongong University College, University of New South Wales, July 1972, pp. 159-161.

[30] N.J. Felici, "Recent Advances in the Analysis of D.C. Ionized Electric Fields", Direct Current, Vol. 8, No. 9, 1963.

[31] G.W. Penney and R.E. Matick, "Potentials in D.C. Corona Fields", AIEE Trans., Vol. 79, May 1960, pp. 91-99.

[32] G. Leutart and B. Bohlen, "The Spatial Trend of Electric Field Strength and Space Charge Density in Plate-Type Electrostatic Precipitators", Staub-Reinhalt. Luft, Vol. 32, No. 7, July 1972, pp. 27-33.

[33] J.R. McDonald and L.E. Sparks, "A Mathematical Model for Calculating Electrical Conditions in Wire-Duct Electrostatic Precipitation Devices", Journal of Applied Physics, Vol. 48, No. 6, June 1977, pp. 2231-2243.

[34] P.A. Lawless and L.E. Sparks, "A Mathematical Model for Calculating Effects of Back Corona in Wire-Duct Electrostatic Precipitators", Journal of Applied

Physics, Vol. 51, No. 1, Jan. 1980, pp. 242-256.

[35] G.D. Smith, Numerical Solution of Partial Differential Equations, Oxford University Press, 1971.

[36] G.A. Kallio and D.E. Stock, "Numerical Computation of the Electrical Conditions in a Wire-Plate Electrostatic Precipitator Using the Finite Element Technique", The Fifth Symposium on the Transfer and Utilization of Particulate Control Technology, Kansas City, Montana, Aug. 27-30, 1984.

[37] A.W. Baird, "The Use of Graded Nets in Computer Modeling of Corotron Fields", IEEE Trans. on Industry Applications, Vol. IA-12, No. 5, Sept./Oct. 1976, pp. 524-526.

[38] J.R. McDonald, "A Mathematical Model of Electrostatic Precipitation", Vol. I, U.S. Enviromental Protection Agency Report No. EPA-600/7-78-111a.

[39] Discussion at the Fifth Symposium on the Transfer and Utilization of Particulate Control Technology, Kansas City, Missouri, Aug. 27-30, 1984.

[40] G.S.P. Castle, private communications, 1982.

[41] J.L. Davis and J.F. Hoburg, "Wire-Duct Precipitator Field and Charge Computation Using Finite Element and Characteristics Methods", Journal of Electrostatics, Vol. 14, 1983, pp. 187-199.

[42] J.L. Davis, private communications, Oct. 3, 1984.

[43] M.S. Abou-Seada and E. Nasser, "Digital Computer Calculation of the Electrical Potential and Field of a

Rod Gap", Proc. IEEE, Vol. 56, 1967, pp. 813-820.

[44] C.F. Gerald, Applied Numerical Analysis, Second Edition, Addison-Wesley Publishing Company, 1978, Chapter 2.

[45] M. Abdel Salam, A. Zeitoun and M. El-Ragheb, "Charge Simulation Technique for Calculating the Field due to Ionic Space Charge", Industry Applications Society Conference Record, 1976, pp. 654-659.

[46] M. Abdel Salam and A.A. Ibrahim, "Digital Calculations of Electric Fields in the Vicinity of Protrusions from H.V. Condúctors", IEEE PES Winter meeting, New York, N.Y., Jan. 30-Feb. 4, 1977, paper No. A 77 131-6.

[47] M.N. Horenstein, "Computation of Corona Space Charge and V-I Chararcteristics Using Equipotential Charge Shells", Industry Applications Society Conference Record, 1980, pp. 1081- 1086.

[48] O.C. Zienkiewiez, The Finite Element Method in Engineering Science, McGraw-Hill, 1971, pp. 26-29.

[49] M. Zahn, Electromagnetic Field Theory: a problem solving approach, John Wiley and Sons, 1979, pp. 72-83.

[50] M. Pauthenier and M. Moreau-Hanot, "Ettouffement de la Decharge Couronne-en Millieu Trouble", J. Physique et Radium, 6, 1953, pp. 257-262.

[51] N.H. Malik, private communications, Feb. 1982.

[52] A. Yializis, E. Kuffel and P.H. Alexander, "An Optimized Charge Simulation Method for the Calculation

of High Voltage Fields", IEEE PES Winter Meeting, New York, N.Y., Jan. 29 - Feb. 3, 1978, paper No. F 78 179-4.

[53] M.R. Iravani and M.R. Raghuveer, "Accurate Field Solution in the Entire Interelectrode Space of a Rod-Plane Gap Using Optimized Charge Simulation", IEEE Trans. on Electrical Insulation, Vol. EI-17, No. 4, Aug. 1982, pp. 333-337.

[54] G. Gela, "Computation of Ionized Fields Associated with Unipolar D.C. Transmission Systems", Ph.D. thesis, Department of Electrical Engineering, University of Toronto, April 1980.

[55] F.B. Irwin and I.I. Inculet, "A Mathematical Analysis of the Glow and Dark Space Regions in Positive Corona", Industry Applications Society Conference Record, 1984, pp. 992-996.

[56] M.P. Sarma and W. Janischewskyj, "Analysis of Corona Losses on D.C. Transmission Lines: I - Unipolar Lines", IEEE Trans. on PAS, Vol. PAS-88, No. 5, May 1969, pp. 718-731.

[57] M. Khalifa and M. Abdel-Salam, "Improved Method for Calculating D.C. Corona Losses", IEEE PES summer meeting, July 15-20, 1973, paper No. T 73 410-8.

[58] A.D. Moore, op. cit., pp. 191-193.

[59] W. Strauss (Editor), op. cit., pp. 309-311.

[60] C.F. Gerald, op. cit., pp. 266-274.

[61] P. Cooperman, Report No. 46, Research Cottrell Inc.,

Bound Brook, NJ, 1952.

[62] J. Böhm, "Back Discharge in Electrostatic Gas Cleaning", Staub-Reinhalt. Luft, Vol. 30, No. 3, March 1970.

[63] J. Böhm, Electrostatic Precipitators, Elsevier Scientific Publishing Company, 1982, Chapter 2.

[64] M.B. Awad, "Mechanism of Corona Quenching and Sparkover Phenomena in Electrostatic Precipitators", Ph.D. thesis, The University of Western Ontario, June 1975.

[65] A.A. Elmoursi and G.S.P. Castle, "The Analysis of Corona Quenching in Cylindrical Precipitators Using Charge Simulation", Industry Applications Society Conference Record, 1983, pp. 974-981.

[66] J.R.G. Pude, J.F. Hughes and P.F. Coventry, "A Study of Electrostatic Precipitation Processes Calculation of Electric Fields due to Single Unipolar Source", Journal of Electrostatics, Vol. 14, 1983, pp. 241-254.

[67] P.A. Lawless and L.E. Sparks, "Measurment of Ion mobilities in Air and Sulfur Dioxide Air Mixtures as a Function of Temperature", Atmospheric Environment, Vol. 14, 1980, pp. 481-483.

[68] T. Misaka, K. Sugimoto, H. Yamada, "Electric Field Strength and Collection Efficiency of Electrostatic Precipitator having Wide Collecting Plate Pitches", CSIRO Conference on Electrostatic Precipitation, Leura, Aug. 23-24, 1978, paper No. 11.

[69] D.O. Heinrich, "Review and Some Practical Aspects of Wide Duct Spacing", Proceedings of the First International Conference on Electrostatic Precipitation, Monterey, California, Oct. 14-16, 1981, pp. 638-653

[70] D.O. Heinrich, "Electrostatic Precipitator Collector Spacings ", Atmospheric Enviroment, Vol. 13, 1979, pp. 1707-1711.

[71] H.J. White, op. cit. , pp. 198-209.

[72] S. Noso, "Performance Characteristics of Electrostatic Precipitators with Wide Spacing", Proceedings of the First International Conference on Electrostatic Precipitation, Monterey, California, Oct. 14-16, 1981, pp. 654-667.

[73] L. Lindau and S. Matts, "Some Space Charge Problems Encountered With Large Electrode Spacing", Proceedings of the Second International Conference on Electrostatic Precipitation, Kyoto, Japan, Nov. 12-15, 1984.

[74] S.A. Matts, "Some Experiences with Increased Electrode Spacing", CSIRO Conference on Electrostatic Precipitation, Leura, Aug. 23-24, 1978, paper No. 13.

[75] S. Masuda, "Present Status of Wide-Spacing Type Precipitator in Japan", EPA Symposium, Denver, 1979, pp. 483-501.

[76] C. Golkowski and M. Chojnowski, "The Role of Electrode Spacing in the Performance of the Electrostatic

Precipitator", Journal of Electrostatics, Vol. 14, 1983, pp. 339-348.

[77] A.A. Elmoursi and G.S.P. Castle, "Modeling of Corona Characteristics in a Wide-Duct Precipitator Using the Charge Simulation Technique", Industry Applications Society Conference Record, 1984, pp. 1192-1200.

[78] O.J. Tassicker, "Boundary Probe for Measurement of Current Density and Electric Field Strength - With Special Reference to Ionized Gases", Proc. IEE, Vol. 121, No. 3, March 1974, pp. 213-220.

[79] P.A. Lawless and L.E. Sparks, "Prediction of Voltage-Current Curves for Novel Electrodes, Part I. Wire Electrodes", presented at the fifth Symposium on the Transfer and Utilization of Particulate Control Technology, Kansas City, Missouri, Aug. 27-30, 1984.

[80] I.I. Inculet, Z. Kucervosky and M. Suzuki, "Electric Charging of Particles Near the Corona Glow Region in Air-CO Mixtures", IEEE Trans. on Industry Applications, Vol. IA-15, No. 3, May/June 1979, pp. 276-287.

END

13-1-85

FIN